Investigations of Methods for Quantifying Diffusive Transport Processes in Sedimentary Rock

NWMO TR-2013-18

December 2013

Diana Loomer, Yan Xiang and Tom Al

University of New Brunswick

NUCLEAR WASTE MANAGEMENT ORGANIZATION
SOCIÉTÉ DE GESTION DES DÉCHETS NUCLÉAIRES

Nuclear Waste Management Organization
22 St. Clair Avenue East, 6th Floor
Toronto, Ontario
M4T 2S3
Canada

Tel: 416-934-9814
Web: www.nwmo.ca

Investigations of Methods for Quantifying Diffusive Transport Processes in Sedimentary Rock

NWMO TR-2013-18

December 2013

Diana Loomer, Yan Xiang and Tom Al
University of New Brunswick

Document History

Title:	Investigations of Methods for Quantifying Diffusive Transport Processes in Sedimentary Rock		
Report Number:	NWMO TR-2013-18		
Revision:	R000	Date:	December 2013
University of New Brunswick			
Authored by:	Diana Loomer, Yan Xiang and Tom Al		
Verified by:	Not Applicable		
Approved by:	Tom Al		
Nuclear Waste Management Organization			
Reviewed by:	Tammy Yang, Monique Hobbs		
Accepted by:	Mark Jensen		

ABSTRACT

Title: **Investigations of Methods for Quantifying Diffusive Transport Processes in Sedimentary Rock**
Report No.: **NWMO TR-2013-18**
Author(s): Diana Loomer, Yan Xiang and Tom Al
Company: University of New Brunswick
Date: December 2013

Abstract

Diffusion measurement techniques for low-permeability sedimentary rocks have been advanced using new and/or modified methods in several areas: i) effective diffusion coefficient (D_e) measurements with confining pressure (CP); ii) improvements in the X-ray radiography (RAD) method; iii) method development for creating partial gas/brine saturation conditions in rock for diffusion studies; and iv) imaging diffusion pathways using scanning electron microscopy (SEM).

The through-diffusion method was modified to measure D_e values normal to bedding before and after confining pressure was applied to the rock sample. As pressure increased from ambient laboratory pressure (AP) to a CP of 12.0 MPa, a 14% decrease in the D_e of tritiated water (D_{eHTO}), and a 17% decrease in the D_e of iodide (D_{eI}) were observed in Queenston Formation shale drill core from the Michigan Basin. The decreases in D_e were much larger for Georgian Bay Formation shale samples (CP of 15.1 MPa): 32% in D_{eHTO} and 44% in D_{eI}. For Cobourg Formation limestone and argillaceous limestone samples (CP of 17.4 MPa), the decrease in D_e for both tracers ranged from 31% to 35%.

The RAD calibration method was revised to use natural sandstones as the calibration matrix for quantifying the correlation between the change in X-ray attenuation and the I^- tracer concentration in a sample. The natural sandstones were not suitable calibration matrices for the non-conservative tracer cesium (Cs^+). As an alternative, the relationships between the calibration functions for the glass vials, sandstones and ceramics observed in the I^- calibration were exploited and a new calibration function for Cs^+ was determined. The revised calibration approach will be used in any future X-ray radiography work.

The D_{eI} and I^--accessible porosity values measured in Opalinus Clay samples from the Mont Terri Underground Rock Laboratory, Switzerland using the RAD method under unconfined conditions were found to be higher than published values. This resulted from the swelling of the Opalinus Clay in the RAD cell. The RAD cell was then re-designed to hold swelling samples. The one D_{eI} value (4.7×10^{-12} m^2/s) measured using the RAD confining cell is consistent with published values. For cesium (Cs^+) diffusion measurements, the multicomponent reactive transport code MIN3P was used to calculate the Cs^+ concentration profiles. Estimates of the pore diffusion coefficients (D_{pCs}) and the selectivity coefficients ($\log K_{Cs+/Na+}$) were obtained using the model-independent parameter estimation code, PEST. The average D_{pCs} parallel to bedding was 1.7×10^{-9} m^2/s and the average D_{pCs} normal to bedding was 8.1×10^{-10} m^2/s. The range of measured $\log K_{Cs+/Na+}$ values (1.4 to 2.1) is consistent with published values. The log $K_{Cs+/Na+}$ decreases as the Cs^+ tracer concentration increases.

A new method to create and to control gas/brine partial saturation conditions in rock samples is under development. Preliminary studies by the X-ray RAD method show promise. Further development on a new Am-241 gamma ray radiography technique is underway.

Diffusive pathways in the Michigan Basin rock samples were visualized using SEM. The I^- tracer was fixed in rock pores by precipitating insoluble silver iodide, AgI. At the micrometer (μm) scale, characteristic pathways were differentiated.

TABLE OF CONTENTS

LIST OF TABLES

Page

LIST OF FIGURES

Page

LIST OF ABBREVIATIONS

AFM	Atomic force microscope
AP	Ambient laboratory pressure
BSE	Back scattered electron imaging mode
CEC	Cation exchange capacity
CL	Cathodoluminescence
CP	Confining pressure
CPTD	Confining-pressure through-diffusion
D_p	Pore diffusion coefficient: $D_p=(\delta/\tau)\cdot D_0$, where δ is constrictivity, τ is tortuosity, and D_0 is the free water diffusion coefficient
D_e	Effective diffusion coefficient: $D_e=\phi\ D_p$.
D_a	Apparent diffusion coefficient (term included for completeness, but not used in this report): $D_a=D_e/\alpha$, where the rock capacity factor is $\alpha=\phi+\rho K_d$, ρ is the bulk dry density of the rock, and K_d is the distribution coefficient for the solute
$D_{e\text{-}AP}$	D_e measured at ambient laboratory pressure
$D_{e\text{-}CP}$	D_e measured at confining pressure
$D'_{e\text{-}CP}$	D_e measured with repeated application of confining pressure
D_{eHTO}	D_e measured with tritiated water, HTO, tracer
D_{eI}	D_e measured with iodide, I^-, tracer
D_{pCs}	D_p measured with cesium, Cs^+, tracer
DGR	Deep geological repository
EDS	Energy-dispersive X-ray spectroscopy
FIB	Focused ion beam milling for TEM sample preparation
$\log K_{Cs+/Na+}$	Selectivity coefficient
LSCM	Laser scanning confocal microscopy
L-SPW	DGR limestone synthetic porewater
mbtf	Meters below the tunnel floor
MIN3P	Multicomponent reactive transport code
NB	Normal-to-bedding orientation
NWMO	Nuclear Waste Management Organization
OPA	Opalinus Clay
PB	Parallel-to-bedding orientation
PEST	Model-independent parameter estimation code
RAD	X-ray radiography
SEM	Scanning electron microscopy
S-SPW	DGR shale synthetic porewater
S/N	Signal-to-noise ratio
TD	Through-diffusion
TEM	Transmission electron microscopy
UNB	University of New Brunswick
URL	Underground research laboratory
XRD	X-ray diffraction
ϕ_I	Iodide-accessible porosity
ϕ_w	Water-loss porosity
ΔP	Change in confining pressure
$\Delta\mu$	Change of X-ray attenuation coefficient
$\Delta\mu_{sat}$	X-ray attenuation coefficient saturated with tracer

1. INTRODUCTION

This technical report was prepared for the Nuclear Waste Management Organization (NWMO) and documents the activities and outcomes of five (5) research studies undertaken at the University of New Brunswick (UNB) from March, 2009, to March, 2012. The research is intended to develop new, and improve existing, methodologies for laboratory measurements and to gain a better understanding of mechanisms controlling solute transport in diffusion-dominated sedimentary rock systems. Such rocks are under consideration in Canada as potential host and barrier rocks for a deep geological repository (DGR) for the long-term management of radioactive waste.

1.1 OBJECTIVES

The projects focused on the continued development of analytical tools and methods for quantification of diffusion and reaction processes in low-permeability sedimentary rocks. Following the results of previous studies (Cavé et al. 2009a, b; Cavé et al. 2010; Al et al. 2009, 2012), several research questions were formulated, which the current projects attempt to address:

- What is the effect of confining pressure on diffusion rates in sedimentary rock samples from the Michigan Basin?
- With the continued use of the X-ray radiography (RAD) method, discrepancies between expected and measured iodide-accessible porosities (ϕ_I) have arisen. What is causing these discrepancies and can the radiography method be improved to resolve this issue?
- How do the results of the radiography method compare to other analytical methods for determining diffusion properties in the well-characterized Opalinus Clay (OPA) from Switzerland?
- Can the radiography method be used to measure solute diffusion coefficients in partially saturated rocks where the pore volume is occupied by porewater and gas phases?
- What are the capabilities and limitations to the use of scanning electron microscopy (SEM) for visualizing diffusion pathways in low-permeability rocks?

To address these issues, the following five research projects were undertaken:

1) Modification of the through-diffusion (TD) cell design to measure effective diffusion coefficients (D_e) with confining pressure (CP);
2) Modification of the calibration method for X-ray radiography using different calibration matrices;
3) Measurement of pore diffusion coefficients (D_p) for conservative (iodide, I^-) and non-conservative (cesium, Cs^+) tracers in the Opalinus Clay. The Opalinus Clay has been extensively studied and is therefore an excellent material for comparing the radiography method to other analytical methods used for measuring diffusive transport through low-permeability sedimentary rocks;
4) Development of a method to create partially saturated conditions in low-permeability rocks, and conduct an evaluation of the potential for monitoring the degree of partial saturation using radiography. The ultimate goal of this project is to measure the effect of the presence of a gas phase on diffusion coefficients; and

5) Visualization of the I^- tracer distribution in samples using SEM (μm scale) with the goal of defining diffusive pathways in rocks.

1.2 REPORT STRUCTURE

The main body of this report is organized according to three major themes:

I. Modification of the through-diffusion cell and presentation of the results of the diffusion measurements with confining pressure (Section 2);
II. Applications and modifications of the radiography method (Sections 3-5). Topics covered include: i) modification of the calibration method (Section 3); ii) measurement of diffusion and diffusion-reaction parameters in the Opalinus Clay and modification of the method to accommodate swelling and/or disaggregated materials (Section 4); and iii) design and preliminary testing of a method for creating and monitoring partially saturated conditions in shale (Section 5); and
III. SEM imaging of porosity and solute transport in shale and argillaceous limestone samples from the Michigan Basin at the μm scale (Section 6). The new method developed includes fixation of I^- tracer with precipitation of AgI and the methods attempted include the use of silver-doped low-viscosity epoxy impregnation and the use of cathodoluminescence (CL) imaging.

The scientific conclusions from these research projects are summarized at the end of each section and concluding remarks are presented in Section 7.

2. DIFFUSION MEASUREMENTS WITH CONFINING PRESSURE

All previous diffusion measurements on the Michigan Basin rock samples were conducted at ambient laboratory pressure and as a result, the reported diffusion coefficients are systematically overestimated because in situ lithostatic stress was not taken into account. Diffusion coefficients for conservative tracers, including tritiated water (HTO) and halides, were determined for the Opalinus Clay at Mont Terri at both field scale (m scale) under in situ conditions (Gimmi et al. 2014; Van Loon et al. 2004; Wersin et al. 2004) and at laboratory scales (from cm to tens of cm) under applied confining pressures (García-Gutiérrez et al. 2006; Van Loon et al. 2003a). Comparison between these measured D_e values indicates an excellent agreement (Tevissen et al. 2004). This finding suggests that applying confining pressures that are equivalent to the compressive pressures beneath the geological sites to diffusion samples in the laboratory is an effective alternative.

The objectives of this study were to 1) advance our existing through-diffusion method to measure D_e values before and after applying confining pressure to the sample; 2) provide estimation of correction factors for D_e values measured at AP ($D_{e\text{-}AP}$); and 3) understand the factors determining the degree of the confining pressure effect. The approach was to conduct a systematic study on a variety sedimentary rock types of variable porosity.

Four different diffusion samples from three DGR core segments were selected for this study: Queenston Formation shale, Georgian Bay Formation shale, Cobourg Formation limestone and Cobourg Formation argillaceous limestone. These rock units are located between 472 and 681 m below ground surface, with estimated in situ vertical pressures of 12.0 to 17.4 MPa using average rock density of 2.6 g/cm^3 (Gorski et al. 2009). The D_e values were determined by TD experiments using HTO and I^- tracers with confining pressures ranging from ambient laboratory pressure to 17.4 MPa.

2.1 METHODS

We set out to develop a TD method that would use samples of 76 mm diameter, equivalent to the diameter of the core retrieved during site characterization activities. This would minimize sample preparation time so that samples could be quickly prepared in the field by cutting 10 mm slices and mounting them in the diffusion cell. Several attempts were made to use 76 mm diameter rock samples with thicknesses between 10 and 20 mm for TD measurements under confining pressure. Despite multiple attempts to improve the cell design, the samples fractured when the pressure was applied during each attempt. Recognizing that the large diameter resulted in relatively large differential forces across the sample surface, the sample size was reduced to a diameter of 25.4 mm and a thickness of approximately 10 mm (Figure 1). By using smaller diameter samples, the total external force was reduced from 70-90 kN for 76 mm diameter samples to 10-20 kN for 25.4 mm diameter samples and the differential forces across the samples were also minimized.

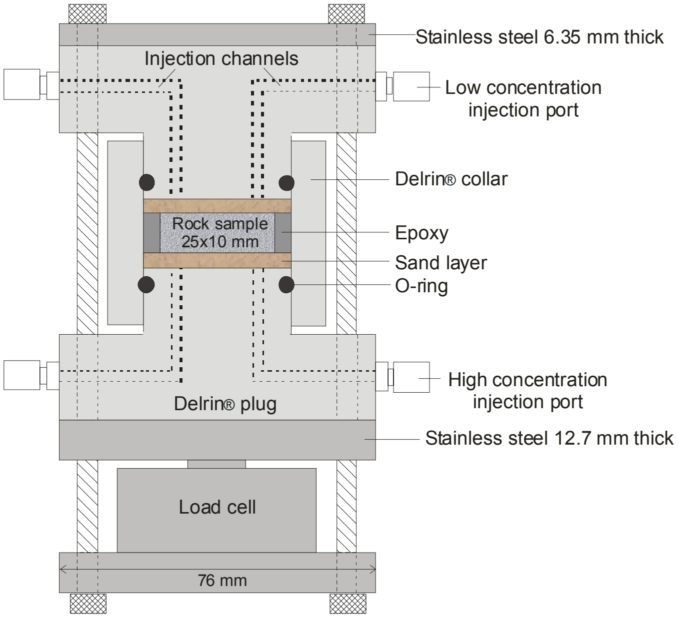

Figure 1: Diagram of the 25.4 mm Confining-Pressure Through-Diffusion Cell

Sample DGR3-472 (Queenston shale, normal to bedding) was mounted in a 25.4 mm confining-pressure through-diffusion (CPTD) cell (Figure 1) with an applied force equivalent to the in-situ CP of 12.0 MPa (Table 1) followed by saturation with DGR shale synthetic porewater (S-SPW) (Al et al. 2009). During the saturation period, the pressure gradually decreased due to consolidation of the rock. The applied force was adjusted daily over a period of five to six weeks until it stabilized at a constant pressure of 12.0 MPa. The TD experiment with HTO tracer (Table 1) was operated until the diffusion flux reached a steady state, and then the pressure was decreased to ambient pressure while continuing to monitor the diffusion flux. After a new steady state was established at AP, a pressure of 12.0 MPa was re-applied to test for reproducibility in the D_e measurement. The diffusion experiment with HTO tracer lasted 168 days and then a new TD experiment was initiated with the I^- tracer and a similar experimental sequence.

Table 1: Experimental Conditions Used in the CPTD Experiments

Sample	Description	CP (MPa)	Matrix	HTO tracer Concentration (Bq/mL)	HTO tracer Volume (mL)	I^- tracer Concentration (M)	I^- tracer Volume (mL)
DGR3-472	Queenston shale	12.0	S-SPW	5908	200	1.0	100
DGR2-593-1	Georgian Bay shale	15.1	S-SPW	4659	195		
DGR2-593-2	Georgian Bay shale	15.1	S-SPW	4407	200	1.0	150
DGR3-681-1	Cobourg limestone	17.4	L-SPW	49533	40	1.0	100
DGR3-681-2	Cobourg arg. Limestone	17.4	L-SPW	49322	40	1.0	100

All samples were prepared normal to bedding. S-SPW means DGR shale synthetic porewater and L-SPW means DGR limestone synthetic porewater (Al et al. 2009).

The same experimental procedures were followed for a Georgian Bay Formation shale sample (DGR2-597) except that a higher confining pressure of 15.1 MPa was applied, corresponding to the greater depth of the formation. This sample fractured during the experiment under the CP and the data are not reported. A second attempt, with sample DGR2-593-1 (normal to bedding), was successfully increased to and held at the CP, but fractured after the pressure was decreased and held at AP. The experimental procedure was modified on the third attempt (DGR2-593-2, normal to bedding) by imposing pressure changes incrementally, from 15.1 to 5.0 MPa in a first step, and then to near ambient pressure (0.6 MPa) in a second step. This approach was successful. Although no D_{eI} values are available from DGR2-593-1, the D_{eHTO} data collected from duplicates DGR2-593-1 and DGR2-593-2 were used for evaluating the reproducibility. Two sub-samples from the Cobourg Formation argillaceous limestone (DGR3-681) were prepared: one from limestone material (DGR3-681-1, normal to bedding), and another from an argillaceous zone (DGR3-681-2, normal to bedding). The successful experimental procedures described above were followed except that DGR limestone synthetic porewater (L-SPW) was used for saturation and a higher confining pressure of 17.4 MPa was applied (Table 1) corresponding to the in situ CP for this formation.

No replicates were prepared because each sample test required a load cell unit to monitor the pressure change throughout the duration of the experiment which lasted more than one year. Four load cell units were available, one for each of the four lithologies studied. The only duplicate samples studied were DGR2-593-1 and DGR2-593-2 (Georgian Bay Formation). Reproducibility of the D_e values measured under confining pressures was tested for each sample by re-applying CP on the same diffusion sample.

All D_e values were calculated using the average diffusive mass flux (J) at steady state:

$$J = -D_e\ (dc/dx) \qquad [\ 1\ ]$$

where dc/dx is the concentration gradient of the tracer across the sample.

2.2 RESULTS AND DISCUSSION

In accordance with the objective of understanding the effect of confining pressure on D_e, the following data are presented in terms of the change in D_e that results from an increase in pressure.

For Queenston shale sample DGR3-472, a D_e value of 4.9×10^{-12} m^2/s was measured with HTO tracer at ambient pressure ($D_{eHTO\text{-}AP}$) (Figure 2a) compared to 4.2×10^{-12} m^2/s at 12.0 MPa ($D_{eHTO\text{-}CP}$), indicating that a change in pressure from ambient to 12.0 MPa results in a 14% decrease in D_{eHTO}. When 12.0 MPa was re-applied, the $D'_{eHTO\text{-}CP}$ (D_e measured with repeated application of CP) returned to the previously measured value (within experimental error; Figure 2a), indicating that the confining pressure effect is reproducible. In comparison, a D_{eI} value of 2.9×10^{-12} m^2/s was measured at ambient pressure (Figure 2b) and a lower D_{eI} of 2.4×10^{-12} m^2/s (17% decrease) was obtained under confining pressure of 12.0 MPa. Similar to measurements with the HTO tracer, when the CP of 12.0 MPa was re-applied, $D'_{eI\text{-}CP}$ returned to the previously measured $D_{eI\text{-}CP}$ value (within experimental error; Figure 2b), indicating that the confining pressure effect is reproducible.

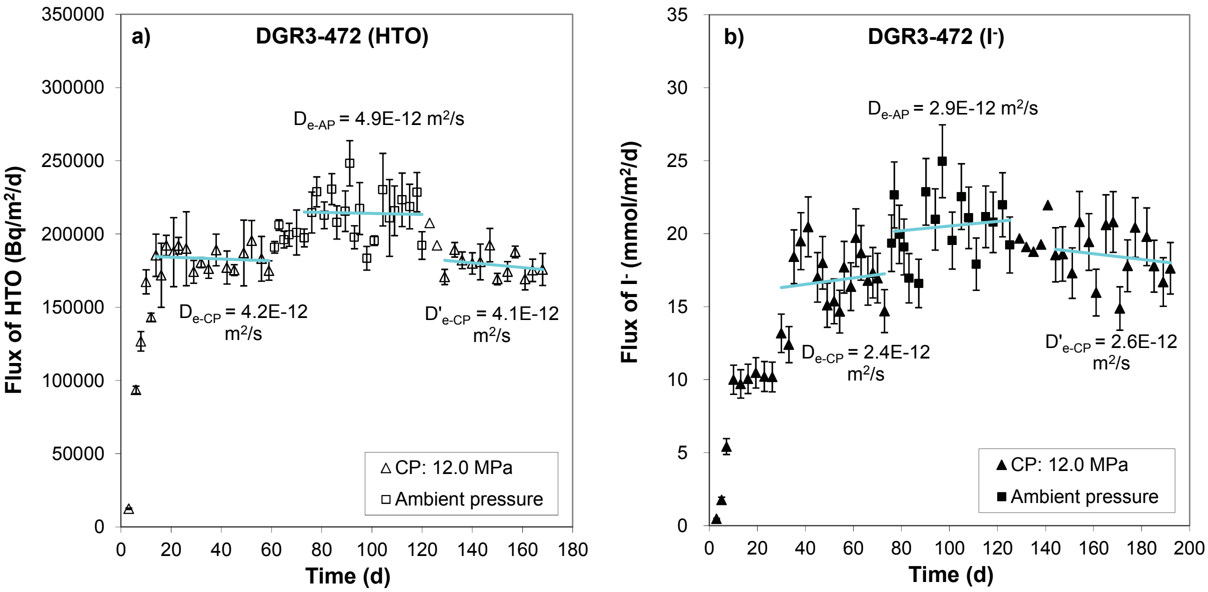

Figure 2: Tracer Flux for Queenston Shale Sample DGR3-472: (a) HTO and (b) I^-

Higher confining pressure (15.1 MPa) was applied to the Georgian Bay Formation shale sample DGR2-593 corresponding to the increased depth of this formation. These rock samples contain higher clay-mineral content (60-70%, Koroleva et al. 2009) and are softer and more fragile than the Queenston Formation shale sample (50-60% clay). The measured D_{eHTO} values were 4.1×10^{-12} m^2/s at a near ambient pressure (0.6 MPa), 3.1×10^{-12} m^2/s at confining pressure of 5.0 MPa (24% decrease), and 2.8×10^{-12} m^2/s at confining pressure of 15.1 MPa (an additional decrease of ~10%; Figure 3a). Re-application of a 15.1 MPa confining pressure caused $D'_{eHTO\text{-}CP}$ to decrease to 3.1×10^{-12} m^2/s, close to the previously measured value of 2.8×10^{12} m^2/s.

The data show some indication of a continued slow decrease over time (Figure 3a) suggesting that the confining pressure effect may be reproducible. The reproducible trend was observed with I^- tracer when a 15.1 MPa CP was re-applied (Figure 3b). The D_{eI} value decreased from 2.5×10^{-12} to 1.6×10^{-12} m^2/s (36% decrease) after a pressure increase from 0.6 to 5.0 MPa (Figure 3b). The D_{eI} value decreased further to 1.4×10^{-12} m^2/s (additional 13% decrease) following an increase in CP from 5.0 to 15.1 MPa.

The 10% decrease of D_{eHTO} and 13% decrease of D_{eI} corresponding to a pressure change from 5.0 to 15.1 MPa are lower than the 16% and 32% decreases, respectively, reported by van Loon et al. (2003b) for the Opalinus Clay from Benken, Switzerland, in response to a similar pressure change (4 to 15 MPa). The differences may be accounted for by the higher uniaxial compressive strength (UCS) and more specifically, by the elastic modulus parameter (a measure of rock deformation property with higher values being stiffer) of the Georgian Bay shale (9 GPa, NWMO 2011) when compared to Opalinus Clay (4 GPa, Corkum and Martin 2007a, b), indicating that Georgian Bay shale is stronger and stiffer than OPA. The results of D_e measurements conducted at multiple confining pressure conditions (Figures 3 and 4) show a consistent trend of decreasing D_e value as a result of increasing confining pressure, but the relationship is non-linear. This finding is consistent with the non-linear mechanical behaviour, including elastic modulus, of rock materials in general (Corkum and Martin 2007a, b).

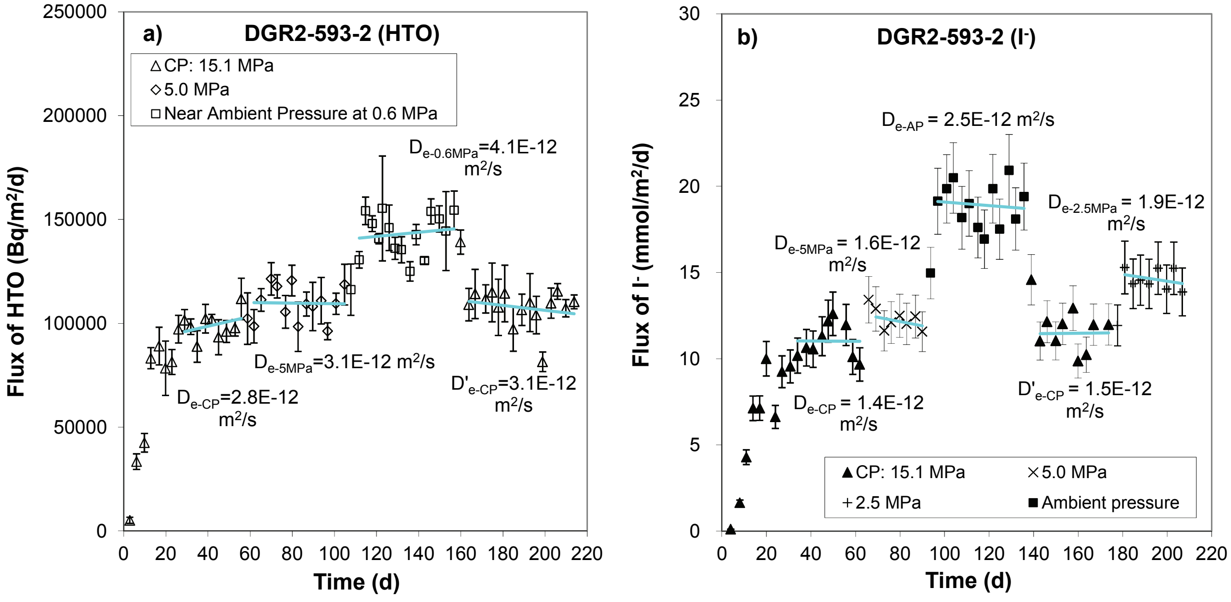

Figure 3: Tracer Flux for Georgian Bay Shale Sample DGR2-593-2, (a) HTO and (b) I^-. The Confining Pressure of 15.1 MPa was Decreased to 5.0 MPa, and then to 0.6 MPa

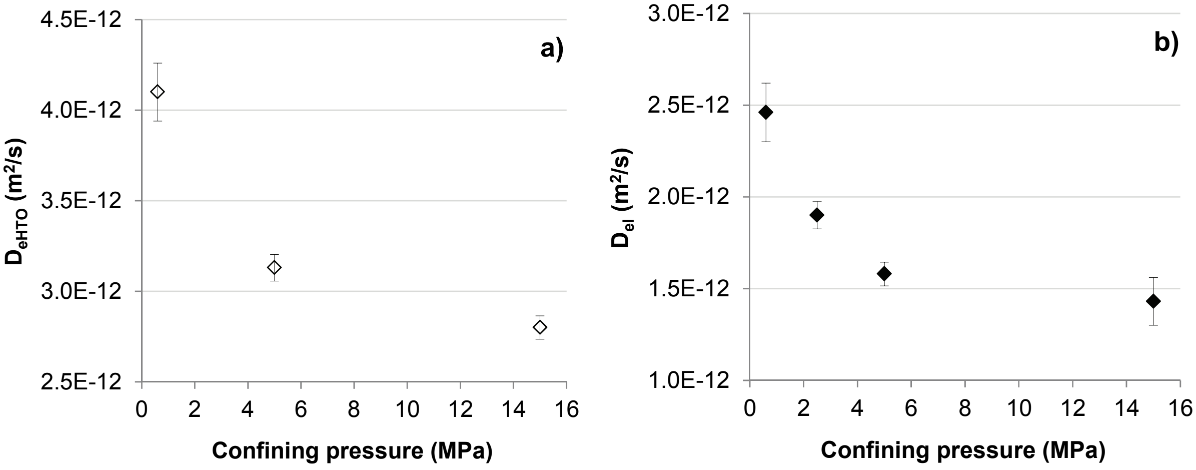

Figure 4: Plots of D_e Values as a Function of Pressure for Georgian Bay Formation Shale DGR2-593-2; (a) HTO and (b) I^-

In general, the trends in D_{eHTO} and D_{eI} values versus confining pressure for the Cobourg Formation limestone samples are similar to those for the shale samples in that D_e values decrease with increasing confining pressure (Figure 5).

There are additional noteworthy characteristics that relate specifically to the carbonate rock samples. First, regardless of the tracer and confining pressure, the argillaceous limestone rock sample has consistently higher D_e values (factor of approximately 2) than the limestone rock sample, suggesting that diffusive transport may occur preferentially in the argillaceous zones. Second, when confining pressure is re-applied to these carbonate samples following a measurement period at ambient pressure, D_{eHTO} values decrease slightly but do not return to the values previously measured at 17.4 MPa (Figures 5a and 5c).

The D_e data obtained from CPTD experiments (Figures 2, 3 and 5) are summarized in Table 2 and Figure 6. Results indicate that the D_e values determined under confining pressure are consistently lower than those determined at ambient pressure. Comparison between the two tracers, HTO and I^-, indicates little difference of the effect of confining pressure on effective diffusion coefficient for the Cobourg Formation limestone samples. The imposed changes in confining pressure resulted in 34% and 31% decrease in D_{eHTO}, and 35% and 33% in D_{eI}, for limestone and argillaceous limestone, respectively. For the Queenston Formation sample, the change in confining pressure resulted in a 14% decrease in D_{eHTO} and 17% in D_{eI}. However, tracer-specific differences in D_e values were apparent for the Georgian Bay Formation shale. In this case, an increase in confining pressure results in a 32% decrease in $D_{eHTO,}$ and a 44% decrease in D_{eI} (Table 2). The difference between the two shales may be due in part to differences in strength, which is measured by UCS, and in stiffness, which is measured by elastic modulus parameter (Table 2). Under confining pressure, the weaker and less stiff Georgian Bay Formation shale will undergo greater pore-size reduction which would enhance anion exclusion effects.

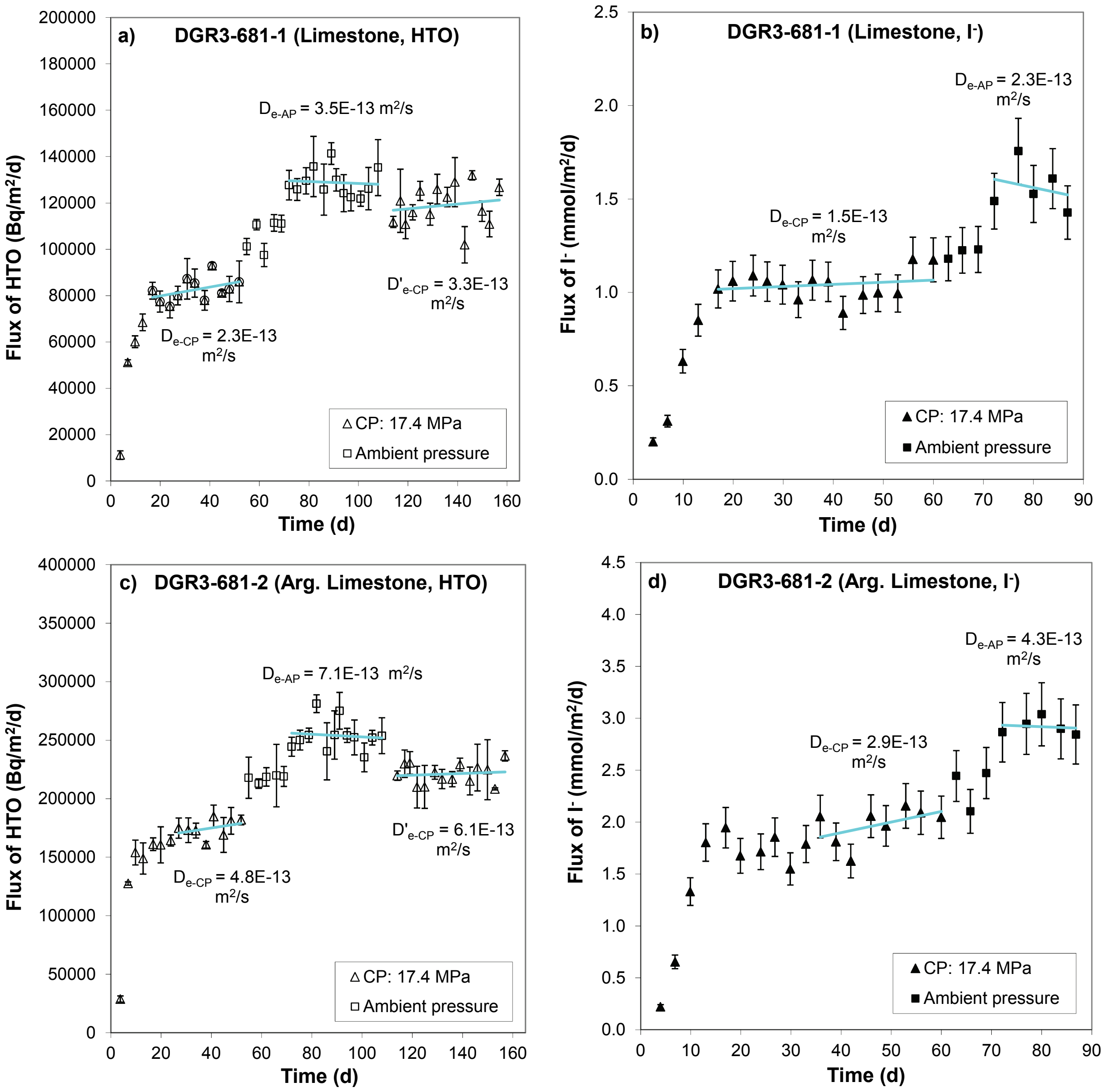

Figure 5: Tracer Flux for Cobourg Formation Limestone Sample DGR3-681-1, (a) HTO and (b) I$^-$, and for Cobourg Formation Argillaceous Limestone Sample DGR3-681-2, (c) HTO and (d) I$^-$

Table 2: Confining Pressure-TD Sample Description and Data Summary

Sample[a]	**DGR3-472**	**DGR2-593-1**	**DGR2-593-2**	**DGR3-681-1**	**DGR3-681-2**
Formation	Queenston	Georgian Bay	Georgian Bay	Cobourg	Cobourg
Lithologic type	Red shale	Grey shale	Grey shale	Limestone	Arg. limestone
Clay content[b]	50-60%	60-70%	60-70%	low	10-15%
CP (MPa)	12.0	15.1	15.1	17.4	17.4
UCS-DGR (MPa)[c]	25-50	25-50	25-50	50-100	50-100
UCS-regional (MPa)[d]	44	35	35	72	72
Elastic modulus (GPa)[d]	15	9	9	32	32
			HTO		
$D_{eHTO\text{-}CP}$ (m^2/s)[e]	4.2E-12	3.3E-12	2.8E-12	2.3E-13	4.8E-13
$D_{eHTO\text{-}5MPa}$ (m^2/s)[e]			3.1E-12		
$D_{eHTO\text{-}AP}$ (m^2/s)[f]	4.9E-12	4.8E-12	4.1E-12	3.5E-13	7.0E-13
% Decrease[g]	14	31	32	34	31
$D'_{eHTO\text{-}CP}$ (m^2/s)[h]	4.1E-12		3.1E-12	3.3E-13	6.1E-13
			I^-		
$D_{eI\text{-}CP}$ (m^2/s)[e]	2.4E-12		1.4E-12	1.5E-13	2.9E-13
$D_{eI\text{-}5MPa}$ (m^2/s)[e]			1.6E-12		
$D_{eI\text{-}AP}$ (m^2/s)[f]	2.9E-12		2.5E-12	2.3E-13	4.3E-13
% Decrease[g]	17		44	35	33
$D'_{eHTO\text{-}CP}$ (m^2/s)[h]	2.6E-12		1.5E-12		

[a]Samples were prepared normal to bedding. [b]Koroleva et al. (2009). [c]Uniaxial compressive strength data reported for DGR samples in Gorski et al. (2009, 2011). [d]Uniaxial compressive strength and elastic modulus data compiled from Southern Ontario database (NWMO, 2011) for the Michigan Basin formations. The D_e data were collected [e]under the confining pressure as indicated in Table 1; [f]at ambient laboratory pressure; [g]with changing pressure from ambient pressure to confining pressure; and, [h]under the re-applied confining pressure.

Results of D_{eHTO} obtained from the duplicates DGR2-593-1 and DGR2-593-2 (Georgian Bay Formation) indicate reproducibility in the effect of confining pressure on D_e (31% and 32% decrease, respectively; Table 2). Although diffusion samples DGR3-681-1 and DGR3-681-2 were cut from the same core segment, one is from limestone and the other from argillaceous limestone. The results from these two samples (31% to 35% decreases in D_e, Table 2) show little difference in the magnitude of the confining pressure effect on D_e for this level of lithological heterogeneity in the limestone at this pressure range.

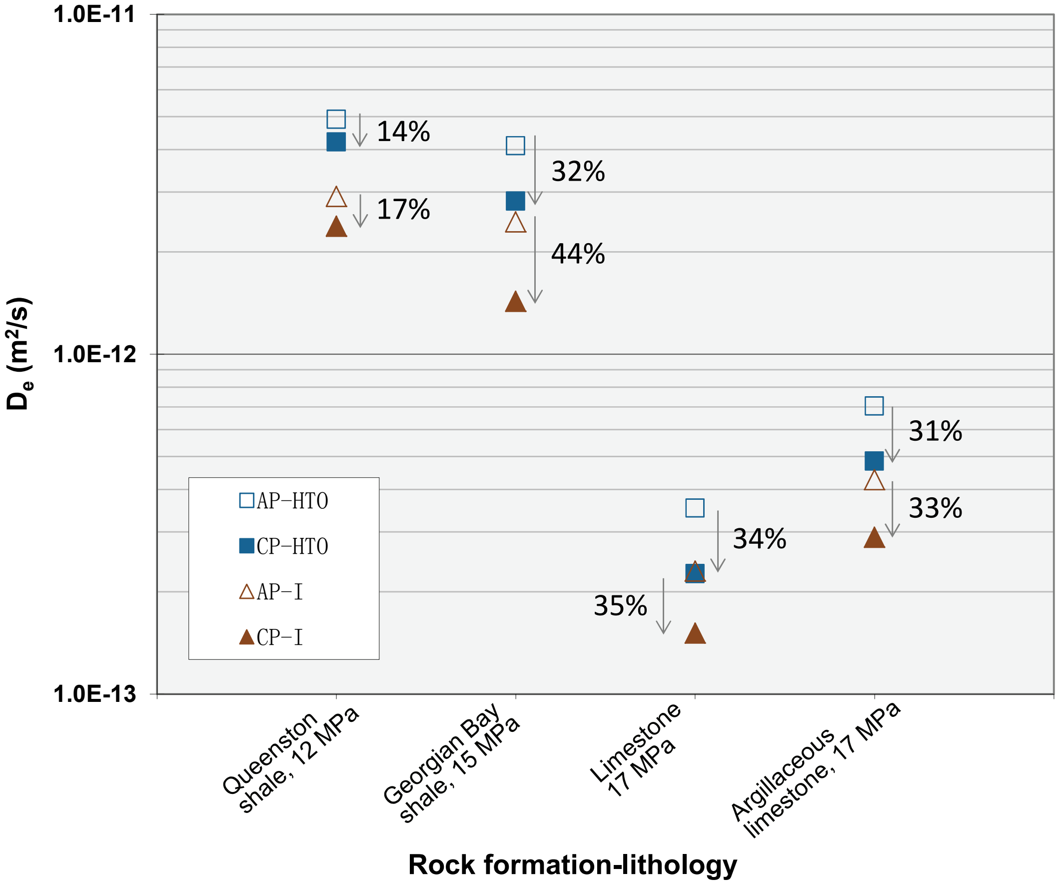

Figure 6: Summary of Measurements of D_e Normal to Bedding

2.3 SUMMARY

The through-diffusion technique has been advanced to measure D_e values on rock samples under confining pressures that represent the in situ lithostatic stress conditions. The method has been tested successfully using four samples that represent three key lithologies from the proposed host and cap-rock formations. The key findings of the confining-pressure diffusion measurements are:

1. A 14% decrease in D_{eHTO} and a 17% decrease in D_{eI} were observed for Queenston Formation shale sample (ΔP = +12.0 MPa), suggesting that the effect of the applied pressure is small and that the difference between HTO and I^- tracers is also small for this Formation.

2. The pressure effect on effective diffusion coefficient for Georgian Bay Formation shale sample is larger; with ΔP = +15.1 MPa, decreases of 31-32% (D_{eHTO}) and 44% (D_{eI}) were observed. This tracer-specific effect is attributed to the enhancement of anion exclusion at high pressure due to pore-size reduction.

3. Effects of confining pressures on D_e are reproducible for Queenston Formation and Georgian Bay Formation shale samples, but less so for the argillaceous limestone.

4. Little difference was detected for the confining pressure effect on D_e between limestone and argillaceous limestone materials. The decreases in D_{eHTO} and D_{eI} values ranged from 31 to 35% ($\Delta P = +17.4$ MPa).

5. The D_e value shows a consistent trend of decrease as a result of confining pressure increase, but such an effect of confining pressure on D_e is non-linear, with larger effects apparent at the lower pressure range. The magnitude of the effect of confining pressure on D_e is reproducible on replicates.

Based on our findings, the following suggestions are made for future work in diffusion measurements and for interpretation of D_e values measured at ambient laboratory pressure.

1. A CPTD cell and accompanying methodology should be developed that allows rock samples to be quickly mounted in diffusion cells in the field immediately after drilling. This should allow samples to be shipped to the lab under confining pressure for subsequent measurement, thereby minimizing artifacts related to sample relaxation.

2. It is not practical to conduct all diffusion measurements at in situ confining pressures. However, by conducting CPTD measurements on key lithologies, it may be possible to develop correction factors for D_e data determined at ambient laboratory pressure. For example, the limited data from this study have been used to estimate correction factors (Table 3) that could be refined with additional CPTD measurements. This approach can be used for $D_{e\text{-}AP}$ values measured by other techniques.

Table 3: Suggested Pressure Correction Factors for Effective Diffusion Coefficients Measured at Ambient Laboratory Pressure ($D_{e\text{-}AP}$)

Rock type	HTO tracer Correction factor	I^- tracer Correction factor
Queenston Formation shale	0.85	0.85
Georgian Bay Formation shale	0.70	0.60
Limestone (all formations)	0.70	0.70

3. REVISIONS TO THE RADIOGRAPHY CALIBRATION METHOD

Over the past few years, our research group at UNB has continued to work with and develop the X-ray radiography (RAD) method for diffusion measurements (Cavé et al. 2009a, b 2010). This research has included three-dimensional (3D) computed tomography for imaging rock materials. In the course of this work, discrepancies have been observed between the iodide-accessible porosity, determined by radiography, and water-loss porosity (ϕ_w) measured gravimetrically. The ϕ_I values were always lower than ϕ_w, and because most of the work has involved low-permeability rocks with high clay contents, the difference was interpreted to result from anion exclusion. However, similar discrepancies were noted more recently for porous sandstones and vuggy limestones, which are not expected to exhibit anion-exclusion effects. After some investigation of the possible causes for the discrepancies, it was discovered that a systematic error arose from a beam hardening artefact that affects the calibration of the change in the X-ray attenuation coefficient ($\Delta\mu$) as a function of I^- tracer concentration. The calibration function is used to determine tracer concentrations in experimental samples, and consequently, ϕ_I. The calibration procedure was described by Cavé et al. (2009a).

Beam hardening is an unavoidable phenomenon in X-ray radiography but the problem arose because the beam hardening characteristics of the rock samples and the glass vials used for calibration are quite different. With this discovery, it became necessary to develop a new calibration method that would better match the beam hardening in the calibration material with the beam hardening in the rock samples. Two types of calibration materials were investigated for use as calibration standards: natural sandstones and manufactured ceramics. The results of the investigations lead to the revision of the calibration procedures used in the UNB RAD method for the two tracers, I^- and Cs^+. The revised procedures are described in the following sections.

3.1 NATURAL SANDSTONES

Well characterized, natural sandstone samples were selected as calibration matrices because they have known porosity, anion exclusion is not a factor ($\phi_w = \phi_I$), and their mineralogy and porosity distributions lead to beam hardening characteristics that are similar to the experimental samples. Three sandstones were selected based on their reported porosities, homogeneity and low clay and feldspar content. They were purchased from Kocurek Industries, Inc. (Caldwell, TX): the Berea Upper Gray (19-20% porosity from Kipton, Ohio), the Carbon Tan (12.2-17.7% porosity from Utah) and the Crab Orchard (6.6-8.7% porosity from Tennessee). The ϕ_w and mineralogy of the sandstones were also characterized at UNB and are described in the following sections.

3.1.1 Water-Loss Porosity

Experimental procedures for the water-loss porosity measurements are the same as those reported by Cavé et al. (2010), with the exception that the samples were first saturated under vacuum with tap water and dried in only one temperature step, at 105°C. These methods are based on the water imbibition technique presented by Emerson (1990). The composition of the natural porewater for these sandstones was unknown and therefore, tap water was used for the porosity measurements. Water-loss porosity measurements were conducted in triplicate on off cuts remaining after preparation of the RAD samples (Figure 7). It is apparent from Figure 7 that the Berea Upper Gray and Carbon Tan sandstones appear massive and homogenous, but heterogeneities are evident in the Crab Orchard specimen.

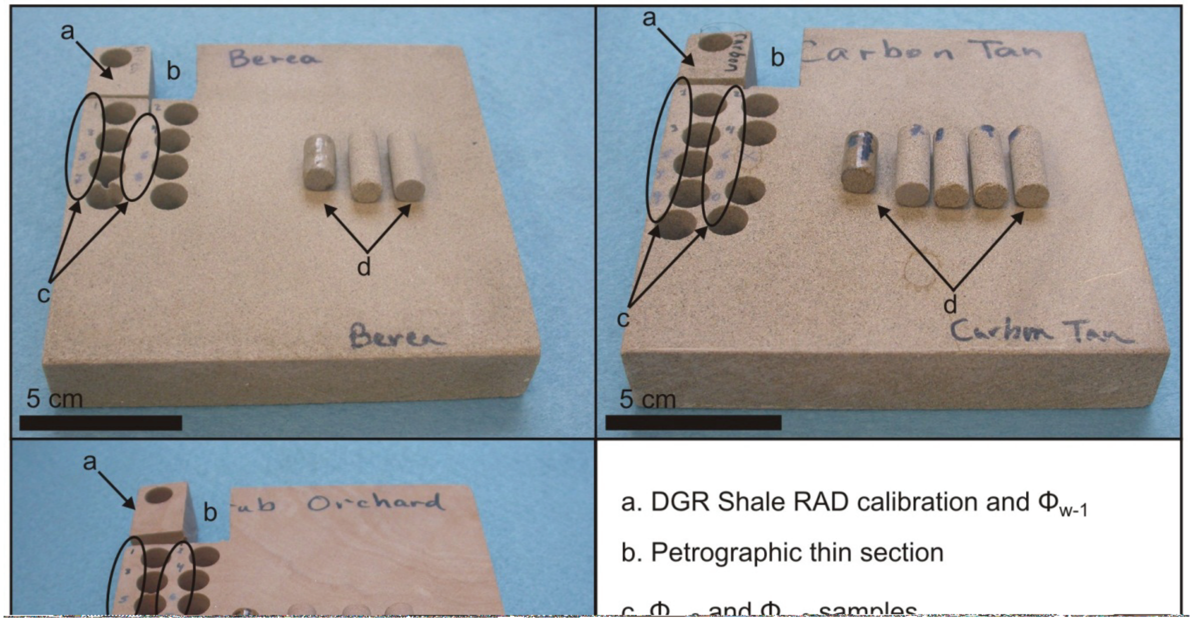

Figure 7: Images of the Sandstone Samples Used for the Iodide Calibration for Radiography. The Annotations Mark the Location of RAD Subcores for Calibrations, Water-Loss Porosity Samples and Petrographic Thin Section Locations

The porosity values measured at UNB and the porosity ranges reported by Kocurek Industries are presented in Table 4. The measured porosity values for the Berea Upper Gray and the Carbon Tan sandstones fall within the range reported by Kocurek Industries. However, the measured porosities for the Crab Orchard sandstone are slightly lower than the reported range. Information concerning the method of porosity measurement and other experimental details are not available from Kocurek Industries and, given the apparent heterogeneity of the Crab Orchard sandstone (Figure 7), a slightly different value for porosity is not considered unreasonable. The mean porosity of the 3 measurements made at UNB was used in the RAD calibration.

3.1.2 Mineralogy

The mineralogy of the sandstones was determined at UNB using X-ray Diffraction (XRD) and SEM. Off cuts from the RAD sandstone subcores were pulverized and powder diffraction analysis was performed using a Bruker D8 Advance Powder X-Ray Diffractometer equipped with a solid state detector. The X-ray diffractograms were analyzed using the International Centre for Diffraction Database PDF-4 and the Search-Match analytical software program Jade. Semi-quantitative analysis was performed using the Reference-Intensity-Ratio method.

Table 4: Sandstone Bulk Porosities

	Berea Upper Gray	**Carbon Tan**	**Crab Orchard**
	Range reported by Kocurek Industries		
	0.19 - 0.20	0.122 - 0.177	0.066 - 0.087
	Measured at UNB		
ϕ_{w-1}	0.198	0.129	0.054
ϕ_{w-2}	0.197	0.126	0.052
ϕ_{w-3}	0.194	0.130	0.056
Mean ϕ_w	**0.196**	**0.128**	**0.054**
σ	0.002	0.002	0.002
RSD (%)	1.14	1.90	3.90

"σ" means standard deviation and "RSD" means relative standard deviation.

Polished petrographic thin sections were prepared from the areas indicated in Figure 7 (areas labelled "b") and optical images were collected using the Leitz Laborlux 11 POL petrographic microscope. SEM was performed using a JEOL JSM6400 SEM equipped with an EDAX Genesis Energy Dispersive X-ray Spectroscopy (EDS) system operated with a 15 keV accelerating voltage and a 1.5 nA beam current. Back scattered electron (BSE) images, point EDS spectra and two-dimensional elemental maps were collected.

The results of the mineralogical analyses performed on the UNB samples are summarized in Table 5 along with published or other reference data for the sandstone formations, where available. The Berea Upper Gray and Crab Orchard sandstones are predominantly made up of quartz (80-90 wt%), while the Carbon Tan consists of 64 wt% quartz, 21 wt% carbonates and 15 wt% K-feldspar. Clay minerals are present in all the sandstones and, combined, represent up to approximately 10 wt% of the Berea Upper Gray and Crab Orchard sandstones (Table 5). In certain samples, some clay minerals such as micas+illite and kaolinite/pyrophyllite were below the XRD detection limits (1-2 wt%) but were observed by optical microscopy (Figure 8) and SEM (Figure 9). The objective of the XRD analysis was basic mineralogical characterization; special techniques were not used for discriminating clay minerals, such as ethylene glycol solvation (Mosser-Ruck et al. 2005). The SEM-EDS analyses indicate the clay minerals possess a range of compositions, likely reflecting varying degrees of alteration and also the effects of overlapping minerals in the analyses. The maximum resolution for imaging and chemical analyses for this system (i.e., the beam interaction volume) under the given operating conditions is approximately 1-2 μm in x and y and 2-3 μm in z. Therefore, nanometer scale intergrowths common with clay minerals cannot be resolved by SEM. The most probable clay minerals, based on SEM-EDS analysis, have been indicated in Table 5.

Table 5: Mineralogy of the Sandstones

Mineral and Formula	Berea Upper Gray	Carbon Tan	Crab Orchard
	Wt%	Wt%	Wt%
Quartz SiO_2	79 (85-90)	64	92 (92)
K-feldspar $KAlSi_3O_8$	10 (3-6)	15	√ (2)
Calcite $CaCO_3$	-	10	-
Dolomite $CaMg(CO_3)_2$	- (1-2)	11	-
Ankerite $Ca(Mg,Fe)(CO_3)_2$	√	-	-
Micas+illite e.g., $(K)(Al,Mg,Fe)_2(Si,Al)_4O_{10}[(OH)_2,(H_2O)]$	√ (1)	√	8 (4)
Kaolinite/Pyrophyllite e.g., $Al_2Si_2O_5(OH)_4$	√ (5-6)	√	√ (1)
Chlorite e.g., $(Mg_5,Al)(Al,Si_3)O_{10}(OH)_8$	11 (tr)	-	- (tr)
Ti oxide TiO_2	√	-	√
Fe oxide $Fe_x(O,OH)_x$	√	√	√
Zircon $ZrSiO_4$	√	√	√
Apatite $Ca_{10}(PO_4)_6(OH,F)_2$	-	√	-
Monazite $(Ce,La,Th,Ca)(PO_4)$	-	-	√

Semi-quantitative results are from XRD analysis at UNB. Values in brackets are taken from other references; Churcher et al. (1991) for the Berea sandstone and Kocurek Industries for the Crab Orchard sandstone. Check marks indicate mineral phases identified in SEM analysis but were below detection in the XRD analysis; "tr" means trace amounts have been identified in other references.

Anion exclusion is a result of the electrostatic repulsion of negative ions away from particle surfaces of like charge, such as clay particles, which usually have a permanent negative charge. This effect becomes particularly relevant with high clay content and small pore throats and is generally considered to be important in clay-rich media (Melkior et al. 2004; Bazer-Bachi et al. 2006; van Loon et al. 2007). The combination of relatively high porosity and low clay content in the Berea Upper Gray sandstone (ϕ_w = 0.196 and 11 wt% clays) and Carbon Tan sandstone (ϕ_w = 0.128 and trace amounts of clays) means that anion exclusion is not likely in those samples (Figure 9). With such high quartz content in the Crab Orchard sandstone, any anion exclusion that might occur is also expected to be negligible. Given the results of the mineralogical analyses, which show that clay contents are relatively low (no more than 11%), anion exclusion is expected to be negligible in these sandstones and it is assumed that $\phi_I = \phi_w$.

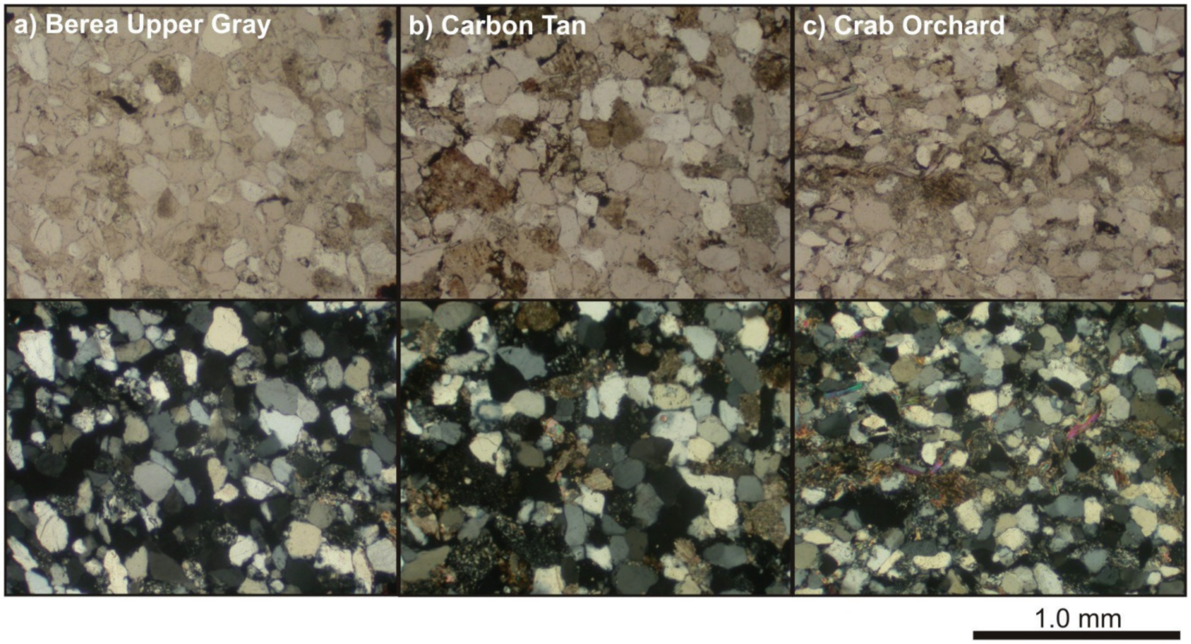

Figure 8: Micrographs from the (a) Berea Upper Gray, (b) Carbon Tan and (c) Crab Orchard Sandstones. Top Images are Transmitted Light Micrographs and Bottom Images are Corresponding Polarized Light Micrographs. Quartz is the Dominant Mineral in all Three Sandstones

3.1.3 Calibration Methods

To generate the calibration curves for the RAD technique, sets of 3 sandstone subcores (Berea, Carbon Tan and Crab Orchard) with different porosities (Table 4) were saturated first with synthetic porewater (SPW) and then with the corresponding tracer solution. Opalinus Clay synthetic porewater (OPA SPW) (van Loon et al. 2003a) and OPA I^- tracer were used for the calibration used in Opalinus Clay experiments, and S-SPW with its matching I^- tracer (Cavé et al. 2010) was used in the calibration for use with DGR shale samples (Table 6).

Two methods were used to acquire tracer-saturated $\Delta\mu$ values ($\Delta\mu_{sat}$). One method treated the calibration sandstones in the same manner as experimental samples, allowing the saturation to proceed by diffusion only. The other method was designed to saturate the sandstones with tracer solution more rapidly, by advectively displacing the pore fluid with tracer solution. In the first method, the sandstones were prepared in the same way as experimental samples, by coating them with silicone and encasing them in heat-shrink tubing and then mounting them in the diffusion cell as described in Cavé et al. (2010). Ceramic bars were affixed to the sides of the samples to replace the ceramic cap as an internal standard. The sandstones were saturated with SPW (Table 6) under vacuum until bubbles stopped evolving and then reference images of the sandstones were collected. Then the samples were saturated with I^- tracer solution from both ends by diffusion. Images were collected on a weekly basis until there were no further changes in the $\Delta\mu$ of the sandstones, i.e., when $\Delta\mu = \Delta\mu_{sat}$. Complete saturation of the sandstones required 3 to 4 weeks. The I^- tracer in the reservoirs was refreshed regularly during that time. Two I^- calibrations were performed with this method: 1) a calibration using the 0.39 M NaI OPA Clay tracer solution, and 2) a calibration using the 1 M I^- DGR Shale tracer solution (Table 6).

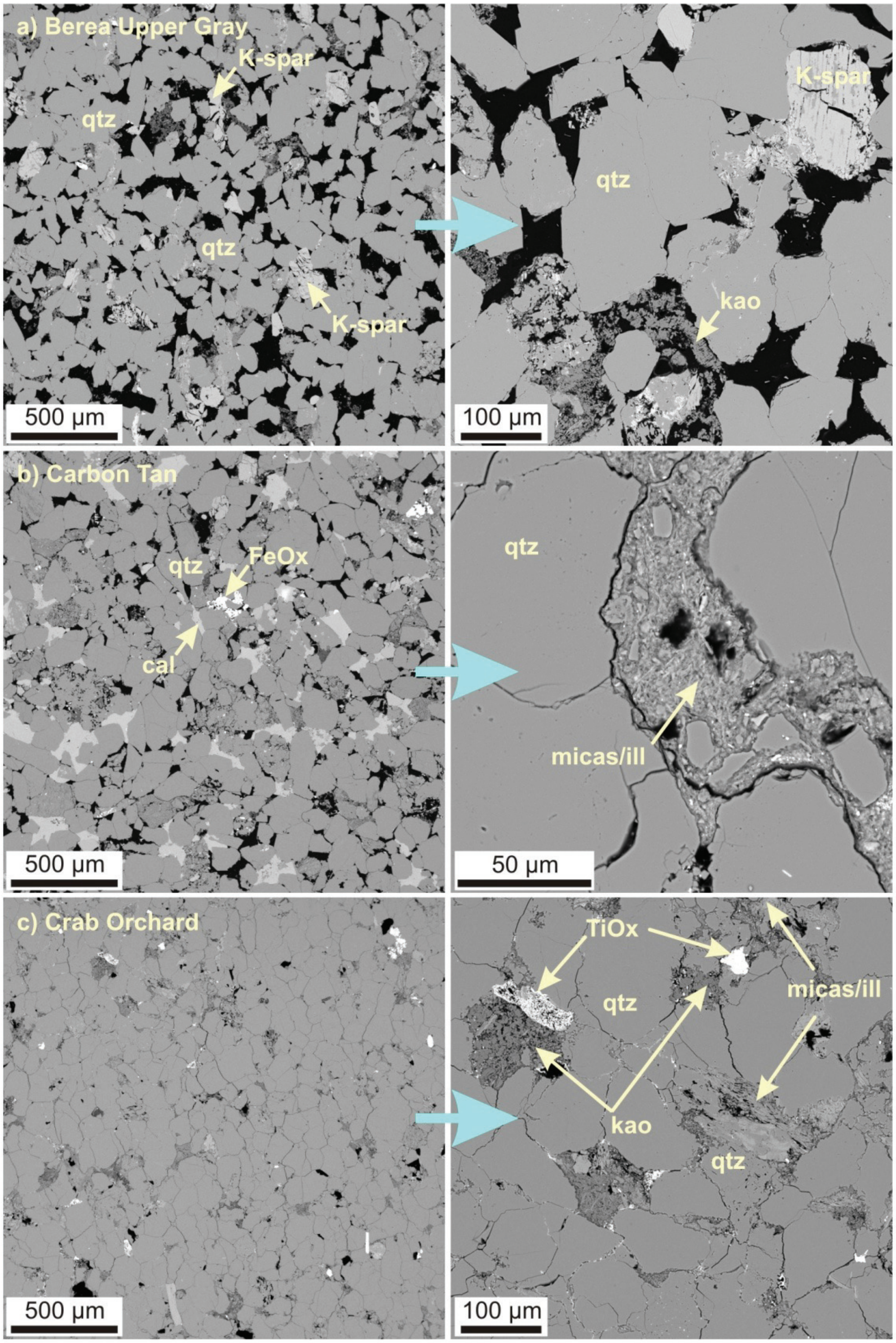

Figure 9: BSE SEM Images from the (a) Berea Upper Gray, (b) Carbon Tan, and (c) Crab Orchard Sandstones. K-spar = K-feldspar, qtz = Quartz, kao = Kaolinite (or Similar Clay), ill = Illite, cal = Calcite, FeOx = Fe Oxides, TiOx = Ti Oxides. The Images on the Right are Higher Magnification Images from the Areas Shown on the Left. Black Zones in the Images Represent Pores

Table 6: Composition of the Synthetic Porewater and Tracer Solutions Used in the Revised Calibration Method

	OPA SPW	OPA Tracers		S-SPW	DGR Shale Tracers	
		I^-	Cs^+		I^-	Cs^+
Na	0.240	0.39	0.240	2.400	2.400	-
K	0.002	-	0.002	0.500	0.500	0.500
Mg	0.017	-	0.017	0.250	0.250	0.250
Ca	0.026	-	0.026	1.201	1.201	1.201
Sr	0.001	-	0.001	-	-	-
Cl	0.300	-	2.800	5.800	4.800	5.800
SO_4	0.014	-	0.014	0.001	0.001	0.001
HCO_3	0.0005	-	0.0005	-	-	-
I	-	0.39	-	-	1.000	-
Cs	-	-	2.500	-	-	2.400

Units are Molar (mol/L). The composition of the OPA SPW was taken from van Loon et al. (2003a); rational for the tracer solution composition is provided in Section 4.3.1. The composition of the DGR Shale SPW and tracer solutions is from Cavé et al. (2010).

The time required for tracer saturation of the sandstones by diffusion was longer than desired (approximately 1 month), so the second method for saturating the samples by advective displacement was developed. The advective-displacement method was used with a duplicate set of sandstone subcores and the OPA solutions (Table 6). The results from the advective displacement method are included in the OPA I^- calibration data set. The sandstone subcores were first coated with Epofix™ epoxy and then inserted into advective-displacement cells (Figure 10).

The sandstones were received from Kocurek industries nominally dry. Therefore, the Berea and Carbon Tan cores were first purged with $CO_{2(g)}$ in the advective cells for approximately 4 hours and then flushed with 9 mL of SPW. The cells were then closed for 2 days to allow any $CO_{2(g)}$ remaining in the samples to dissolve in the SPW. Another 9 mL of SPW was flushed through the cells and the cells were closed again and allowed to sit overnight before commencing data collection. A volume of 9 mL is approximately 30 pore volumes for the Berea sandstone, and 50 pore volumes for the Carbon Tan sandstone. The Crab Orchard sandstone has much lower permeability and porosity, so the SPW saturation procedure was modified. The cores were flushed with $CO_{2(g)}$ for 3 hours, the cells were closed overnight and then flushed with $CO_{2(g)}$ for another 5 hours the following day. After saturation with $CO_{2(g)}$, the cells were connected to a peristaltic pump and de-aerated SPW was flushed through the cells. Approximately 20 pore volumes of SPW were pumped through the cores over 4 days. Advective displacement was conducted in a similar manner to exchange the SPW in the sandstones with the tracer solution. Tracer-saturation of the sandstones was verified by continued flushing of the sandstones with fresh tracer solution and repeatedly acquiring X-ray images until there were no further changes in the $\Delta\mu$ of the sandstones. Complete tracer-saturation using advective-displacement was confirmed in 4 days for the Berea and Carbon Tan sandstones and in 14 days for the lower permeability Crab Orchard sandstone.

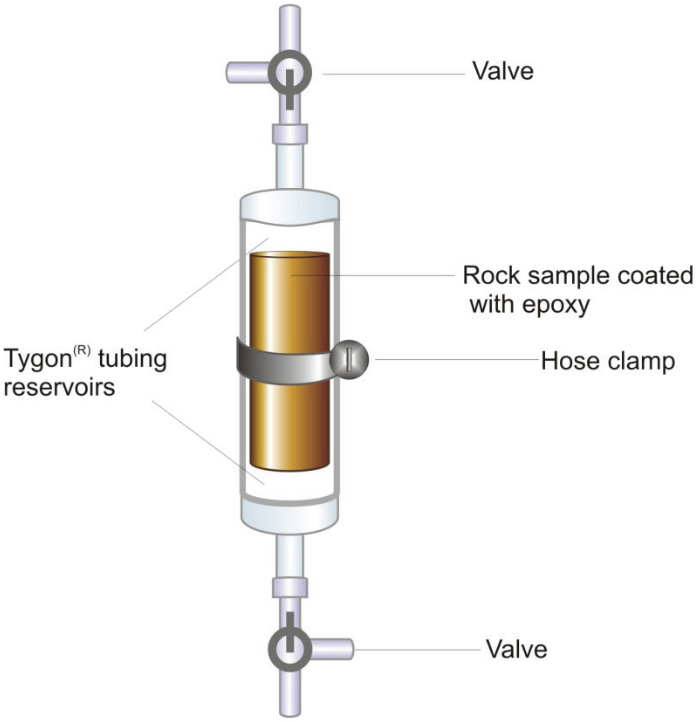

Figure 10: Schematic of the Advective-Displacement Cell Designed for Rapid Saturation of RAD Samples

The instrument operating conditions used for both the OPA Clay and the DGR Shale calibrations are listed in Table 7.

Table 7: X-ray Radiography Data Acquisition Parameters for Calibration and Diffusion Tests Using the SkyScan 1072 MicroCT

Parameter	Settings
Data collection	3 replicate reference images
Energy	60 kV for OPA and 90 kV for DGR Shale solutions
Current	163 μA for OPA and 110 μA for DGR Shale solutions
Acquisition time	9968 ms
Frame-averaging	8
Filter	1 mm Al between source and sample
Flat field correction	On
Image settings	16-bit TIFF, 1024x1024 pixels, 2MB
Magnification	14 x

3.2 MANUFACTURED CERAMICS

Calibration with Cs^+ tracer cannot be performed with natural sandstones because of the adsorption of Cs^+ on sandstones; alternative materials are required. Manufactured non-porous ceramics offer a controlled, reproducible composition and can be machined to specifications. Two ceramics were tested for the radiography calibration. The ceramics selected were, Macor® by Corning and the Mykroy/Mycalex® ceramic previously used as the internal standard cap on RAD samples (hereafter referred to as Mycalex®). The ceramics were selected based on the similarity of their X-ray attenuation properties with common rock-forming minerals (Figure 11). The Macor® ceramic corresponds with quartz and albite, while the Mycalex® is similar to calcite. The Mycalex® ceramic is considered most representative of the DGR sample material while the average of the Macor® and Mycalex® is considered most representative of the Opalinus Clay. The linear attenuation coefficients plotted in Figure 11 were calculated from the National Institute of Standards and Technology XCOM database (http://physics.nist.gov/PhysRefData/Xcom/html/xcom1.html).

Four cores (11 mm diameter) from each ceramic were drilled along the cylinder axis with holes of different diameters to create equivalent volumetric porosities (Figure 12). The bottoms were fitted with removable plugs to contain the calibration solutions. The simulated porosity of each core was measured in the radiographs using ImageJ software. The ceramic vial calibrations were performed for both I^- and Cs^+ tracer solutions (Table 6).

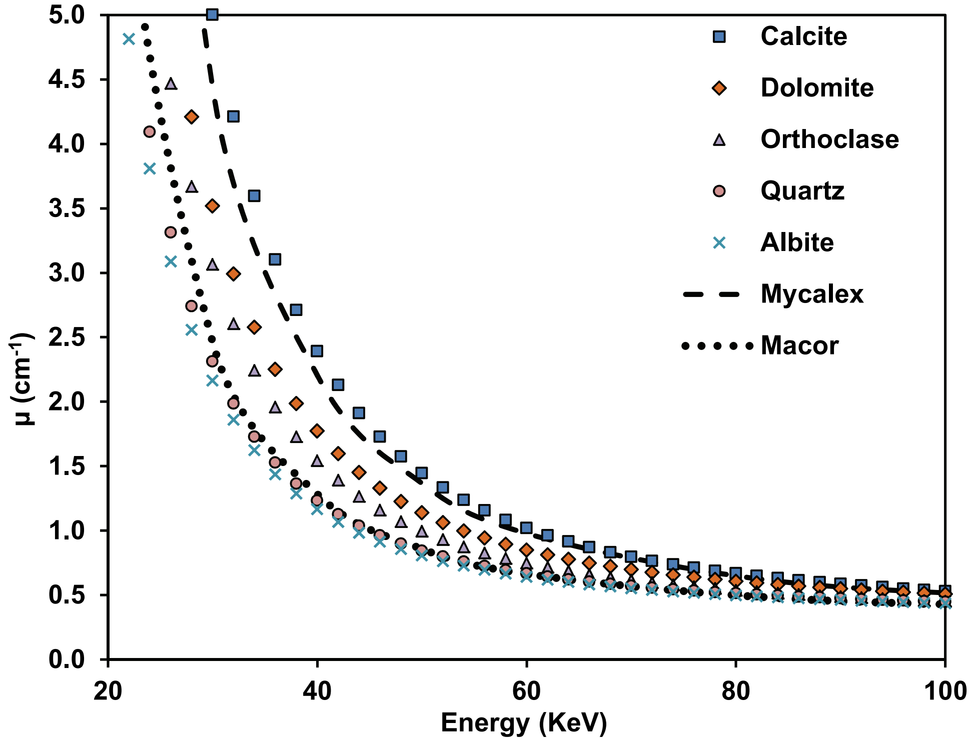

Figure 11: Plot of Linear X-ray Attenuation Coefficients versus Photon Energy for Common Rock-Forming Minerals and the Mycalex® and Macor® Ceramics

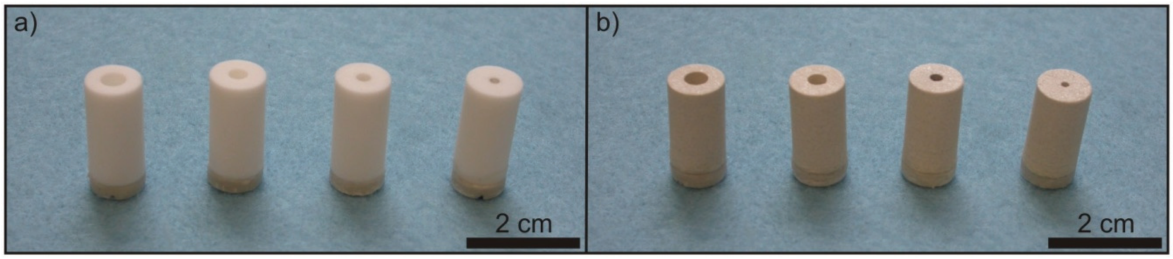

Figure 12: Images of the (a) Macor® and (b) the Mycalex® Ceramic Standards. The Holes Through the Centers, from Left to Right, Represent Nominal 17%, 10%, 5% and 2% Porosity, Respectively. All Standards in the Images have a Mycalex® Cap Affixed at the Bottom

3.3 THE IODIDE TRACER CALIBRATION

The I^- calibration curves for the OPA Clay and DGR Shale using different standard materials – sandstones, ceramics and glass vials – are presented in Figure 13 and Figure 14, respectively. The glass vial calibrations were performed as previously described, by varying the I^- concentration in a series of standard solutions and measuring the change in Δμ (Cavé et al. 2010; Al et al. 2012). Both the sandstone and the ceramic calibrations are based on the change in Δμ with changing porosity. However, for ease of comparison, the calibration curves have been recalculated to present the change in Δμ versus I^- concentration. Table 8 provides the calibration function for each of the matrix materials for both the Opalinus Clay and the DGR Shale solutions.

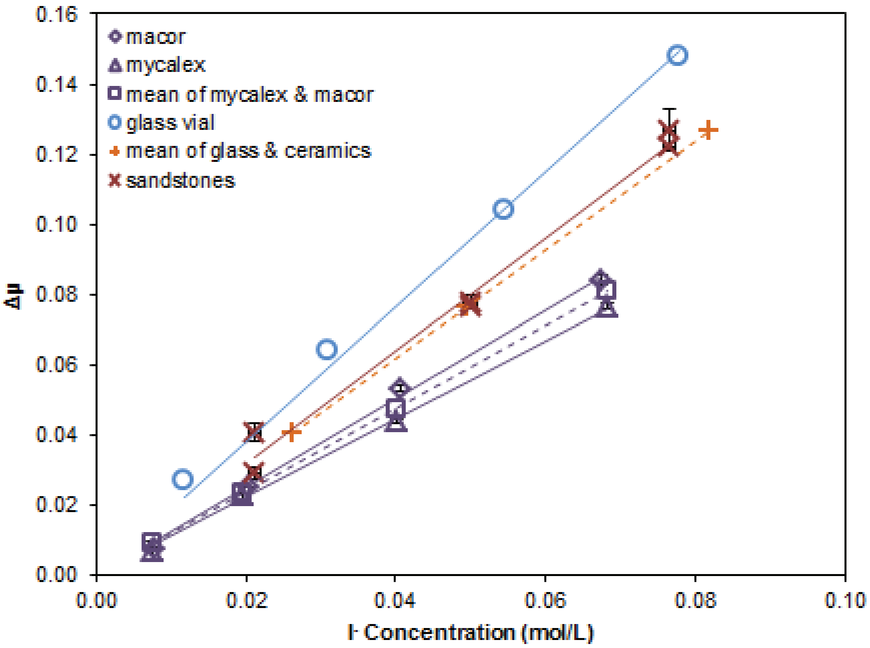

Figure 13: Opalinus Clay Radiography Calibration Curves for I^-; 60 kV X-ray Source

The glass vials were least affected by beam hardening and therefore display the highest slope, while the ceramics, with the “porosity” concentrated in the center of the standard, were most affected by beam hardening and therefore display the lowest slope (Figures 13 and 14). The sandstones have a natural porosity distribution and the calibration slope is virtually midway between the glass vial and ceramic curves. Two sets of sandstones were used in the Opalinus Clay calibration and the heterogeneity of the natural sandstones is apparent in the results, particularly for the low porosity (low I^- concentration) Crab Orchard sandstone (Figure 13). The natural mineral and porosity distributions in the sandstones provide the best possible representation of beam hardening characteristics in porous geologic media. Therefore, the sandstone calibration curve is most appropriate for quantifying the results of radiographic measurements. The effect of the change in the RAD calibration method has on the measured values ϕ_I and D_{eI} for the DGR samples is presented and discussed in detail in Al et al. (2012).

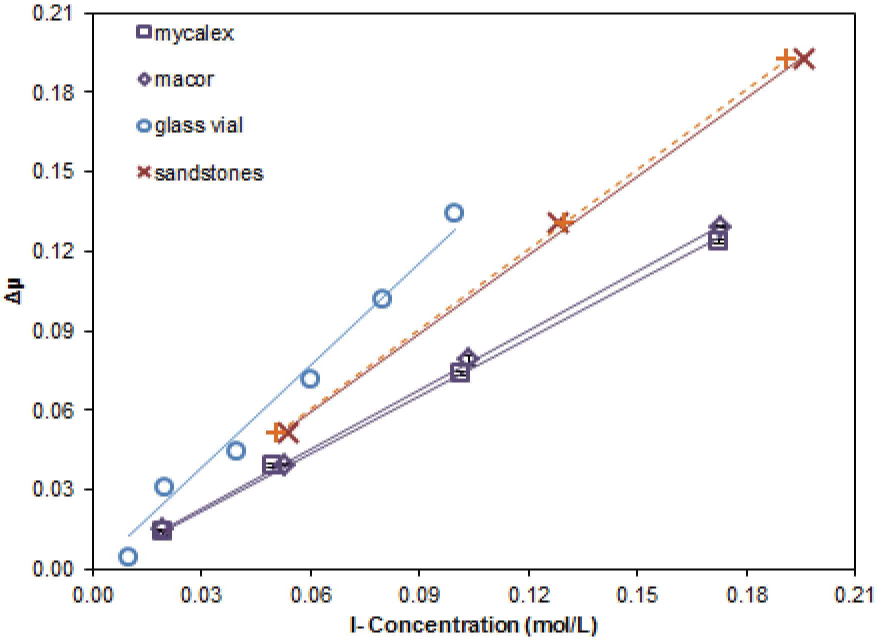

Figure 14: DGR Shale Radiography Calibration Curves for I^-; 90 kV X-ray Source

3.4 THE CESIUM TRACER CALIBRATION

Cavé et al. (2010) investigated the potential for radiographic measurement of reactive solute transport parameters (pore diffusion coefficient, D_{pCs}; selectivity coefficient, log $K_{Cs+/Na+}$; and cation exchange capacity, CEC) using Cs^+. The method relies on a calibration function relating the Cs^+ concentration to Δμ. Cavé et al. (2010) performed the calibration in glass vials containing standard solutions of varying Cs^+ concentration in SPW. With the discovery of the beam hardening artefact in the calibration method for I^- concentrations, the Cs^+ calibration method also required modification.

Table 8: Radiography Calibration Functions for I^- in Different Solid Matrices

Calibration Matrix	Equation	R^2
Opalinus Clay		
Macor®	y = 1.26x	0.9965
Mycalex®	y = 1.12x	0.9989
Mean of mycalex® and macor®	y = 1.19x	1
Glass vial	y = 1.91x	0.995
Mean of glass vial and ceramic	y = 1.55x	1
Sandstones	**y = 1.60x**	**0.9865**
DGR Shale		
Macor®	y = 0.75x	0.9997
Mycalex®	y = 0.73x	0.9984
Glass vial	y = 1.28x	0.9816
Mean of glass vial and mycalex®	y = 1.00x	1
Sandstones	**y = 0.99x**	**0.9977**

Although the sandstone standards provide the best matrix for calibration with I^-, they cannot be used for calibration of Cs^+ concentrations because Cs^+ adsorbs strongly to mineral surfaces. In that case, the X-ray attenuation is a function of adsorbed and aqueous Cs^+, and the total mass (concentration) of Cs^+ in a sample is unknown. In order to circumvent this problem, we exploit the relationships between the I^- calibration functions for the glass vial, sandstone and ceramic matrices and apply them to the Cs^+ calibration. Adsorption of Cs^+ is not an issue when measurements are conducted with either glass vials or the ceramics, so the calibration curve for Cs^+ in the "sandstone" is calculated from the known relationships between the calibration curves from the glass vials, sandstones and the ceramics for I^-. This approach is justifiable because, at a given X-ray source potential, the differences among the slopes of the calibration curves for the glass vials, sandstones and ceramics are due to differences in the beam hardening characteristics of the materials. These material properties are constant regardless of the composition of the filling solution.

The glass vial and ceramic calibrations for Cs^+ were carried out in the same manner as the I^- calibrations (Sections 3.2 and 3.3), using both Opalinus Clay (Figure 15) and DGR Shale (Figure 16) solutions. The equivalent sandstone curve for Cs^+ was calculated. The instrument operating parameters (Table 7) were also the same as those used in the I^- calibrations. The Cs^+ calibration curves for the ceramics were not straight lines, so a straight-line approximation through the lowest concentration points was used (Figures 15 and 16). It may be that, as the surface area to volume ratio in the centre holes of the ceramic standards decreases with increasing hole diameter, the relative effect of minor Cs^+ sorption onto the walls of the ceramic vial decreases. This would result in smaller than expected increases in $\Delta\mu$. Table 9 provides the Cs^+ calibration function for each of the matrix materials for both the Opalinus Clay and the DGR Shale SPWs.

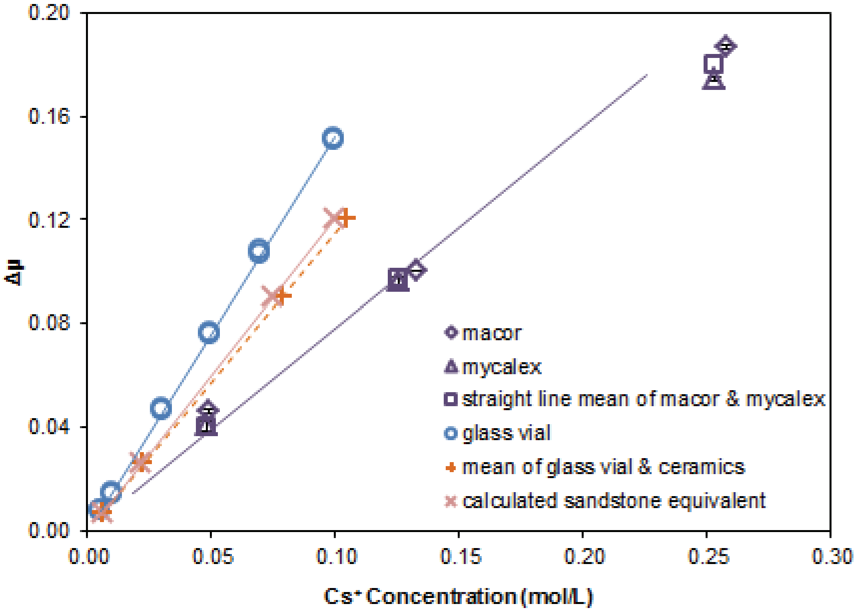

Figure 15: Opalinus Clay Calibration Curves for Cs$^+$ Developed Using Different Calibration Matrices; 60 kV X-ray Source

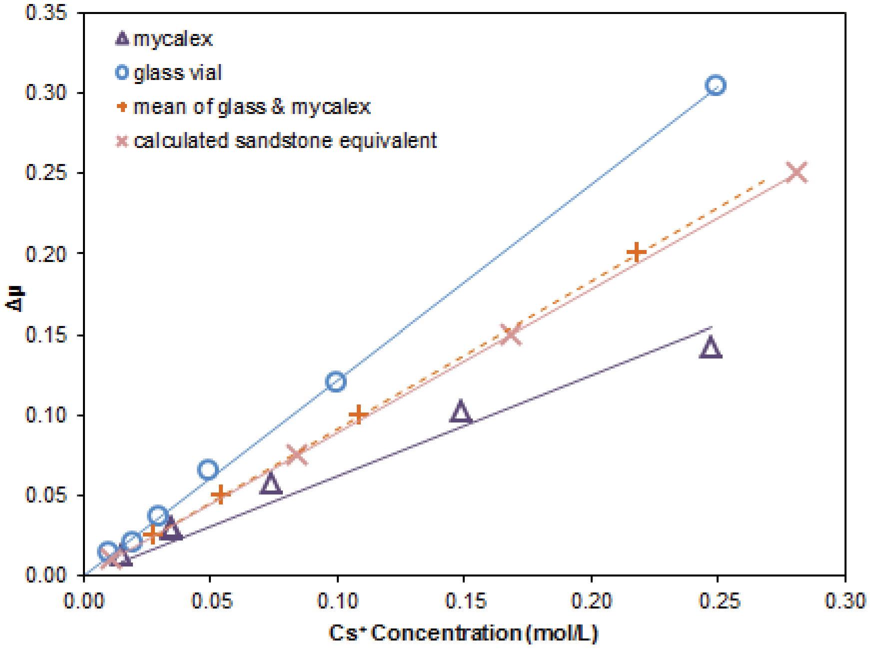

Figure 16: DGR Shale Calibration Curves for Cs$^+$ Developed Using the Different Calibration Matrices; 90 kV X-ray Source

Table 9: Radiography Calibration Functions for Cs^+ in Different Solid Matrices

Calibration Matrix	Equation	R^2
Opalinus Clay		
Mean straight line of mycalex® and macor®	$y = 0.78x$	0.997
Glass vial	$y = 1.52x$	0.9997
Mean of glass vial and ceramic	$y = 1.15x$	1
Calculated sandstone equivalent	**$y = 1.20x$**	**1**
DGR Shale		
Straight line of mycalex®	$y = 0.62x$	0.9619
Glass vial	$y = 1.21x$	0.9992
Mean of glass vial & mycalex®	$y = 0.92x$	1
Calculated sandstone equivalent	**$y = 0.89x$**	**1**

3.5 SUMMARY

The use of standard solutions in glass vials for calibration leads to an underestimation of the I^- mass in rock samples, and consequently underestimates ϕ_I and D_{eI}. A new calibration method was developed to provide a better match between the beam hardening characteristics of the calibration materials and rock sample matrices. Two types of calibration materials were investigated: ceramics and natural sandstones. The natural sandstones best reflect the beam hardening resulting from the distributed porosity common in natural samples. Therefore, the calibration function based on the sandstones is considered the most appropriate for use in measuring the I^- concentration and ϕ_I in porous rock samples. The natural sandstones were not suitable for the Cs^+ calibration because Cs^+ adsorbs to the mineral surfaces and there is no way to quantify the mass of adsorbed Cs^+ accumulated within a sample after equilibration with a tracer solution. To avoid this problem, the relationships between the calibration functions for the glass vial, the sandstones, and ceramics observed in the I^- calibration were exploited to develop a calibration function for Cs^+.

4. MEASUREMENT OF DIFFUSION PROPERTIES BY X-RAY RADIOGRAPHY USING IODIDE AND CESIUM TRACERS: OPALINUS CLAY

To date, the development of the radiographic technique for measuring diffusion properties in sedimentary rock has been focused on samples from the Michigan Basin (Cavé et al. 2009a, b; Cavé et al. 2010; Al et al. 2012). As part of the method development, measurements made by the RAD technique were compared against measurements on the same core segments using the through-diffusion technique (Cavé et al. 2009a, b). The results from the two techniques were found to be comparable, verifying the radiography technique. In 2010, an opportunity arose to apply the radiography technique to Opalinus Clay samples retrieved from the Mont Terri Underground Research Laboratory (URL) in Switzerland (Figure 17). Opalinus Clay has been extensively studied through the Mont Terri Project and therefore provides a good opportunity to compare the RAD technique with other methods.

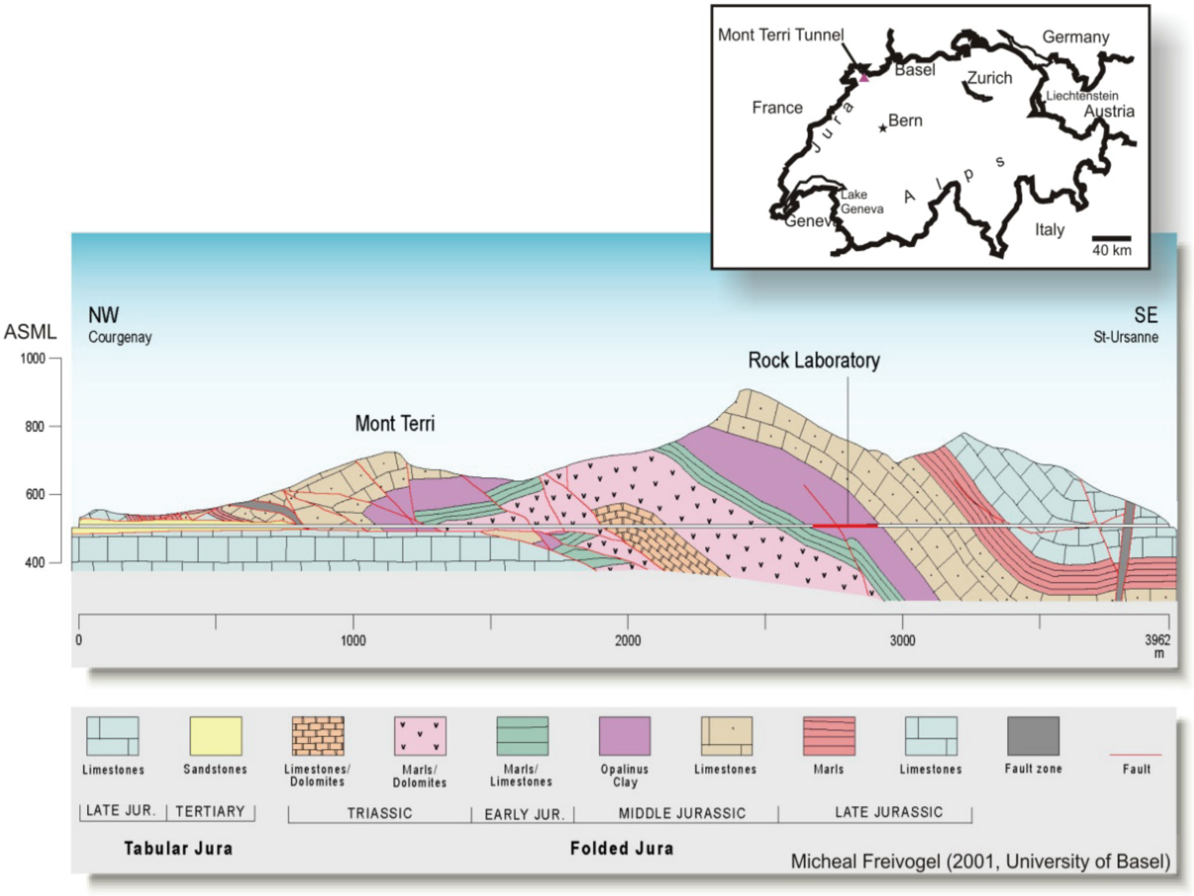

Figure 17: Location of the Mont Terri Tunnel and URL in Switzerland and Bedrock Geology of Mont Terri. Source: http://www.mont-terri.ch

4.1 MONT TERRI URL DESCRIPTION

The Mont Terri Project is an international research project for the hydrogeological, geochemical and geotechnical characterization of the Opalinus Clay (http://www.mont-terri.ch). The goal of the project is to provide input for assessing the feasibility and safety of a repository for radioactive (or chemotoxic) waste in this type of host rock. The research and development aspects of this project are concerned with testing and further development of investigation technologies. Therefore, the testing of the RAD method with the Opalinus Clay is consistent with this goal.

The URL is located 300 m below the surface, in the security gallery of the Mont Terri motorway tunnel under the Swiss Jura Mountains, in the Canton of Jura, north-western Switzerland (Figure 17). The Middle Jurassic age Opalinus Clay was selected for the URL because of its low permeability - transport is dominated by diffusion within the formation - and the presence of minimal tectonic deformation.

4.2 SAMPLE MATERIAL

There have been many diffusion and sorption studies carried out as part of the Mont Terri Project, including laboratory, in situ and modeling experiments (e.g., Palut et al. 2003; van Loon et al. 2003a, b; van Loon et al. 2004; Wersin et al. 2004; Wersin et al. 2008; Jakob et al. 2009; van Loon et al. 2009; Appelo et al. 2010). The location of and/or the source material for these diffusion and sorption studies was the DI niche in the URL (Figure 18).

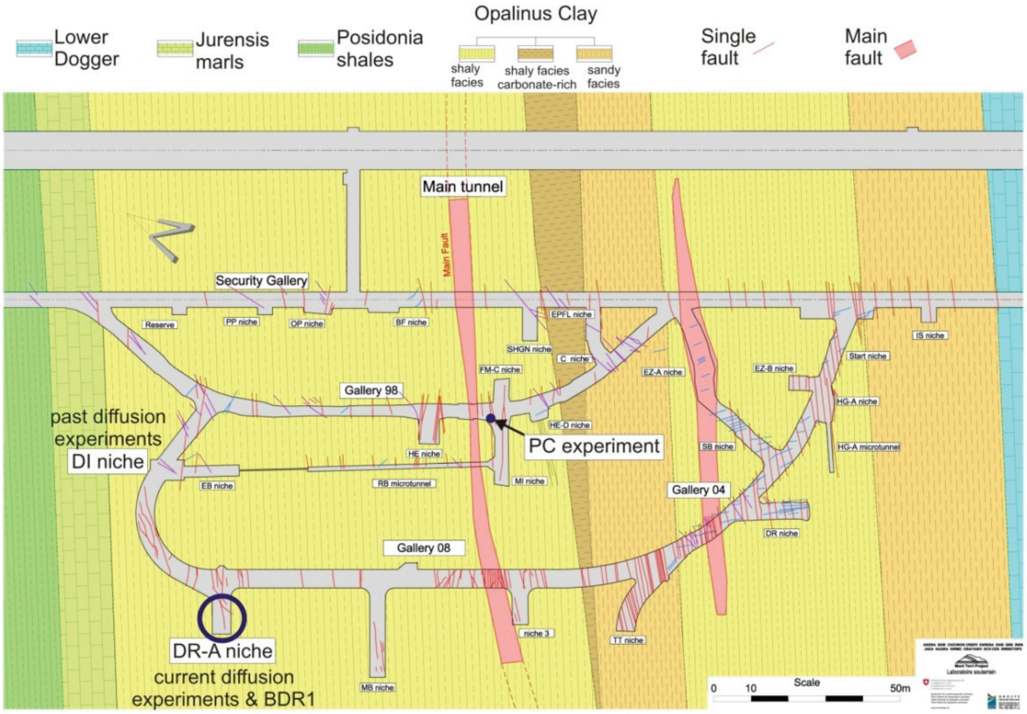

Figure 18: Geology of the Mont Terri URL and Location of the DR-A Experiment

In 2009, in situ DR-A (diffusion, retention and disturbances) experiments were initiated in the DR-A niche (Figure 18). The sample material provided to UNB was recovered from an overcored borehole (BDR1) related to the DR-A diffusion experiment. However, when making comparisons with published literature, the UNB results will be compared with diffusion data from the DI niche because the diffusion data from the DR-A experiments were not available. The two niches are approximately 50 m apart and are located in the same facies of the Opalinus Clay (Figure 18), and therefore, the results from the two niches should be comparable.

Three samples of Opalinus Clay (Figure 19) were provided to UNB for diffusion experiments. The typical mineralogy and selected physical properties of the Opalinus Clay are provided in Table 10. The samples submitted to UNB were collected on 19 January, 2010, and are identified below. The sample depths are given in meters below the tunnel floor (mbtf).

- BDR1_OC 1a: 5.3-5.5 mbtf, 0.20 m long, 0.045 m diameter, long axis normal to bedding;
- BDR1_OC 2: 5.57-5.68 mbtf, 0.065 m long, 0.290 m diameter; and,
- BDR1_OC 3a: 5.8 mbtf, 0.20 m long, 0.045 m diameter, long axis parallel to bedding.

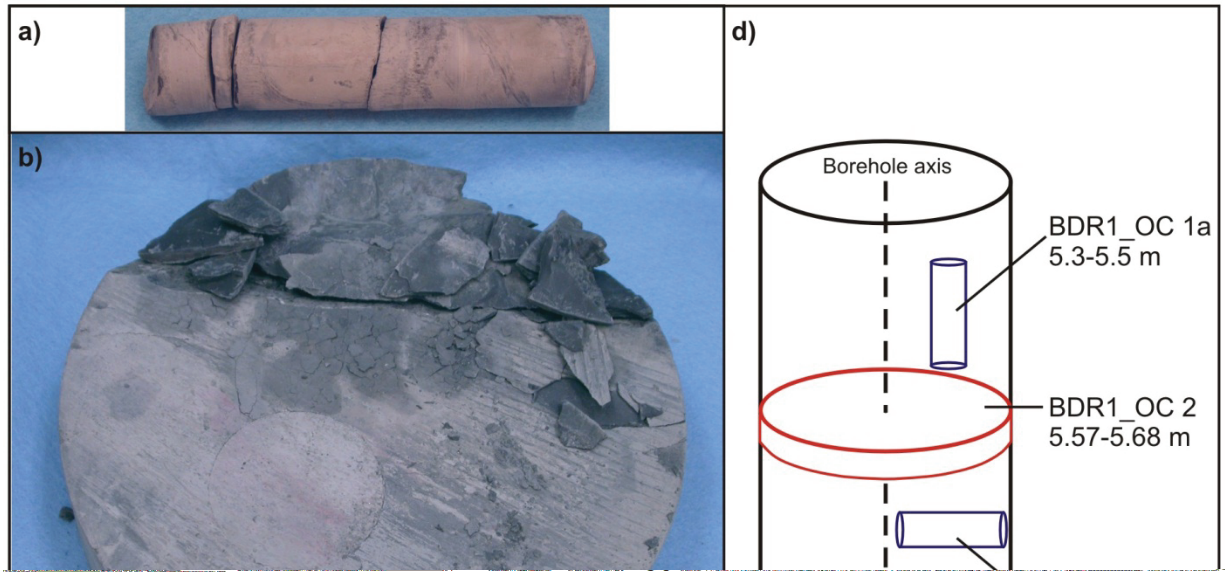

Figure 19: Examples of Opalinus Clay Samples (a) BDR1_OC 1a, (b) BDR1_OC 2, (c) BDR1_OC 3a and (d) an Illustration of the Relative Location and Orientation of the Core Samples in BDR1_OC. The Scale is the Same in Images (a), (b) and (c), While (d) is Not Drawn to Scale. Depths are Given in Meters Below the Tunnel Floor

Table 10: Typical Mineralogy and Selected Physical Properties of Opalinus Clay from Mont Terri, Switzerland

Parameter	**Opalinus Clay at Mont Terri**
Total Clay minerals (wt%)	58 – 76 (66)
Illite	*16 – 40 (26)*
Kaolinite	*6 – 33 (20)*
Illite/smectite	*5 – 32 (16)*
Chlorite	*4 – 20 (9)*
Quartz (wt%)	6 – 24 (13)
Feldspars (wt%)	2 – 4 (3)
Calcite (wt%)	5 – 28 (13)
Dolomite/ankerite (wt%)	0.2 – 2.5
Siderite (wt%)	1 – 5 (3)
Pyrite (wt%)	0.6 – 1.7
Organic carbon (wt%)	<0.1 – 1.5
CEC (meq/100g rock)	11.1
	11.7 – 12.4[a] intact rock (by modeling ^{22}Na diffusion)
	9.45 ± 0.7[b] crushed rock (by Σcations)
	12.09 ± 3.6[c] crushed rock
	10.15 ± 1.6[c] crushed rock (by Σcations)
	9.45 – 16.92[d] crushed rock (multiple methods)
	10.4 – 11.6[e] crushed rock
Porewater type	Na-Cl-SO_4
Bulk dry density (g/cm^3)	2.2 – 2.4[d]
Physical porosity	0.16 (0.15 – 0.18[d])
Anion-accessible porosity	0.09
$D_{e\text{-}NB}$ (HTO; m^2/s)	1.5 x 10^{-11}, anisotropy ratio 5
$D_{e\text{-}NB}$ (Cl^-; Br^-; I^-; m^2/s)	4.1 x 10^{-12}, anisotropy ratio 6
Swelling pressure (MPa)	1.2 (NB), 0.5 (PB)

Data sourced from Mazurek et al. (2008) unless otherwise indicated. Mazurek et al. (2008) give values considered representative of the Opalinus Clay at Mont Terri.

Mineralogical data represent the range of values reported in the literature and an approximate average of those values in brackets. Values for individual clay minerals represent wt% of the total clay content. When available, values for the shaly facies were used. Data sources: Pearson et al. (2003) and references cited therein, Mazurek et al. (2008), van Loon et al. (2009), Appelo et al. (2010), Koroleva et al. (2011).

Diffusion coefficients ($D_{e\text{-}NB}$) were measured normal to bedding at ambient laboratory temperature (ca. 22°C).

[a] Appelo et al. (2010); [b] Bradbury and Baeyens (1998); [c] Lauber et al. (2000); [d] Pearson et al. (2003) and references cited therein; [e] Koroleva et al. (2011).

4.3 METHODS

4.3.1 Experimental Solutions

The composition of the synthetic porewater (Table 11) used to re-saturate the OPA Clay material after sample preparation was obtained from van Loon et al. (2003a; 2009).

4.3.1.1 Iodide Tracer Solution

The radiography technique for diffusion measurements requires an I^- tracer solution with an I^- concentration that is high enough to produce a satisfactory signal-to-noise (S/N) ratio. However, it is also important to match the ionic strength of the tracer solution to the ionic strength of the porewater so that osmotic effects will not influence the diffusion measurements. It is not possible to match the chemical composition of the tracer solution to the OPA SPW (with the ionic strength of 0.39 M) and, at the same time, keep the I^- tracer concentration high enough to meet S/N ratio requirements. As a result, a 0.39 M NaI tracer (ionic strength = 0.39 M) was used without matching the chemical composition of the OPA SPW. The possible influence of calcite dissolution on porosity changes was assessed with geochemical modelling using PHREEQC Version 2.17.3 (Parkhurst and Appelo 1999). The results suggest that there would be negligible change in the porosity of the sample (Appendix A).

Table 11: Composition of the Synthetic Porewater and Tracer Solutions Used with the Opalinus Clay

	OPA SPW (M)	**I Tracer (M)**	**Cs Tracer 1 (M)**	**Cs Tracer 2 (M)**	**Cs Tracer 3 (M)**
Na	0.240	0.39	0.240	0.240	0.240
K	0.002	-	0.002	0.002	0.002
Mg	0.017	-	0.017	0.017	0.017
Ca	0.026	-	0.026	0.026	0.026
Sr	0.001	-	0.001	0.001	0.001
Cl	0.300	-	0.310	0.301	0.3002
SO_4	0.014	-	0.014	0.014	0.014
HCO_3	0.0005	-	0.0005	0.0005	0.0005
I	-	0.39	-	-	-
Cs	-	-	0.010	0.001	0.0002
Ionic strength	0.39	0.39	0.40	0.39	0.39

The composition of the OPA SPW was taken from van Loon et al. (2003a).

4.3.1.2 Cesium Tracer Solutions

In published literature, the Cs^+ concentrations used to investigate Cs^+ sorption have ranged from 10^{-9} to 10^{-1} M; Cs^+ concentrations are not expected to exceed 10^{-3} M in the repository environment (Bradbury and Baeyens 2000). Additionally, Bradbury and Baeyens (2000) suggested that the relative importance of different binding sites varies with changing Cs^+ concentration. The goal, then, of this work was to use a range of relevant Cs^+ concentrations. Three tracer solutions were prepared in OPA SPW matrix with Cs^+ concentrations of 0.01, 0.001 and 0.0002 M (Table 11). The 0.01 M Cs^+ concentration was selected to provide data with a high S/N ratio. The 0.001 M Cs^+ concentration was selected to be consistent with in situ and laboratory experiments on the Opalinus Clay (van Loon et al. 2004; Wersin et al. 2008; Jakob et al. 2009), and the 0.0002 M Cs^+ was considered the lowest practical concentration for the radiography method. The Cs^+ was added to the OPA SPW in the form of CsCl. The concentrations of all other constituents were the same for the three tracer solutions.

4.3.2 Sample Preparation

Eight subcores were prepared for the I^- tracer experiments from the BDR1-OC 1a and 2 core segments. An additional four subcores from the BDR1-OC 1a, and eight from the BDR1-OC 2 core segment were prepared for the Cs^+ tracer experiments. Six of the subcores used in the I^- experiments were re-used in the Cs^+ experiments, giving a total of 18 subcores for the Cs^+ experiments. Subcores were prepared in both the normal-to-bedding (NB) and the parallel-to-bedding (PB) orientations. The sample labels, 5.3 NB or PB and 5.57 NB or PB, correspond to the core segments BDR1-OC 1a and 2, respectively (Figure 19).

The OPA Clay samples were initially prepared using a Dremel® rotary tool, but due to sample breakage, the method was modified to use a drill bit with compressed air, rather than water, as the lubricating fluid. This modification proved successful, reducing sample preparation time and breakage. All BDR1 5.3 series samples and sample BDR1 5.57 NB3 were prepared using the Dremel® tool; all other BDR1 5.57 series samples were prepared using the coring drill bit.

The cylindrical subsamples (nominal 11 mm diameter, and 11.5 to 19.1 mm length) were prepared from BDR1-OC core slices and mounted in the RAD diffusion cells as described in Cave et al. (2010) and Al et al. (2012). The surface of the samples was brushed with a thin coat of silicone and immediately enclosed in heat-shrink tubing (3M FP-301). An 11 mm diameter piece of felt and a non-porous ceramic disc (11 mm diameter, 3 mm height; Mykroy®/Mycalex® ceramic) were placed on top of each subsample inside the heat shrink tubing and the tubing was gently heated. The fabric ensures even and complete wetting of the sample surface with the experimental solutions. The ceramic disc is used as an internal standard to correct for variability in the X-ray source. The samples were then attached to the reservoirs (Figure 20) and sealed in with silicone. Two thin plastic wires were fixed vertically to the side of the shrink tubing as alignment guides.

After they had been mounted in the diffusion cells and the silicone allowed to cure overnight, the samples were re-saturated under vacuum with OPA SPW. This was done to ensure that any surficial drying that may have occurred during sample preparation was eliminated. Throughout the course of the experiments, all of the samples were stored in sealed containers with an open dish of OPA SPW to prevent evaporation from the diffusion cells (Figure 21).

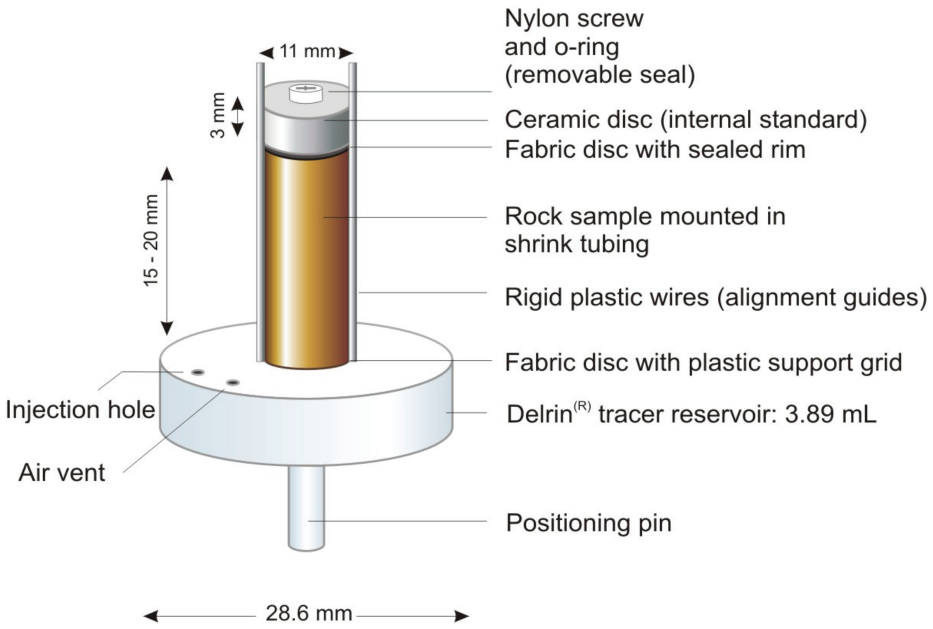

Figure 20: Diagram of the Cell Used for Diffusion Experiments by Radiography

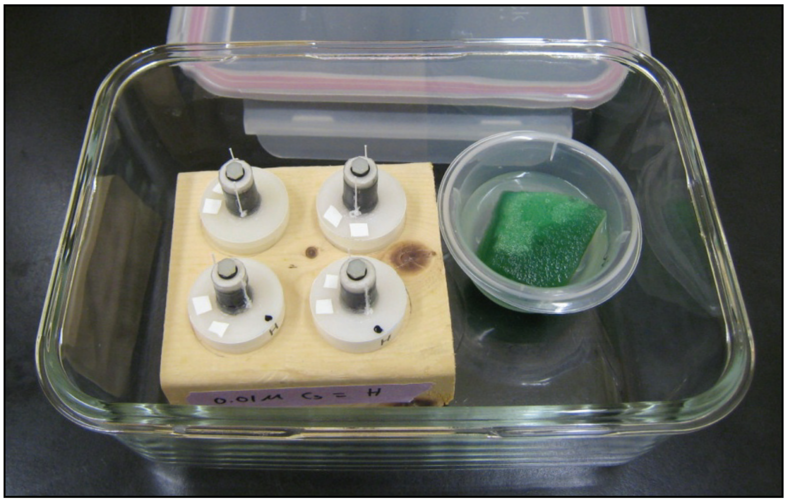

Figure 21: Diffusion Cells Used in the Radiography Experiments

The Opalinus Clay samples swelled in the diffusion cells upon initial saturation with SPW. Swelling was indicated by lifting and breakage of the silicone seal at the base of the diffusion cell, and expansion of the sample diameter. The swelling resulted in variable degrees of disaggregation in the bottom 1 to 2 mm of the samples and had minimal effect at the top of the sample (Figure 22). Once re-saturated with SPW, the samples appeared to stabilize and no further changes were observed.

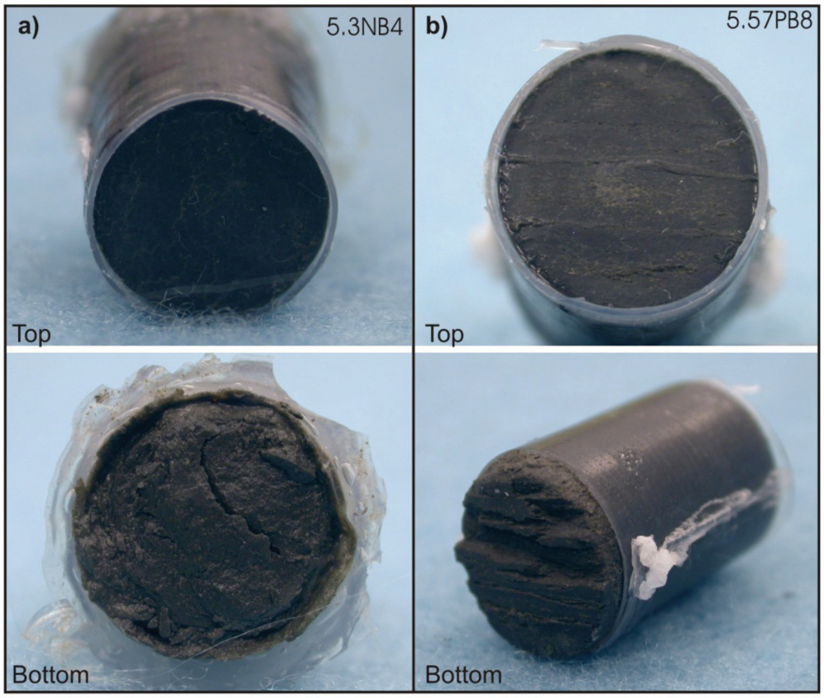

Figure 22: Images of Subcores After Completion of the Radiography Experiments. Subcores have a Nominal 11 mm Diameter

To investigate the possible effects of swelling on the radiography results, and to advance the radiography method for use with swelling and/or disaggregated samples, a modification to the radiography diffusion cell was designed and fabricated (Figure 23). The heat-shrink tubing was replaced with a 1 mm-thick Delrin® sleeve, and 3 mm-thick top and bottom plates made of Delrin® were added. Nylon nuts and rods were used to hold the plates together. The contact between the sample bottom and the solution reservoir was changed from an open hole with a plastic support grid to a solid piece of Delrin® with 5 holes drilled in it to allow for solution transfer between the reservoir and the sample. Delrin® and nylon were used because they do not corrode in brine solutions and they have low X-ray attenuation properties. The ceramic cap internal standard was replaced with two ceramic bars fixed to the outside of the Delrin® sleeve. The size of the modified cell was constrained by the size of the sample chamber in the SkyScan microCT. One subcore sample from the BDR1-5.57 core (5.57 NB13) was tested using this new RAD confining cell.

When the sample in the RAD confining cell was re-saturated with SPW, the rigid Delrin® prevented sample disaggregation at the bottom. However, the Delrin® was not strong enough to prevent all swelling – the top plate bowed upwards slightly as a result of the swelling pressure (Figure 24). With this cell design, the confining pressure is not directly controlled, as with conventional geomechanical tests that use confining vessels to apply pressure and load cells and/or pressure transducers to monitor the applied pressure. Instead, the confining pressure in the modified RAD cell develops as a result of the swelling of the clay against the sides of the Delrin® cell when the sample is wetted, and the pressure is not monitored. Therefore, the resultant confining pressure will be less than or equal to the swelling pressure of the clay, which Mazurek et al. (2008) have reported to be 0.5 MPa in the PB orientation and 1.2 MPa in the NB orientation for Mont Terri Opalinus Clay in OPA SPW.

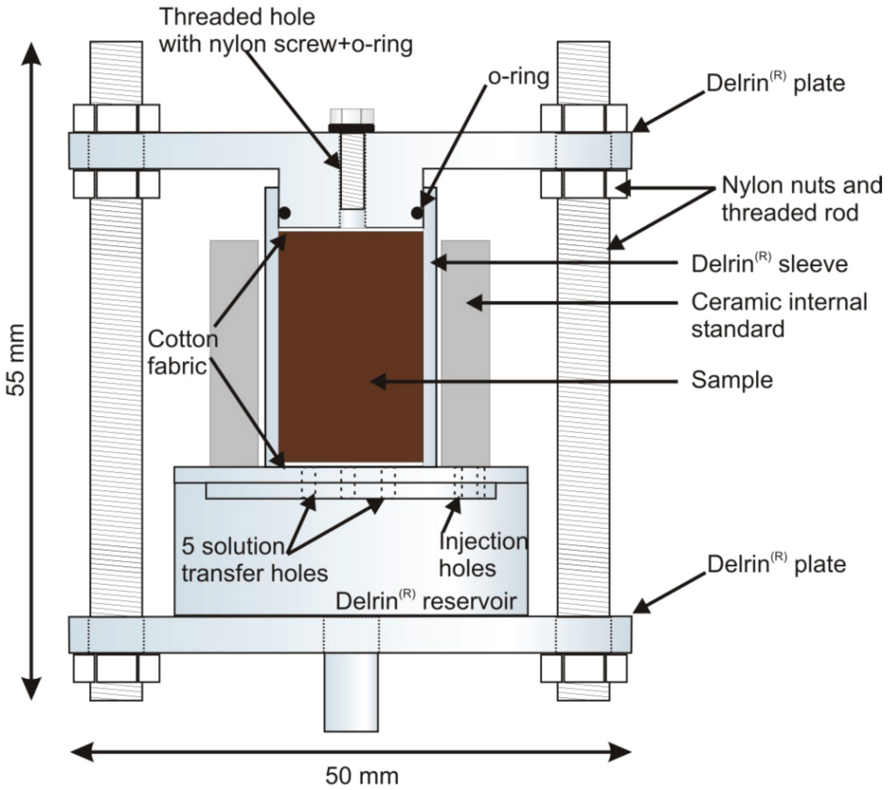

Figure 23: Diagram of the Confining Diffusion Cell for Use with Swelling or Disaggregated Samples in Radiography Experiments

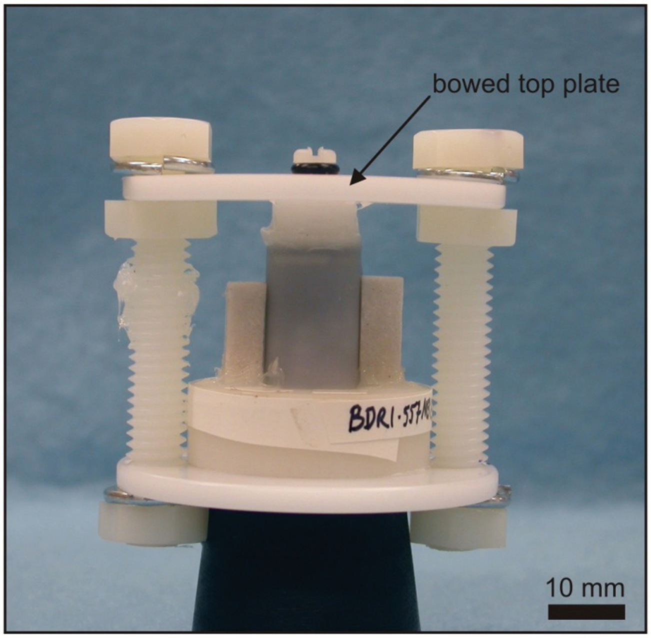

Figure 24: Image of the Confining Diffusion Cell after Saturation of the OPA Sample

4.3.3 Measuring Conservative Tracer Diffusion by Radiography

Diffusion experiments were initiated by replacing the SPW in the reservoirs (Figures 20 and 23) with tracer solution containing 0.39 M I^-. A total of 15 – 20 mL of tracer solution was used to flush and refill the reservoirs (i.e., >3 x's the reservoir volume). Replicate reference radiographs (time = 0) were collected immediately after the tracer solutions were introduced, and 3 to 4 time-series radiographs were collected at 2 to 3 hour time intervals for up to 10 hours after experiment initiation. The I^- tracer had reached the top boundary of all of the samples after 24 hours. After the time-series radiographs were collected, the samples were saturated with I^- tracer from both ends by removing the nylon screw caps (Figures 20 and 23) and immersing the top in tracer solution.

The progress of saturation was monitored weekly by X-ray radiography until no changes were observed in X-ray attenuation between consecutive images. During this time, the tracer solutions in the reservoirs were refreshed periodically. From the start of the tracer experiment to a fully saturated state, a period of 3 to 6 weeks – typically 5 weeks – was required to ensure saturation of the samples with I^- tracer. The experiments were carried out at room temperature, 21.7±1.5 °C.

All data were collected as digital radiographs (16-bit greyscale TIFF files) using a SkyScan 1072 desktop microCT instrument. The instrumental settings used for the OPA data acquisition were the same as those used for the OPA calibration and are listed in Table 7. Data processing for the determination of D_p was performed using the relative approach described in Cavé et al. (2009a) and Al et al. (2012), with ϕ_I calculated using the slope of the sandstone calibration curve, 1.60 (Section 3.3).

4.3.4 Non-Conservative Tracer Diffusion Properties by Radiography Using Cesium

Diffusion-reaction experiments were initiated by injecting 20 mL of the selected CsCl tracer solution (0.01, 0.001 or 0.0002 M Cs^+) slowly into the bottom of each reservoir, flushing out the OPA SPW. The outer surfaces of the samples were rinsed with distilled water and gently blotted dry. Reference radiographs were collected in triplicate immediately after tracer addition to the reservoir. The microCT instrument was operated under the same operating conditions as the I^- tracer experiments (Table 7).

Time-series radiographs were collected using the same positioning and operating conditions as used for the reference radiograph. The intervals for time-series radiograph collection varied depending on the concentration of tracer used. For the 0.01 M Cs^+ tracer solution, two to three radiographs were collected within the first eight hours, with the interval increasing to one radiograph a day for the first three days, and then every one to three days until breakthrough at the top boundary was confirmed. For the 0.001 and 0.0002 M Cs^+ tracer solutions, radiographs were collected once a day for the first two days of the experiment and then once every one to five days, depending on the tracer progress through the sample. Breakthrough occurred more rapidly for the higher concentration tracers, typically in 4 to 7 days, than for the lower concentration tracers, up to 23 days.

The tracer solutions were refreshed at the end of the first day, followed by once a day for the first three days of the experiment, and then every one to three days for the duration of the experiment. Samples were stored at room temperature (22 ± 0.6 °C) in a sealed container with an open dish of OPA SPW.

Quantification of Cs^+ concentrations in the rock samples was based on the calibrated relationship between Cs^+ concentrations and $\Delta\mu$ using the sandstone equivalent slope (Figure 15; Section 3.4). Concentration profiles were scaled by the bulk ϕ_w. It is not possible to determine a Cs^+-accessible porosity because there is no way to distinguish between Cs^+ in the porewater and Cs^+ adsorbed on mineral surfaces; the signal from the radiography includes both. The average bulk porosity value for BDR1_OC determined from weight loss by drying at 105°C for two samples is 0.164 with a range of 0.158 to 0.170 (Gimmi et al. 2014).

4.3.5 Diffusion-Reaction Simulations

The multicomponent reactive transport code, MIN3P (Mayer et al. 2002), was used to simulate diffusive transport and ion exchange in one dimension, and to calculate total Cs^+ concentration versus distance profiles. Estimates of D_{pCs} and the selectivity coefficient (log $K_{Cs+/Na+}$) were obtained using the Model-Independent Parameter Estimation code, PEST v.12.2 (Doherty 2010), by fitting simulated Cs^+ concentration profiles to experimentally determined profiles. Previously, the cation exchange capacity (CEC) was also included as a variable in the curve fitting (Cavé et al. 2010). However, the CEC and the log $K_{Cs+/Na+}$ are not independent parameters so the CEC was fixed at 12.4 meq/100g from Appelo et al. (2010) – a value that falls well within the reported range of CEC values (Table 10) and that had been determined on intact rock. When CEC is held constant, there is little correlation between D_{pCs} and the log $K_{Cs+/Na+}$, so there is good confidence in the uniqueness of fit for the two parameters.

The transport domain (Figure 25) was divided into 40 cells along the length of a sample (which ranged from 11.5 to 19.1 cm long). Each cell was initially saturated with SPW which was equilibrated to an exchange site density representing the CEC of the sample. The bulk dry density was 2.25 g/cm^3, obtained from two subsamples of BDR core (T. Gimmi pers. com. 24 August, 2011) which compares well to the 2.21 g/cm^3 reported by Koroleva et al. (2011). The value of 0.164 (Gimmi et al. 2014) was used for the bulk porosity in the diffusion-reaction simulations. This value for porosity is consistent with the 0.16 reported for Mont Terri Opalinus Clay (Mazurek et al. 2008). Both the porosity and the dry density were held constant in the simulations. The free solution diffusion coefficient for Cs^+ (D_{0Cs}) is 2.05 x10^{-9} m^2/s (Li and Gregory 1974, in Melkior et al. 2005) and was set as the upper limit for D_{pCs} values in PEST. Transport was initiated by introducing a Cs^+ tracer solution (0.0002, 0.001 or 0.01 M Cs^+), and imposing a constant boundary condition at the influx cell and a closed boundary condition at the end of the domain. Diffusion-only transport was specified for the transport calculations with ion-exchange equilibria occurring on the exchange sites in each cell.

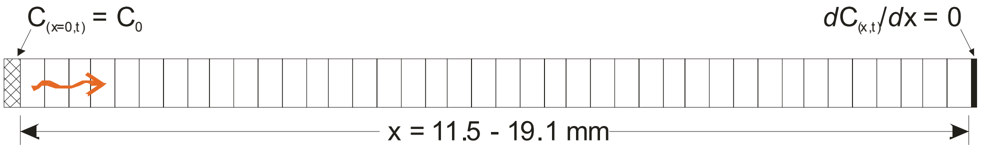

Figure 25: Schematic illustration of the MIN3P model domain. Orange arrow represents diffusion-only transport

In order to fit the model simulations to the experimental data, PEST requires each model cell to represent a matching data point. The diffusion-reaction data profiles consist of approximately 600 to 900 data points, each representing 1 pixel in the image. To reduce the number of data points to match the 40 cells in the model, polynomial curves were fit to the data points using the open-source polynomial regression data fit java applet, PolySolve Version 3.4 (Lutus 2011). The equation for the fitted curve was then used to re-calculate the equivalent Cs^+ concentration at the specific distances represented by the 40 cells in the model. This data reduction was also useful in reducing the noise from the data generated using Cs^+ tracers with low concentrations.

4.4 RESULTS AND DISCUSSION

4.4.1 Conservative Tracer Diffusion

Examples of I^- diffusion profiles are given in Figure 26, with the complete set of experimental diffusion profiles provided in Appendix B. Figure 26a presents profiles from a sample oriented normal to bedding and measured without confining pressure. Figure 26b presents profiles of the sample that was mounted in the RAD confining cell. Although these are not the same sample, the D_{pI} values derived using the RAD confining cell are a factor of about three lower, a 64% relative decrease over a subsample from the same core segment measured in the conventional diffusion cell without confining conditions (BDR1 5.57 NB13 and BDR1 5.57 NB3; Table 12). Similarly, the ϕ_I for the sample measured under confining conditions is lower than those from the samples measured without confining conditions (Figure 27). Comparison between the two 5.57 NB samples indicates a 19% decrease in ϕ_I when confining pressure was applied (Table 12). Van Loon et al. (2003a, b) did not observe changes in porosity when applying confining pressures in the range of 1 to 15 MPa to Opalinus Clay samples from Mont Terri. However, they may not have been able to distinguish any systematic changes in porosity with changes in confining pressure because of the large amount of scatter in the porosity values determined by through-diffusion and the unreliability of the through-diffusion method for porosity determination (van Loon et al. 2003a). In addition, the results reported here represent a change from unconfined conditions to something less than 1.2 MPa and, as noted in Section 2, the effect of confining pressure is non-linear and expected to be greatest near the low end of the pressure range which is not represented in data presented by Van Loon et al. (2003a,b).

Comparison with other Mont Terri Opalinus Clay D_e values, from both laboratory and in situ studies, indicates that the values from the unconfined samples measured at UNB are higher than published values (Figure 28). However, the D_e value measured under confining conditions falls very close to the published laboratory values conducted with a confining pressure of 1 MPa (van Loon et al. 2003a). The confining pressure in the RAD cell cannot be directly controlled or measured, but the confining pressure would be less than or equal to the swelling pressure of the Opalinus Clay, 1.2 MPa in the NB direction and 0.5 MPa in the PB direction (Mazurek et al. 2008). Radiographs collected before and after sample saturation with OPA SPW indicate that the sample swelled 0.67 mm in the NB direction and 0.07 mm in the PB direction within the RAD confining cell.

The I^- anisotropy ratio ($D_{e\text{-}PB:NB}$) from the UNB measurements without confining pressure is 2.2, while the published literature, measured with confining pressure, reports anisotropy ratios of 4 to 6 for Opalinus Clay at Mont Terri (Table 12). The difference in anisotropy ratios likely results from the lack of confining pressure in the UNB experiments coupled with the differential swelling pressures between the NB and PB directions (Table 10).

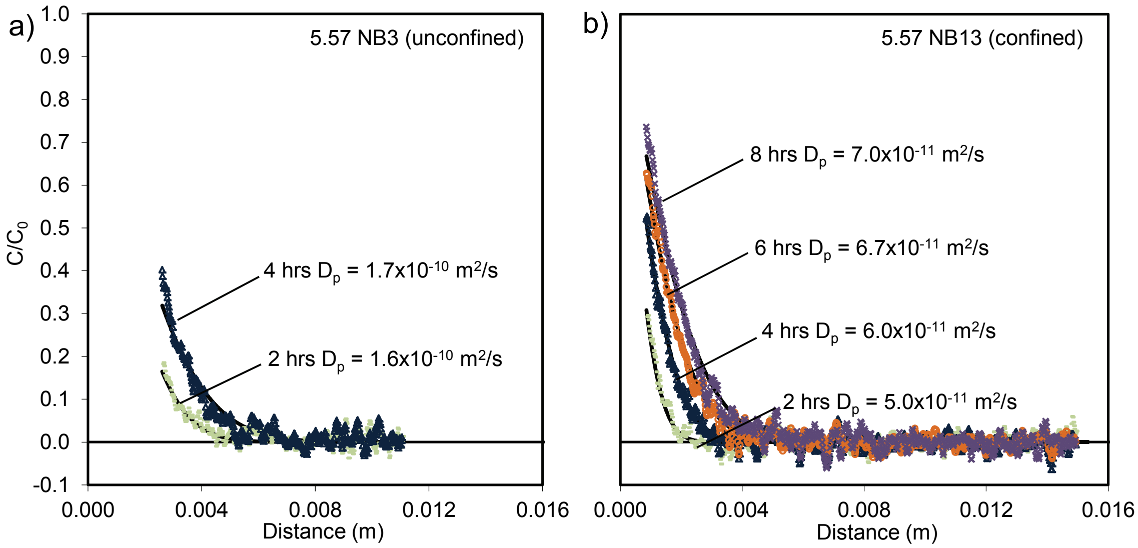

Figure 26: Examples of I^- Diffusion Curves for the Opalinus Clay BDR1 Core Samples Measured Without Confining Pressure (a) and With Confining Pressure (b)

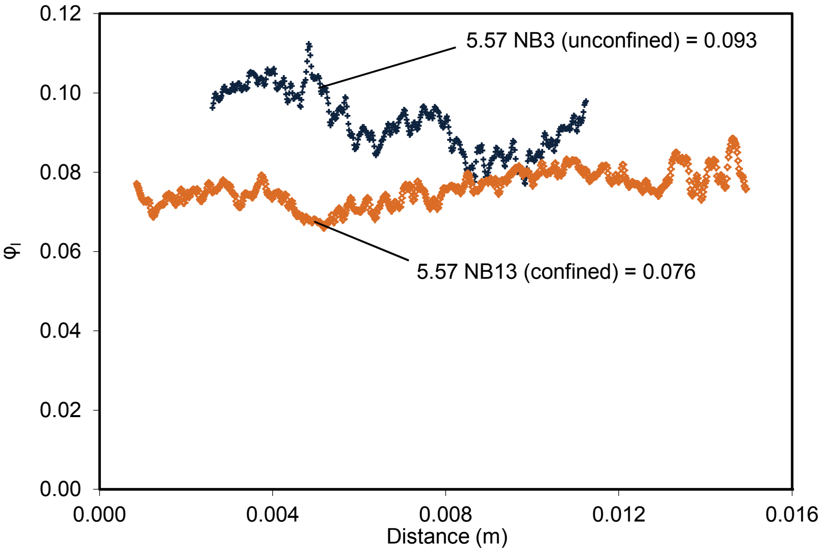

Figure 27: Examples of ϕ_I Profiles for the Opalinus Clay BDR1 Core Samples With and Without Confining Pressure

Table 12: Summary of Diffusion Measurements by Radiography for Opalinus Clay Using Iodide Tracer and Previously Reported Data

Sample	**D_p (m^2/s)**	**D_e (m^2/s)**	**ϕ_I**	**ϕ_w**	**$\phi_I : \phi_w$**
Measured without confining pressure					
BDR1 5.3 NB1	2.0×10^{-10}	2.2×10^{-11}	0.109		
BDR1 5.3 NB2	2.4×10^{-10}	2.6×10^{-11}	0.108		
BDR1 5.3 NB3	1.6×10^{-10}	1.7×10^{-11}	0.103		
5.3 NB Mean	**2.0×10^{-10}**	**2.2×10^{-11}**	**0.107**	**0.164**	**65%**
σ	4.0×10^{-11}	4.7×10^{-12}	0.003		
RSD	20%	22%	3%		
BDR1 5.3 PB1	4.3×10^{-10}	4.3×10^{-11}	0.100		
BDR1 5.3 PB2	4.4×10^{-10}	4.7×10^{-11}	0.105		
BDR1 5.3 PB3	5.1×10^{-10}	5.4×10^{-11}	0.106		
5.3 PB Mean (PB:NB = 2.2)	**4.6×10^{-10}**	**4.8×10^{-11}**	**0.104**	**0.164**	**63%**
σ	4.2×10^{-11}	7.1×10^{-12}	0.004		
RSD	9%	14%	3%		
BDR1 5.57 NB3	1.7×10^{-10}	1.5×10^{-11}	0.093	0.164	57%
Measured with confining pressure					
BDR1 5.57 NB13	6.2×10^{-11}	4.7×10^{-12}	0.076	0.164	46%
5.57 NB13 : 5.57 NB3	36%	31%	81%		
Previously reported values for the Opalinus Clay at Mont Terri with experimental conditions					
NB, anion[a]	4.6×10^{-11}	4.1×10^{-12}	0.09	0.16	56%
NB, anion, (1.0 MPa)[b]	4.8×10^{-11}	4.6×10^{-12}	0.096	0.18	53%
PB calc., anion (PB:NB = 6)[a]	2.7×10^{-10}	2.5×10^{-11}	0.09	0.16	56%
PB calc., anion (PB:NB = 4)[b]	1.9×10^{-10}	1.8×10^{-11}	0.096	0.18	53%
In situ, PB, I^-[c]	1.5×10^{-10}	1.2×10^{-11}	0.085	0.15[d]	56%
In situ, PB, I^-[c]		1.9×10^{-11}		0.17[d]	
In situ, PB, I^-[c]	4.5×10^{-10}	3.6×10^{-11}	0.08	0.15[d]	53%

All samples except BDR1 NB13 were prepared using the Dremel® tool; BDR1 NB13 was prepared with the coring drill bit.

D_p = Measured pore diffusion coefficient.

D_e = Effective diffusion coefficient calculated using the average measured iodide accessible porosity.

σ means standard deviation and RSD means relative standard deviation.

[a] Mazurek et al. 2008; [b] van Loon et al. 2003a; [c] van Loon et al. 2004 and Wersin et al. 2008. D_e values corrected for temperature differences; [d] Porosity derived from HTO diffusion tests.

Overall, the RAD confining cell was used successfully, and found to be necessary, to produce D_{eI} data for the Opalinus Clay that are consistent with published literature. The confining cell represents a new tool for measuring D_e values in swelling samples. However, modifications to increase the strength of the cell and further reduce swelling are possible.

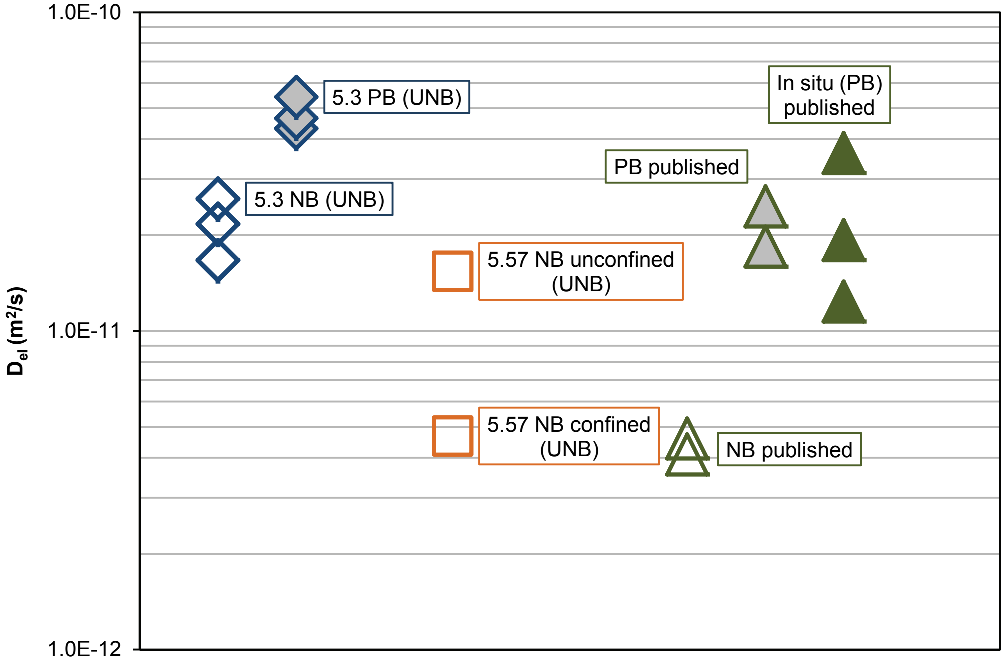

Figure 28: Comparison of D_{el} Values Measured at UNB on the BDR1 Core Samples and Published Data from Mont Terri Diffusion Studies. Data Presented for the BDR1 5.3 Samples were Measured without Confining Pressure. Data Presented for the BDR1 5.57 Samples were Measured With and Without Confining Pressure. The Published Laboratory Values were Measured under a Confining Pressure of 1 MPa (Mazurek et al. 2008; van Loon et al. 2003a; van Loon et al. 2004; Wersin et al. 2008)

4.4.2 Non-Conservative Tracer Diffusion

The results of the PEST-MIN3P simulations are summarized in Table 13. Overall, the simulations were able to generate very good fits to the Opalinus Clay experimental data. Examples of fitted Cs^+ diffusion-reaction profiles for each of the Cs^+ tracer concentrations are provided in Figure 29. Examples of the MIN3P-PEST input files are included in Appendix C, and the complete set of fitted diffusion-reaction profiles are provided in Appendix D. The diffusion-reaction profiles generated with the 0.0002 M Cs^+ tracer contain a great deal of noise relative to the signal. The amount of noise decreases as the Cs^+ concentration in the tracer increases.

For each sample, PEST was used to fit a complete dataset of multiple time-series profiles and provide parameter estimates that reflect the average for the sample. As a result, there are slight variations, due, for example, to sample heterogeneity, where the simulated profiles do not directly match the experimental data points for all time series (Figure 29). For selected samples, PEST was also used to fit each time series individually and it was found that the fit for the individual time series could be improved (Figure 30). However, the mean of the estimated parameters is equivalent for both approaches. For example, fitting the combined set of time-series profiles for sample 5.57 PB8 (Figure 29c and Table 13) provides a value of 1.4 for log $K_{Cs+/Na+}$ and 1.3 x 10^{-9} m^2/s for D_{pCs} while the corresponding mean for the two parameters based on individual time series fits is 1.4 and 1.2 x 10^{-9} m^2/s, respectively (Figure 30).

Table 13: Values for D_{pCs} and log $K_{Cs+/Na+}$ Determined from Radiography and Reactive-Transport Simulations for the Opalinus Clay BDR1 Core Samples

Sample ID	**log $K_{Cs+/Na+}$**	**D_{pCs} (m^2/s)**	**Sample ID**	**log $K_{Cs+/Na+}$**	**D_{pCs} (m^2/s)**
		Cs$^+$ Tracer Concentration 0.0002 M			
5.3 NB3	2.0	1.3 x10^{-9}	5.3 PB3	2.0	1.8 x10^{-9}
5.3 NB4	2.1	5.6 x10^{-10}	5.3 PB4	1.8	1.6 x10^{-9}
5.57 NB7	2.2	8.1 x10^{-10}	5.57 PB7	1.9	2.0 x10^{-9}
Mean NB	**2.1**	**8.9** x10^{-10}	**Mean PB**	**1.9**	**1.8 x10^{-9}**
σ NB	0.07	4.0 x10^{-10}	σ PB	0.08	2.2 x10^{-10}
RSD (%)	3	44	RSD (%)	5	12
		Cs$^+$ Tracer Concentration 0.001 M			
5.3 NB2	1.7	9.5 x10^{-10}	5.3 PB2	1.7	1.9 x10^{-9}
5.3 NB5	1.8	6.4 x10^{-10}	5.3 PB5	- Sample fractured -	
5.57 NB6	2.0	8.6 x10^{-10}	5.57 PB9	1.7	2.0 x10^{-9}
Mean NB	**1.8**	**8.2 x10^{-10}**	**Mean PB**	**1.7**	**2.0 x10^{-9}**
σ NB	0.15	1.6 x10^{-10}	σ PB	na	na
RSD (%)	8	20	RSD (%)	na	na
		Cs$^+$ Tracer Concentration 0.01 M			
5.3 NB1	1.5	6.9 x10^{-10}	5.3 PB1	1.3	1.3 x10^{-9}
5.57 NB8	1.6	1.0 x10^{-9}	5.57 PB8	1.4	1.3 x10^{-9}
5.57 NB11	1.5	4.8 x10^{-10}	5.57 PB11	1.4	1.7 x10^{-9}
Mean NB	**1.5**	**7.2 x10^{-10}**	**Mean PB**	**1.4**	**1.4 x10^{-9}**
σ NB	0.05	2.7 x10^{-10}	σ PB	0.04	2.2 x10^{-10}
RSD (%)	3	37	RSD (%)	3	16
		Published values for Opalinus Clay at Mont Terri			
Orientation	**log $K_{Cs+/Na+}$ planar sites**	**D_{pCs} (m^2/s)**	Orientation	**log $K_{Cs+/Na+}$ planar sites**	**D_{pCs} (m^2/s)**
NB	1.6[a,b]	1.1 x10^{-9}[b]	PB	na	1.3 x10^{-9}[c]
			PB	na	1.7 x10^{-9}[d]
			PB	2.0[e]	1.3 x10^{-9}[e]

All 5.3 series samples were prepared using the Dremel® tool; all 5.57 series samples were prepared using the coring drill bit.

CEC = 12.4 meq/100 g; bulk ϕ_w = 0.164; "na" means not applicable.

[a] Bradbury and Baeyens 2000; [b] Jakob et al. 2009; [c] Wersin et al. 2008; [d] van Loon et al. 2004; [e] Appelo et al. 2010.

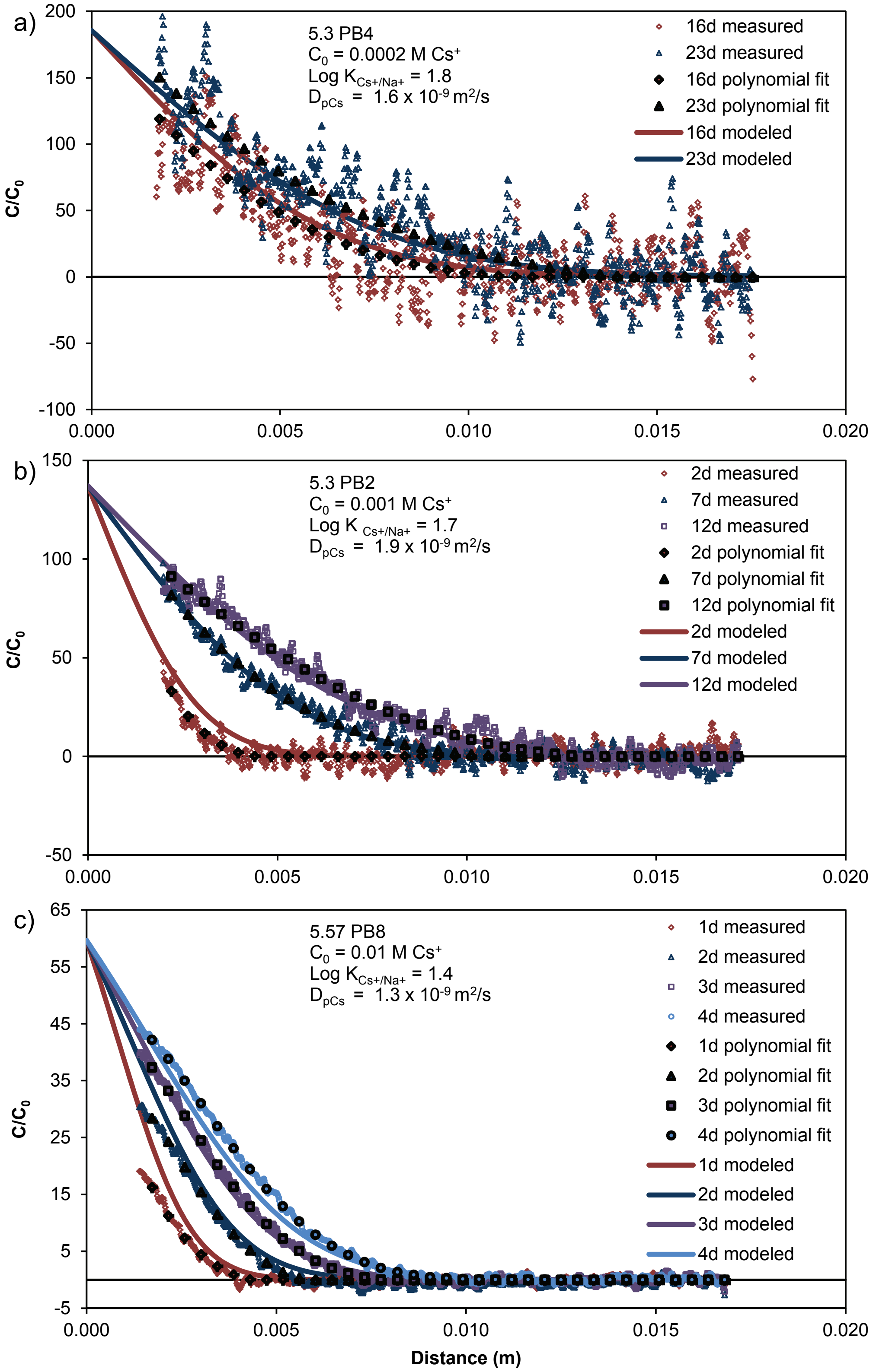

Figure 29: Examples of Measured and Fitted Cs^+ Diffusion Profiles. The Label, Polynomial Fit, Refers to the Fitting of the Experimental Data that Is Required Prior to the PEST Analysis

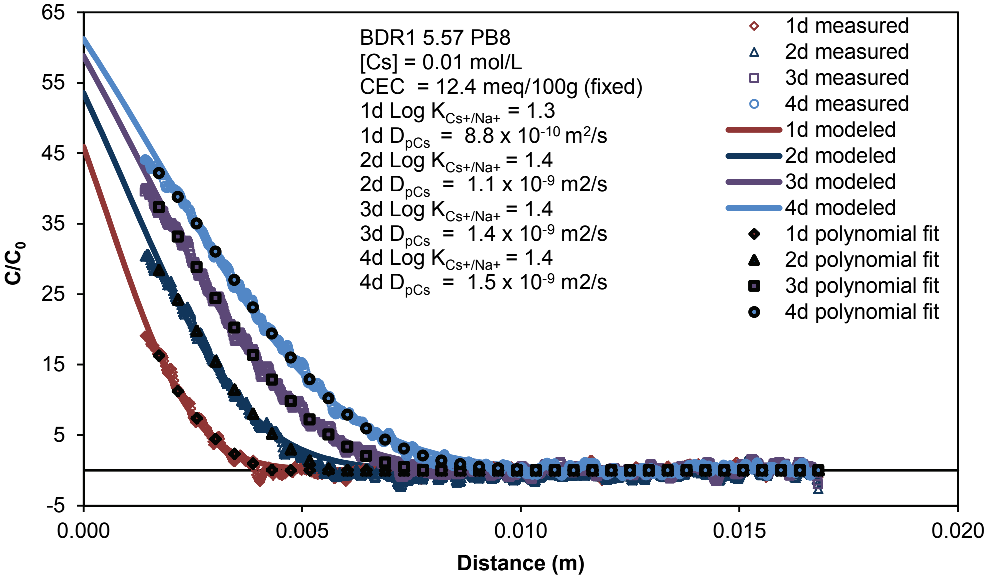

Figure 30: Fitted Cs^+ Diffusion Profiles Based on Matching Time-Series Profiles Individually Rather Than as a Combined Set. The Label, Polynomial Fit, Refers to the Fitting of the Experimental Data that Is Required Prior to the PEST Analysis

4.4.2.1 The Cesium Pore Diffusion Coefficient

Figure 31 presents the results of D_{pCs} estimations in the context of the concentration of the tracer used, the sample orientation, and published values for Opalinus Clay at Mont Terri. The measured D_{pCs} values are not significantly different at the 95% confidence level between the three tracer concentrations. The D_{pCs} values measured in this work are generally consistent with published values (Figure 31) and are approximately an order of magnitude greater than published D_{pHTO} values for the Opalinus Clay (Jacob et al. 2009). In addressing a similar observation, Jakob et al. (2009) attribute the elevated D_{pCs} values to preferential diffusion of Cs^+ through the clay interlayers and externally-bound, double-layer water. Some of the values for the PB-orientated samples in this work (Figure 31) approach the Cs^+ free solution diffusion coefficient (D_{0Cs}) of 2.05 x 10^{-9} m^2/s (Li and Gregory 1974). Additionally, as with the I^- tracer, it is apparent that the rock is anisotropic with respect to diffusion properties. The D_{pCs} measured parallel to bedding is significantly greater at the 99% confidence level than the D_{pCs} measured normal to bedding and the anisotropy ratio (PB:NB) for the Cs^+ data is 2.1, similar to the I^- PB:NB ratio of 2.2 (Section 4.4.1), both measured without confining pressure. The published literature has not evaluated anisotropy in D_{pCs} in Opalinus Clay data to date; the published PB and NB data presented in Figure 31 were derived from different experimental conditions and data processing methods and therefore are not directly comparable. The samples for the Cs^+ experiments were mounted in the conventional RAD cell (unconfined). Therefore, based on the findings from the I^- tracer (Section 4.4.1), the D_{pCs} values and anisotropy ratio reported here may be higher than if the measurements were conducted under confined conditions.

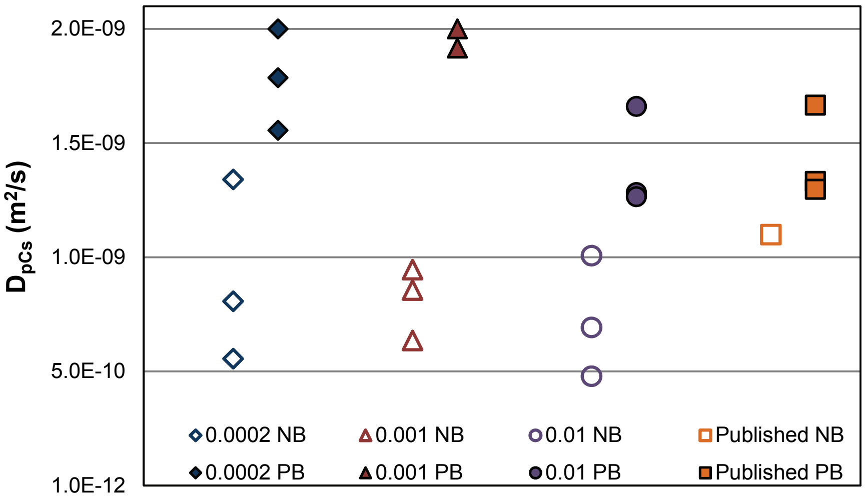

Figure 31: Comparison of D_{pCs} Values Measured at UNB in the NB and PB Orientations with Published Data from Mont Terri Diffusion Studies. Data Sources: van Loon et al. (2004); Wersin et al. (2008); Jakob et al. (2009); Appelo et al. (2010). Published PB and NB Values Are Not from Matched Samples

4.4.2.2 The Selectivity Coefficient for Cesium

Figure 32 presents the results of log $K_{Cs+/Na+}$ estimations from the UNB simulations in the context of the tracer concentration and the sample orientation. Results display a range in log $K_{Cs+/Na+}$ of 1.4 to 2.1 and a decrease in log $K_{Cs+/Na+}$ as Cs^+ tracer concentration increases (Table 13). Direct comparison with published studies of Cs^+ behaviour in Opalinus Clay from Mont Terri is not possible because the published literature uses a three-site model for Cs^+ adsorption on illite based on Bradbury and Baeyens (2000). In contrast, the reactive transport simulations carried out for this work use a single-site model that does not restrict Cs^+ adsorption to the surface of illite. Generally, it is thought that the frayed edge sites (FES) of illite dominate Cs^+ sorption at Cs^+ concentrations $<10^{-8}$ M, the type II sites of illite become the dominant sorption site at Cs^+ concentrations from 10^{-8} to 10^{-5} M, and planar sites dominate sorption at Cs^+ concentrations $>10^{-3}$ M (Jakob et al. 2009). With the 0.01 M and 0.001 M tracer concentrations used for the UNB measurements, the planar sites are expected to dominate the overall selectivity for Cs^+ in those experiments. With the 0.0002 M tracer, Cs^+ sorption on both planar and type II sites will likely have an effect on the value of log $K_{Cs+/Na+}$, which is consistent with the trend in increasing log $K_{Cs+/Na+}$ with decreasing Cs^+ tracer concentration (Figure 32). The log $K_{Cs+/Na+}$ values obtained with the 0.0002 M tracer are significantly greater at a 95% confidence level than the values obtained with the 0.01 M tracer. The statistical significance of the difference in log $K_{Cs+/Na+}$ values between the 0.001 M and 0.01 M tracers cannot be established because of the small number of test samples. There is a tendency toward higher measured log $K_{Cs+/Na+}$ in the NB orientation compared to the PB orientation, which is significant at the 95% confidence level for the 0.0002 M and 0.01 M tracer concentrations. If this is a significant difference, we have no explanation for this observation at this time.

A value of 1.6 for the log $K_{Cs+/Na+}$ of planar sites on illite is commonly used in the literature (Bradbury and Baeyens 2000; van Loon et al. 2004; Jakob et al. 2009). Jakob et al. (2009)

made the assumption that the log $K_{Cs+/Na+}$ value of 1.6 represents a cumulative value accounting for the ion exchange sites on all minerals in the sample, not just the planar sites on illite. Appelo et al. (2010) optimized the log $K_{Cs+/Na+}$ values to experimental data and determined a value of 2.04 for planar sites, while Appelo and Postma (2005) cited a single-site log $K_{Cs+/Na+}$ of 1.1. The UNB measured results are consistent with this range of published values (Table 13).

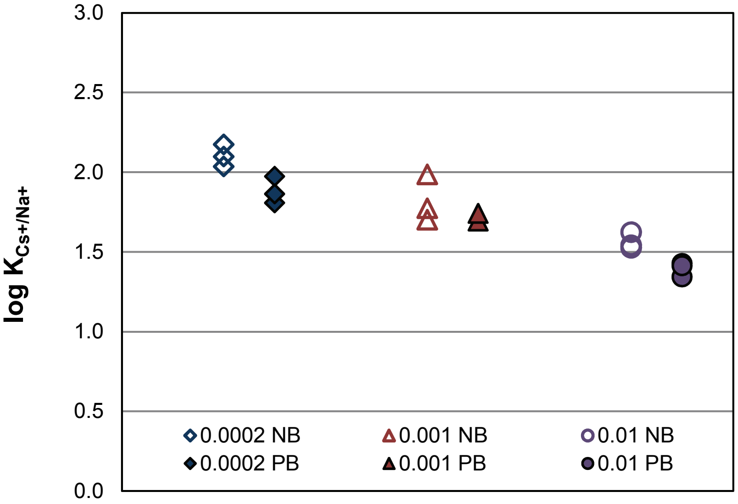

Figure 32: Comparison of log $K_{Cs+/Na+}$ Values Determine at UNB on the BDR1 Core Samples for the 0.0002, 0.001 and 0.01 M Tracer Concentrations in Both the NB and PB Orientations

4.4.2.3 The Effect of Sample Heterogeneity

All of the transport simulations carried out to date, including the analytical fit to diffusion profiles for I^- and the diffusion-reaction simulations for Cs^+, have been performed with the assumption of homogeneous material properties. However, from the ϕ_I profiles, in particular for samples oriented normal to bedding, porosity profiles display evidence of heterogeneity (Figure 27). Sample heterogeneity is also apparent in the time-series profiles of two samples used in the Cs^+ experiment (5.57 NB8 and 5.57 NB11). For example, the presence of heterogeneity in sample 5.57 NB11 produces noise in the time-series profiles at approximately 0.006 m into the sample and in a larger zone that starts at 0.008 m and extends to 0.01 m along the sample length (Figure 33). This type of noise was not observed in the PB samples with the same 0.01 M Cs^+ tracer (e.g., Figure 29c). The modelling performed based on the assumption of sample homogeneity (Figure 33) could not reproduce the finer nuances of the time-series profiles and lead to over prediction of transport in the early time series and under prediction in the late time series.

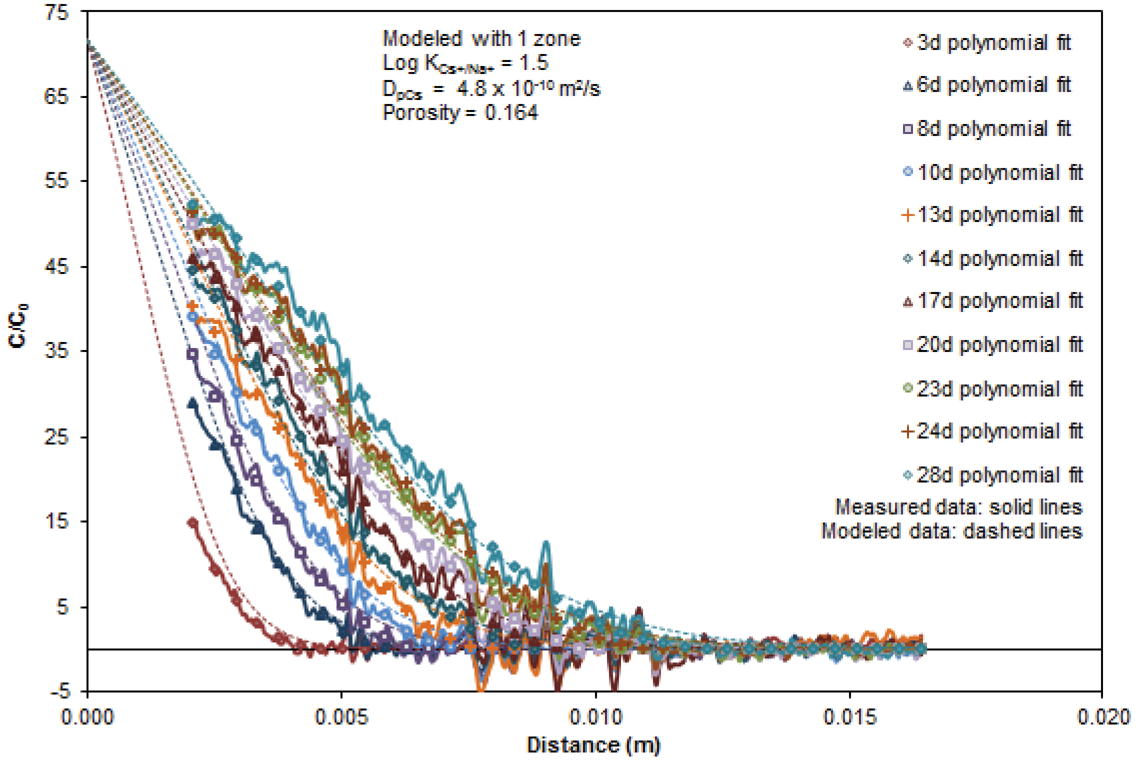

Figure 33: Experimental Time-Series Profiles for Sample 5.57 NB11 and the Best-Fit Diffusion-Reaction Simulations Assuming Homogenous Sample Properties. C_0 = 0.01 M Cs^+; CEC = 12.4 meq/100g

After the experiment had been completed, petrographic thin sections were prepared and investigated using SEM. From the SEM analysis, the decreased diffusivity is thought to relate to thin (less than 1 mm) pyrite-rich, calcite-cemented layers with relatively low porosity (e.g., approximately 5%) that occur dispersed throughout the samples in a general parallel-to-bedding orientation (Figure 34).

To further investigate the effects of sample heterogeneity, an allowance for heterogeneity in both porosity and D_{pCs} was introduced into the model domain for sample 5.57 NB11. The model transport domain was divided into a total of 879 cells to accommodate the full raw data set (rather than the smoothed profile from the polynomial fit) and five zones, based on features observed in the time series profiles, were added. PEST was then used to fit a porosity and D_{pCs} for each of the five zones for four of the time-series profiles. The CEC and the log $K_{Cs+/Na+}$ were held constant in the sample at 12.4 meq/L and 1.5, respectively, however, considering the mineralogy in the low permeability zones, this may not be realistic. Specifically, there is a low illite content in the low permeability layers (Figure 34) so it is likely that the CEC and the log $K_{Cs+/Na+}$ would decrease accordingly. Therefore, the following assessment of the variability in porosity and D_{pCs} values does not consider all important variables.

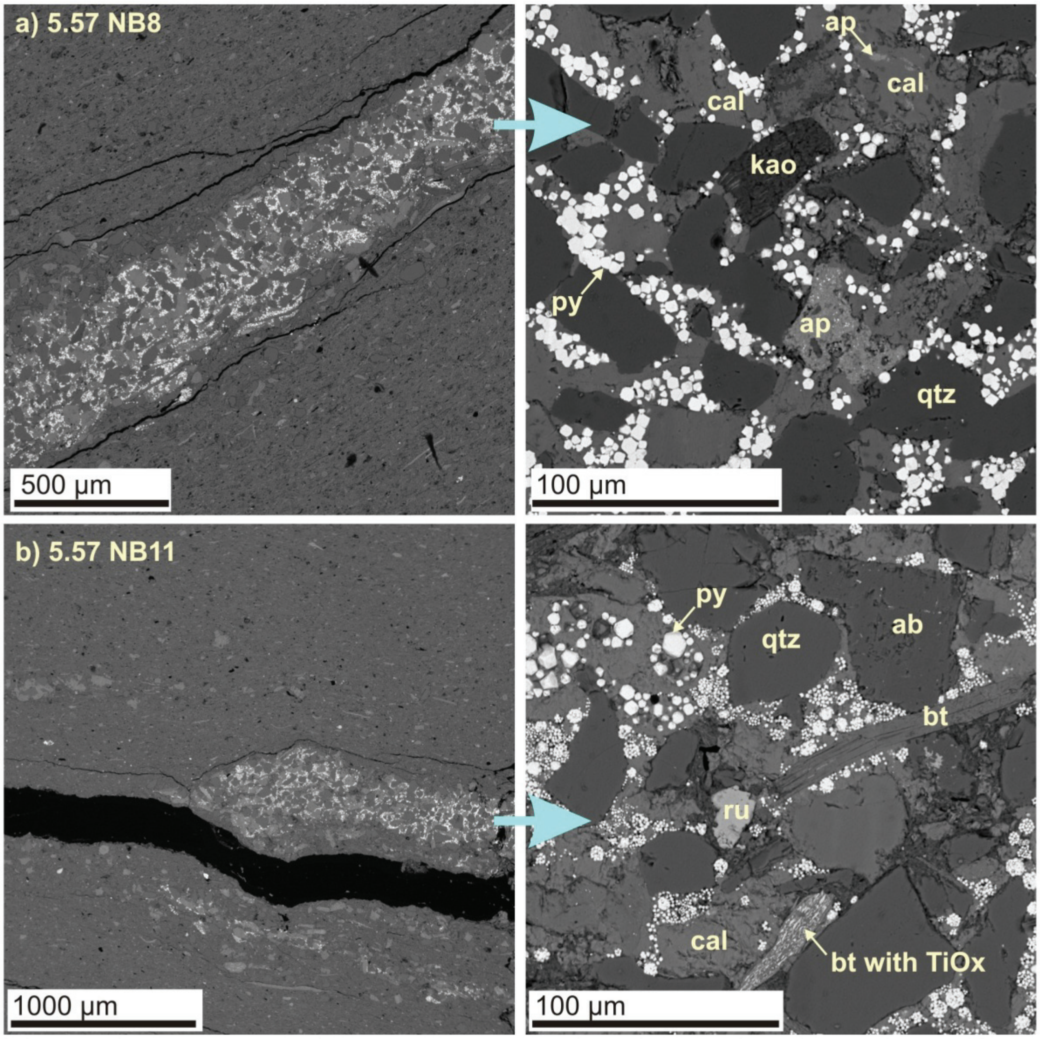

Figure 34: BSE SEM Images from Opalinus Clay BDR1 Samples (a) 5.57 NB8 and (b) 5.57 NB11. Qtz = Quartz, kao = Kaolinite (or Similar Clay), cal = Calcite, ab = Albite, bt = Biotite, ru = Rutile, py = Pyrite, ap = Apatite, TiOx = Ti Oxide. The Images on the Right are Higher Magnification Images from the Areas Shown on the Left

The fitting process was successful in fitting the four time series and in reproducing the features of the curves (Figure 35). The fitted porosities ranged from 0.05 to 0.21 and the fitted D_{pCs} ranged from 1.0×10^{-13} to 4.4×10^{-10} m^2/s. A narrow band of siltstone with low porosity was observed in the last 0.005 m of the sample (Figure 34b) but most of this interval consists of the clay matrix. Therefore, the low porosity (0.05) assigned to this 0.005 m interval in the model (Figure 35) is likely not representative of the sample. These results are sufficient to demonstrate the effect of heterogeneity at a small scale but the work has not been sufficiently detailed to allow for a thorough discussion of spatial variability in D_{pCs}.

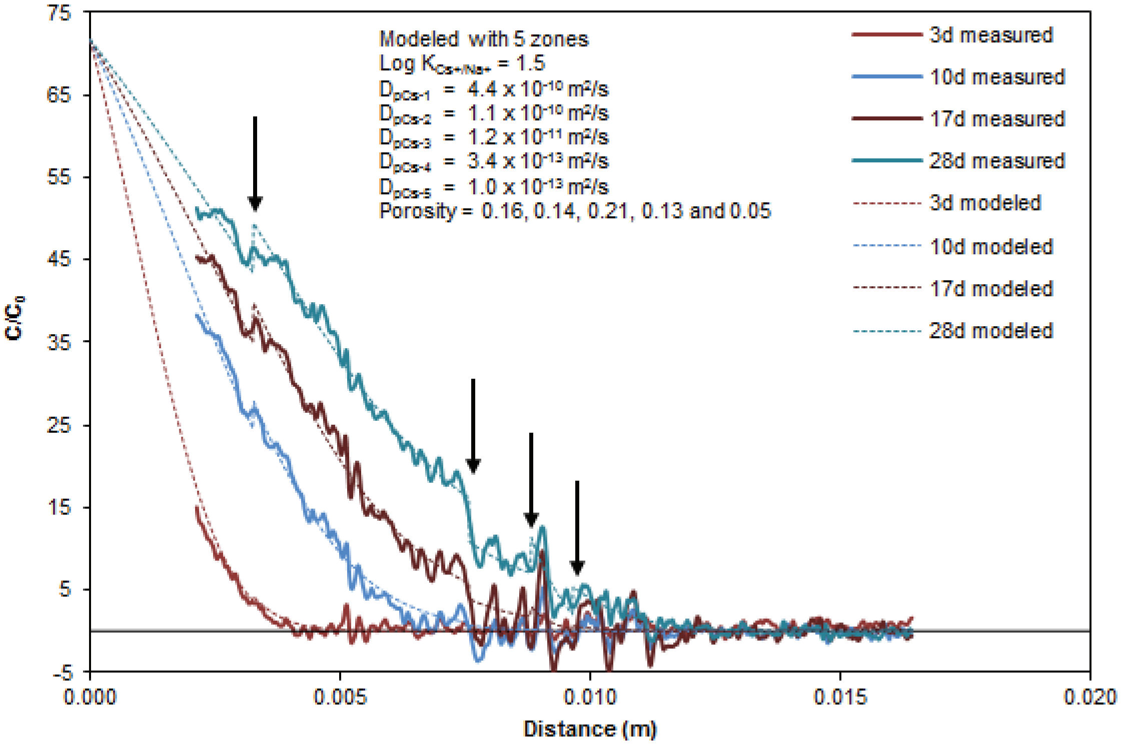

Figure 35: Selected Experimental Time-Series Profiles for Sample 5.57 NB11 and the Best-Fit Diffusion-Reaction Simulations Using 5 Zones of Variable Porosity and D_{pCs}. Arrows Mark the Zone Boundaries. C_0 = 0.01 M Cs^+; CEC = 12.4 meq/100g

4.5 SUMMARY

Diffusion measurements were made by radiography on samples of Opalinus Clay from the Mont Terri URL in Switzerland using a conservative (I^-) and a non-conservative (Cs^+) tracer. The Opalinus Clay contains swelling clays and the standard RAD diffusion cell developed in previous studies was not designed to contain swelling samples. The samples expanded in the standard diffusion cells, resulting in high D_{eI} and ϕ_I values and low anisotropy ratios (2.2) compared to published anisotropy ratios (4-6). The radiography cell was re-designed to hold swelling or disaggregated samples in confined conditions. However, the rigidity of the new cell (RAD confining cell) was limited by the need to use plastic materials with low X-ray absorption. Consequently, not all sample swelling was eliminated and there was no control or monitoring of the confining pressure. However, one measurement was conducted with the RAD confining cell and the result obtained, D_{eI} = 4.7 x10^{-12} m^2/s, is consistent with published values. The new RAD confining cell adds to the methods available for radiography measurements.

For the non-conservative tracer, Cs^+, the multicomponent reactive transport code MIN3P was used to perform diffusion-reaction transport simulations and to calculate total Cs^+ concentration versus distance profiles. Estimates of D_{pCs} and log $K_{Cs+/Na+}$ were obtained using the Model-Independent Parameter Estimation code, PEST, which fit simulated Cs^+ concentration profiles to experimental profiles. The diffusion-reaction experiments were conducted using standard

RAD diffusion cells so the swelling of the samples was not controlled. The results from the experiments carried out with unconfined samples suggest that the effect of sample anisotropy on Cs^+ diffusion, with a PB:NB ratio of 2.1, is similar to that observed with the I^- tracer.

The values for log $K_{Cs+/Na+}$ and CEC are strongly correlated, so the CEC was set to 12.4 meq/100g - a value obtained from recent published literature (Appelo et al. 2010). The fitted range of values for log $K_{Cs+/Na+}$ was 1.4 to 2.1, which is consistent with published values. A decrease in log $K_{Cs+/Na+}$ was observed as the Cs^+ concentration in the tracer increased, and this is consistent with expectations based on literature reports describing the characteristics of multiple binding sites on illite.

For some samples oriented normal to bedding, sample heterogeneities are reflected in the data. Improvements were achieved with the model fit by allowing for variable porosity and D_{pCs} in the diffusion-reaction simulations.

5. INVESTIGATING EFFECTS OF PARTIAL SATURATION ON DGR ROCKS

Results of geoscientific studies suggest that the brine saturations may be less than 100% at some depths in the Ordovician shales and limestones (Raven et al. 2010). It is possible that partial brine saturation could limit aqueous-phase diffusion. Our objectives are: 1) to generate gas/brine partial saturation in the rock pores; 2) to measure the level of the partial saturation generated; and 3) to develop a method to measure D_e values for partially saturated rock samples.

Soil scientists have been working to control and monitor soil water content and to investigate its effects on aqueous-phase diffusion for many years (Barraclough and Tinker 1981; Lim et al. 1998; Plummer et al. 2004; Pace et al. 2007; Aldaba et al. 2010). However, the methods used for soils are not applicable for low-permeability rocks (i.e., solid aggregated material) because of the large differences in physical properties such as consolidation, grain size, porosity and pore-size distribution.

Working with the low permeability Callovo-Oxfordian claystone, Savoye et al. (2010) used the through-diffusion method to measure aqueous diffusion coefficients over a range of water saturations. They controlled the degree of saturation in the sample by creating an osmotic gradient, drawing porewater with relatively low ionic strength out of the rock and into a higher ionic strength solution of polyethylene glycol. This method is not suitable for the rocks from the Michigan Basin because of the naturally high porewater ionic strength. Conca and Wright (1992) used steady-state centrifugation to control the degree of saturation and measure unsaturated hydraulic conductivity in soils, gravel, bentonite, volcanic tuff and mudstone. They also measured diffusion coefficients using electrical conductivity in a specialized centrifuge assembly. It is unlikely that such an approach could work with Michigan Basin samples because the high salinity brine would interfere with measurements of electrical conductivity. Delage et al. (1998) describe a method for controlling the degree of saturation in clay samples by controlling relative humidity using saturated saline solutions and/or concentrated sulphuric acid. This method is different from the osmosis method because it involves vapour phase exchange rather than liquid-phase exchange, and consequently has been found to be a slower process. Even if the sulphuric acid was sufficient to desaturate samples, and the desired degree of saturation could be maintained for the duration of a diffusion experiment, the salts left in the pores after evaporation of the porewater would cause artefacts in subsequent diffusion measurements.

After considering possible approaches, we believe that it may be possible to control the brine/gas saturation by dissolving an inert gas, such as nitrogen (N_2) or argon (Ar), to saturation in the porewater of a sample at a high pressure, and then reduce the pressure such that gas bubbles nucleate and grow within the sample. The solubility-pressure relationships for Ar or N_2 suggest that either of these gases could be suitable for controlled partial saturation experiments with Michigan Basin samples. However, there are more published data available for N_2 solubility versus pressure and salinity (Mao and Duan 2006), and N_2 is therefore considered the most appropriate gas for the proposed experimentation.

Various methods that may be useful in measuring the degree of partial saturation of rock samples have been considered. Gas in sandstone has been found to affect the behaviour of seismic and sonic waves, with enhanced wave amplitudes being reported on samples saturated with a mixture of gas and brine (Yin et al. 1992). Unfortunately the amplitude effect appears to be non-linear with the gas/brine ratio; therefore, these waves cannot be used to quantify partial saturation (Domenico 1976; Frisillo and Stewart 1980). When investigating ultrasonic absorption in partially saturated sandstone, Frisillo and Stewart (1980) used an X-ray absorption technique to verify the gas/brine saturation, in which 150,000 ppm NaI was added to the brine as a strong X-ray absorber. In this study, we will use an X-ray radiography method (which is based on X-ray absorption), similar to the technique described by Cavé et al. (2009a), to determine the gas/brine saturation.

5.1 PARTIAL SATURATION

The solubility of a gas in aqueous solution at a given temperature is proportional to its partial pressure. This is known as Henry's law:

$$S_i = K_H \cdot P_i \qquad [2]$$

where S_i is the solubility of gas i (mol/L) in an aqueous solution, K_H is the Henry's law constant ($mol \cdot L^{-1} \cdot atm^{-1}$ or M/atm) for gas i in the solution, and P_i is the partial pressure of gas i (atm). The constant K_H is dependent on the gas, the temperature and the solution composition. The following set of conditions was selected for the initial brine/gas partial saturation experiment using a sample of Queenston Formation shale: i = N_2, T = 22 ^{0}C, and brine solution = 5.3 mol/L NaCl. The solubilities of N_2 at these conditions as a function of partial pressure P_{N2} (Figure 36) were calculated using the empirical model reported by Mao and Duan (2006). The solubilities of N_2 in pure water and in 3.7 mol/L NaCl brine are also included for comparison.

Data in Figure 36 indicate that N_2 solubility in 5.3 mol/L NaCl brine obeys Henry's law up to a partial pressure of 100 atm (filled symbols), after which (open symbols) slight deviation occurs due to non-ideal behaviour. The K_H value determined for 5.3 mol/L NaCl brine is 0.000156 $mol \cdot L^{-1} \cdot atm^{-1}$ (or M/atm).

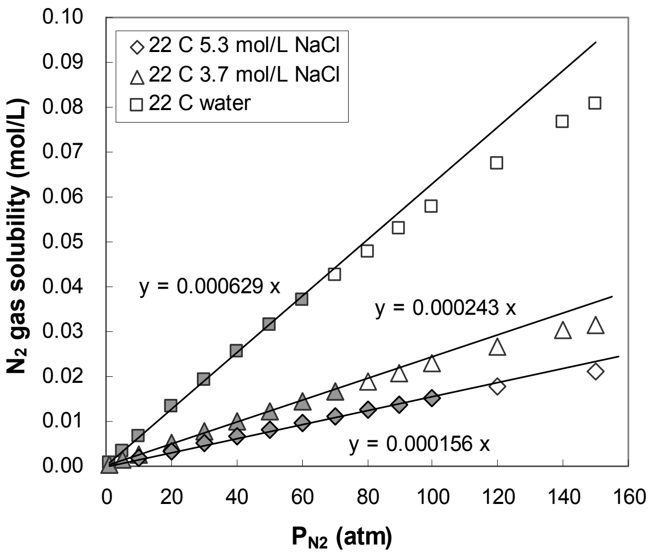

Figure 36: Henry's Law Plots for N_2 Gas at 22 °C in 5.3 mol/L NaCl Brine, in 3.7 mol/L NaCl Brine, and in Pure Water Calculated using the Empirical Model Reported by Mao and Duan (2006). The Slope of the Relationships Corresponds to the Henry's Law Constant, K_H

When the partial pressure of N_2 is reduced from P_1 to P_2, the solubility of N_2 in brine solution decreases correspondingly from S_1 to S_2. As a result, gas bubbles will form in the brine solution. For the brine solution in the pore spaces of a rock sample, a decrease of the partial pressure will result in the formation of gas bubbles in the pore spaces, causing partial brine saturation in the rock. The moles of N_2 bubbles, n, can be calculated according to Equation 3:

$$n_{bubble} = K_H V_p (P_1 - P_2) \qquad [3]$$

where V_p is the volume of the rock pores (L) initially occupied by brine, and $P_2 < P_1 < 100$ atm. The volume of the gas bubbles (V_{bubble}) formed at P_2 can be calculated using the ideal gas law:

$$V_{bubble} = K_H V_p (P_1 - P_2) RT / P_2 \qquad [4]$$

The relative error in the gas volume calculated using the ideal gas law versus van der Waal's equation for non-ideal gases (Equation 5) is negligible (0.07%) and the ideal gas law is considered to be effective for N_2 at the experimental conditions.

$$(\mathrm{P} + \frac{n^2 \mathrm{a}}{\mathrm{V}^2})(V - nb) = nRT \qquad [5]$$

where a and b are the van der Waals constants for N_2 gas (1.39 $L^2 \cdot atm \cdot mol^{-2}$ and 0.0391$L \cdot mol^{-1}$, respectively).

It is assumed that upon equilibration bubbles will form and remain in the rock pores. This assumption will be tested with X-ray radiography. The volume change associated with bubble formation must be accommodated by expulsion of brine from the pores. The calculated bubble volume will be an approximation because the propagation of the pressure decrease into the sample which controls bubble formation, and the expulsion of brine, are governed by the rock permeability. During this pressure equilibration stage there will be diffusive loss of N_2 from the sample, so Equations 3 and 4 are likely to overestimate the volume of gas bubbles formed. Subject to this limitation, the relative pore volume occupied by gas (% gas saturation) can be expressed as the ratio of V_{bubble} to V_p (Equation 6):

$$\%\text{ gas saturation} = [K_H(P_1-P_2)RT/P_2] \times 100\% \qquad [6]$$

The experiment was designed so that P_2 is equal to 1 atm of pure N_2. The P_1 values, as a function of % gas saturation, are calculated using Equation 5 and presented in Table 14. The P_1 values above 100 atm in Table 14 were estimated assuming that Henry's law still applies. More accurate values might be calculated using a quadratic fit rather than a linear fit to the data.

Table 14: Relationship between % Gas Saturation and Initial N_2 Partial Pressure (P_1)

% gas sat.	P_1 (atm)[a]	% gas sat.	P_1 (atm)
2	6.2	45	118.6
5	14.1	50	131.7
10	27.1	55	144.7
20	53.3	60	157.8
25	66.3	70	183.9
30	79.4	80	210.1
35	92.5	90	236.2
40	105.5		

[a] Data were calculated using Equation 5 under the following conditions: T = 22 ^{0}C, 5.3 mol/L NaCl brine with a K_H constant of 0.000156 mol•L^{-1}•atm^{-1}, P_2 = 1 atm N_2.

5.2 EXPERIMENTAL PROCEDURES

A sample of Queenston Formation shale (DGR3-472, ϕ_w = 7.5%) was used for this experiment. A special cell was designed and constructed (Figure 37). The experimental procedures are described stepwise.

Step 1. Cell assembly and reference radiography

The circumference of the cylindrical rock sample (nominal 10.7 mm diameter, 17 mm height) was brushed with a thin layer of silicone and enclosed in N_2-impermeable Teflon® heat shrink tubing (PTFE, 12.7 mm diameter before shrinking, Cole-Parmer). The cell design differs from our RAD cell used for diffusion experiments (section 4.3.2) with respect to: 1) this cell has two caps that slide up and down to maintain 1 atm pressure; 2) it opens from both ends; and 3) the large ceramic screws are intended for use as an internal standard.

The sample was immersed in S-SPW for more than 5 weeks - a length of time that was deemed suitable based on experience from previous TD and RAD experiments. Delrin® caps were placed at both ends of the rock sample, and the sample was sealed in the cell with ceramic screws (Figure 37). Three reference radiographs were recorded to obtain a measure of the reference X-ray attenuation coefficient (μ_{ref}).

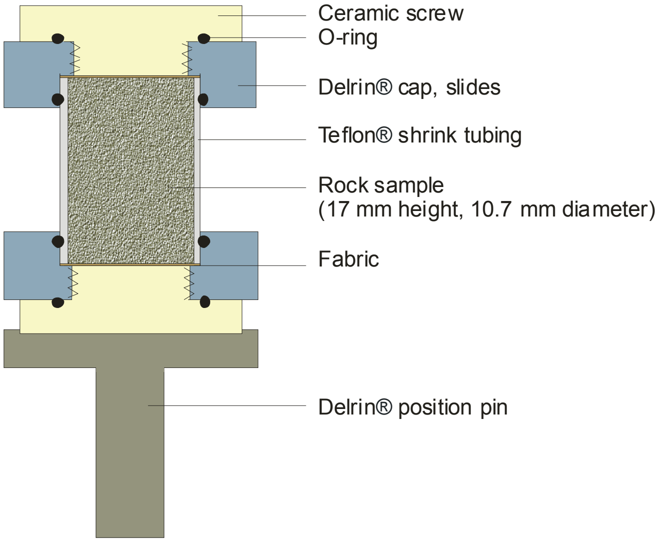

Figure 37: Diagram of the Radiography Cell for the Gas/Brine Partial Saturation Experiment

Step 2. Tracer saturation (0% gas saturation)

The ceramic screws were removed and the sample was immersed in an I^- tracer solution (prepared by replacing 1.0 M NaCl with 1.0 M NaI in the S-SPW matrix). The progress of tracer diffusion was monitored by recording radiographs. When no further change in X-ray attenuation was detected in consecutive radiographs, a final radiograph was recorded to obtain a measure of the X-ray attenuation coefficient for the tracer-saturated sample (μ_{tracer}). The difference between the X-ray attenuation for the tracer-saturated sample and the reference ($\Delta\mu_{tracer}$) is:

$$\Delta\mu_{tracer} = \mu_{ref} - \mu_{tracer} \qquad [5]$$

Step 3. Partial (20%) gas saturation

The ceramic screw caps were removed from the ends and the cell was immersed in 1.0 M I^- tracer solution in a beaker. The beaker was placed in a pressure cell and N_2 gas was introduced to the head space at 800 psi (54 atm). At $P_1 = 54$ atm, the corresponding partial gas saturation is 20.3% (Table 14 or Equation 5). The system was maintained in this condition for 3 weeks to allow dissolved $N_{2(aq)}$ to diffuse into the rock sample. After 3 weeks, the N_2 pressure was released and the radiography cell was re-assembled in approximately 10 minutes.

The system was allowed to equilibrate at 1 atm N_2 pressure, during which time radiographs were recorded periodically to monitor the progress. When no further change in X-ray attenuation was detected in consecutive radiographs, a final radiograph was collected to obtain a measure of the X-ray attenuation coefficient for the partially saturated sample (μ_{PS}). The degree of partial saturation is reflected in the difference in X-ray attenuation between the partially saturated sample and the tracer-saturated sample ($\Delta\mu_{gas}$):

$$\Delta\mu_{gas} = \mu_{tracer} - \mu_{PS} \qquad [6]$$

Step 4. Confirmation of Partial Saturation

This experiment was designed to test the concept of using controlled changes in N_2 solubility at different pressures to create partial gas saturation in porous media. X-ray radiography is used to confirm the presence of a gas phase within the pore space of the sample.

5.3 RESULTS AND DISCUSSION

During the period of diffusive equilibration of the porewater of the rock sample with I^- tracer, the X-ray attenuation of the rock sample increased gradually and then stabilized after 53 days (Figure 38). At this point, pores of the rock samples were saturated with I^- tracer and the equilibration with N_2 under high pressure was initiated.

After decreasing the N_2 pressure to 1 atm, the sample was monitored by X-ray radiography for 10 days (Figure 39) but most of the observed changes occurred in the early time. The results are not suitable for quantitative analysis but the following observations are relevant.

1) Previous radiography cell designs included a layer of fabric on each end of the sample to maintain a wetted surface at the boundaries. In this case, the fabric caused problems because it retains tracer solution which releases excess N_2 gas following the pressure decrease. As a result both Delrin® caps were pushed off immediately after the cell was assembled and the cell was opened to the atmosphere unexpectedly. The fabric was quickly removed and the cell was reassembled within 15 minutes.

2) The Delrin® caps did not expand evenly (Figure 39b) creating a risk of atmospheric gas contamination and disturbing sample alignment. This caused imprecision in the earliest attempts at radiographic imaging of these experiments. The cells have since been redesigned to avoid this problem (Section 5.4).

3) The general increase in $\Delta\mu_{gas}$ versus time (Figure 40) is consistent with an increase in gas partial saturation.

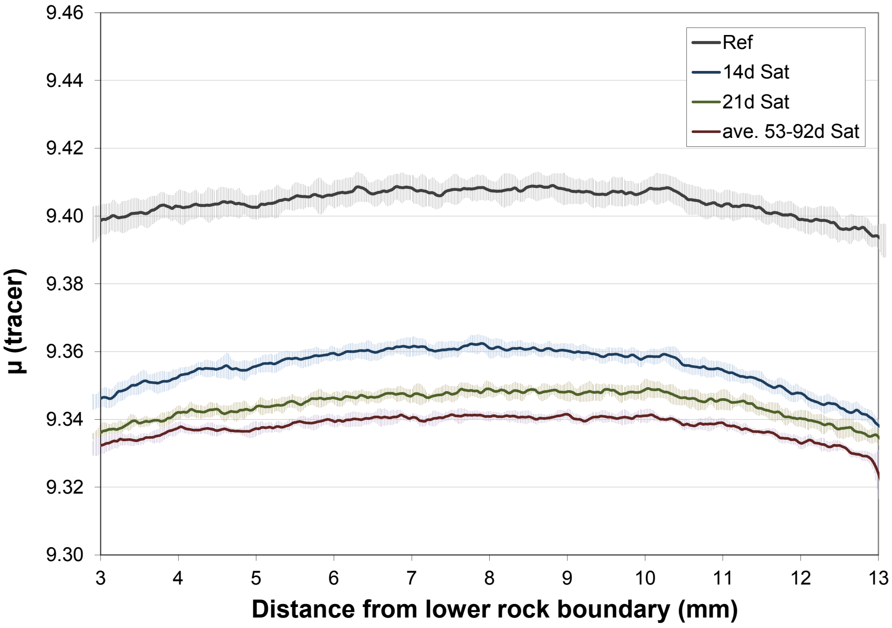

Figure 38: Profiles of μ_{tracer} Measured at 14, 21, 53 and 92 Days by the Radiography Method, Showing the Progress of Tracer Saturation. Standard Deviations are Represented by the Shaded Areas

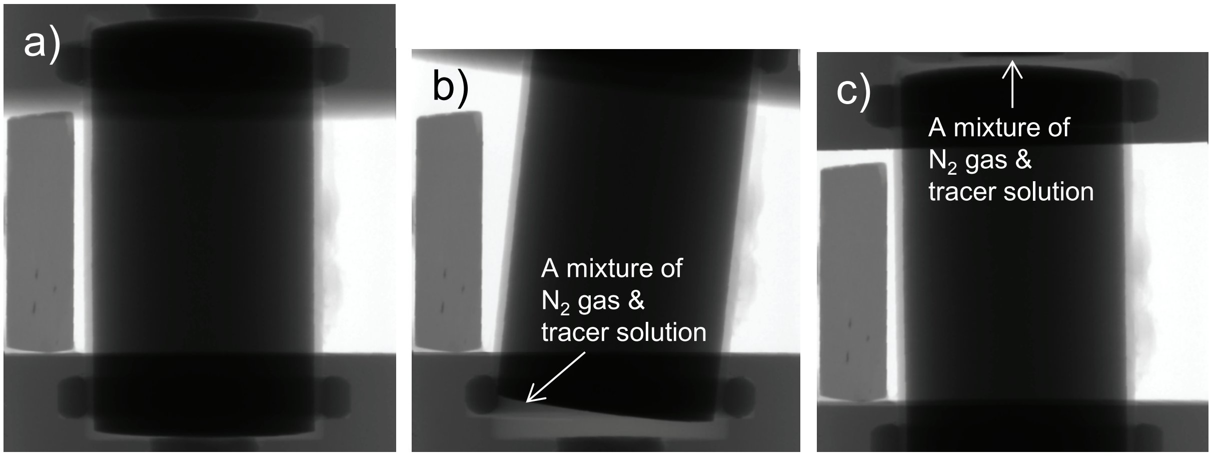

Figure 39: X-Ray Radiographs of Rock Sample DGR3-472 in the Partial Gas Saturation Cell, (a): after the Fabric was Removed and the Cell Re-assembled, (b): 1.5 hr, and (c): 2 hr after Image (a) was Recorded, Illustrating the Volume of the N_2 Gas and Tracer Solution Evolved from the Rock Sample at 1 atm

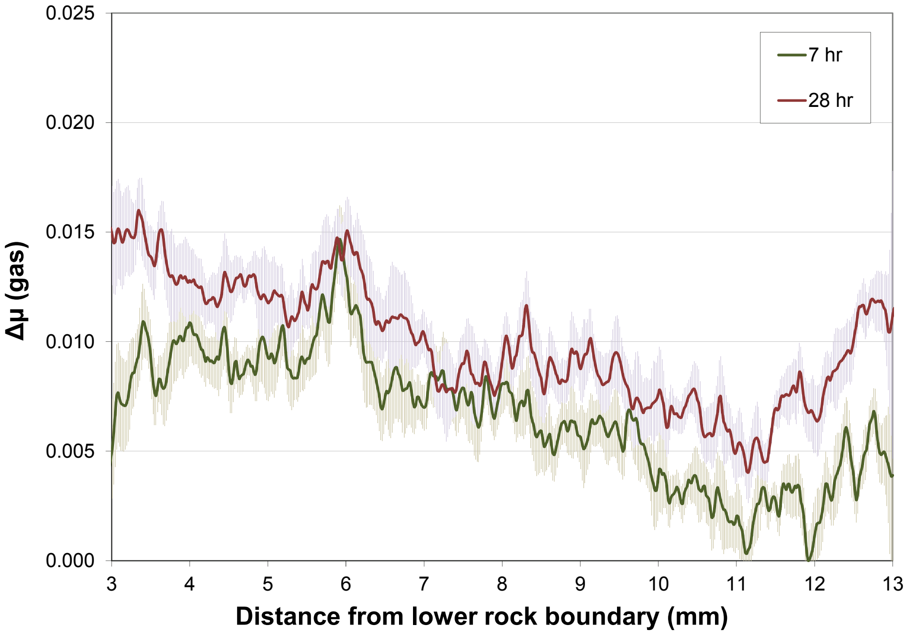

Figure 40: Profiles of $\Delta\mu_{gas}$ Collected 7 and 28 Hours after 800 psi N_2 was Released, Respectively. Standard Deviations are Represented by the Shaded Areas

5.4 MODIFICATIONS OF EXPERIMENTAL DESIGN AND FUTURE WORK

Although the results of the preliminary experiment indicate that it is possible to detect partial saturation using X-ray radiography, we aim to improve the precision, accuracy and detection limits for the measurements in future experiments. We plan to use a γ-ray source radiation imaging technique (Subudhi 2009; Subudhi et al. 2010) to monitor and measure partial saturation and to measure diffusion coefficients in partially-saturated porous media. This new technique employs an Am-241 radiation source, which will eliminate some of the limitations of the current X-ray radiography method, including beam hardening, artefacts from the cone-beam geometry, small instrument chamber size, and limited radiation exposure time. A new diffusion cell (Figure 41) has been designed for these experiments. The ability to work with longer exposure time, while eliminating the effects of beam hardening, should optimize the precision, accuracy and detection limit of the measurements.

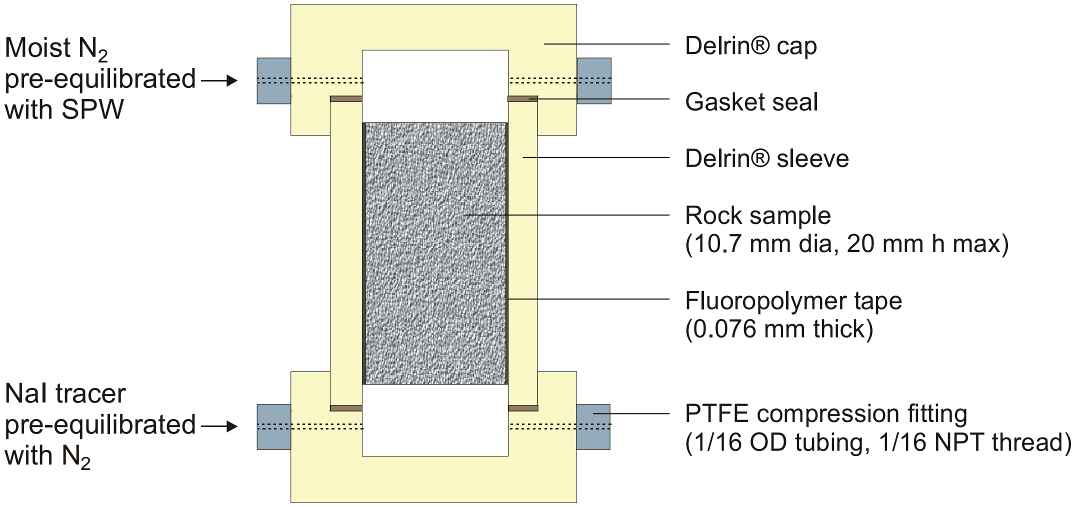

Figure 41: Proposed Diffusion Cell for the Partially Gas/Brine Saturated Rock Samples Using Am-241 γ-Ray Source

5.5 SUMMARY

The focus of this study was to develop a new method to introduce a controlled volume of gas into the rock pore spaces, and then use X-ray radiography to verify the degree of gas saturation achieved. The ultimate goal is to understand the effect of the gas phase on the diffusive transport of aqueous tracers by measuring the D_e values in fully and partially saturated rock samples. Results from preliminary investigations indicate:

- N_2 gas can be introduced into the rock pores using the pressure differential method as proposed.
- The time required for gas bubble formation in the rock pores is less than one day.
- Improvements are required in the radiation imaging methods before quantitative measurements of partial saturation can be achieved.

The next step is to investigate application of a radiation-imaging technique that utilizes an Am-241 gamma source to monitor the partial saturation and to conduct D_e measurements. This technique provides advantages over X-ray radiography in that beam hardening is eliminated and counting statistics are optimized by increasing radiation exposure time.

6. VISUALIZING DIFFUSION PATHWAYS

Imaging techniques to characterize rock pore geometry, distribution and connectivity have been widely used in different areas of engineering geology, such as the oil/gas industry (Ruzyla 1986; Celland and Fens 1991; Kuzmin 2007), CO_2 sequestration (Durocher et al. 2005; Krause et al. 2009), and radioactive waste management (Hellmuth et al. 1993; Holzer et al. 2010). Techniques including scanning electron microscopy (SEM) (Ruzyla 1986; Yokoyama and

Nakashima 2005), cathodoluminescence (CL) (Kuzmin 2007; Sokolov et al. 2007), transmission electron microscopy (TEM) (Lee 2010), and atomic force microscope (AFM) (Hirono et al. 2006) allow for visualizing 2D pore images in natural geological materials. Quantitative image analysis has been used with many of these methods to generate pore parameters, such as porosity fractions and anisotropy ratios. Three-dimensional images of rock pore structures showing the connectivity have been obtained using the non-destructive methods of laser scanning confocal microscopy (LSCM; Fredrich et al. 1995) and synchrotron X-ray CT (Lindquist et al. 2000), and destructive methods using focused ion beam (FIB) sectioning coupled with SEM and/or TEM imaging at submicron to nanometer scale (Tomutsa and Radmilovic 2003; Lee 2010; Holzer et al. 2010). A brief literature review that evaluates the potential for extending imaging methodology to the nanoscale is included in this report (Appendix E).

In this work, three approaches for visualizing diffusion pathways in low-permeability rock samples were explored to aid in understanding the relationship between diffusion and porosity networks at the micrometer scale: 1) AgI-SEM imaging, 2) SEM imaging using Ag-doped low-viscosity epoxy, and 3) cathodoluminescence (CL) imaging using luminescence-agent-doped low-viscosity epoxy.

6.1 AgI-SEM IMAGING

Elements with high atomic numbers, such as silver (Ag) and iodine (I), provide good imaging contrast using SEM in the Back Scattered Electron (BSE) mode. The approach for this method is to use $AgNO_3$ for fixation of I^- tracer (as AgI) in the rock pores, allowing for SEM visualization of I^--accessible pore networks.

6.1.1 Experimental Methods

Selected samples from completed through-diffusion experiments (76 mm or 25.4 mm diameter x 10 mm length), or from X-ray radiography experiments (11 mm diameter x 15 mm length), were saturated in 1 M I^- tracer solution and then immersed in $AgNO_3$ solution (0.1 M) for 6 to 12 days to allow Ag^+ ions to diffuse into the pores and fix the I^- ions in place by precipitation of AgI. Samples were then sectioned parallel to the diffusion path and polished thin-sections were prepared for SEM analysis.

In a slightly modified method, thin slices (approximately 5 mm thick) of DGR shale and hardbed samples were prepared, first by diamond saw cutting, and then by lapping to remove mechanical damage from saw cuts. The samples were glued on glass slides and immersed in 1 M I^- tracer solutions for up to 7 days, during which time all shale samples were damaged. After 7 days, the hardbed samples were immersed in 0.1 M $AgNO_3$ solution for 1 to 2 days to allow for the precipitation of AgI.

The SEM analyses were performed at the Microscopy and Microanalysis Facility at the University of New Brunswick using a JEOL JSM6400 Scanning Electron Microscope equipped with an EDAX Genesis energy-dispersive X-ray spectroscopy (EDS) system.

6.1.2 Results and Discussion

The distribution of AgI precipitate in the Georgian Bay Formation shale is indicated by the bright areas in the BSEI (Figure 42a), and the Ag and I elemental maps (Figure 42b). The fixation of I^- was limited to distances of less than several hundred µm because the near-surface diffusion pathways became blocked by AgI precipitate. Results suggest that the pathways are preferentially oriented parallel to bedding in this shale sample. The large microfracture with an aperture up to 12 µm is likely an artifact related to sample preparation.

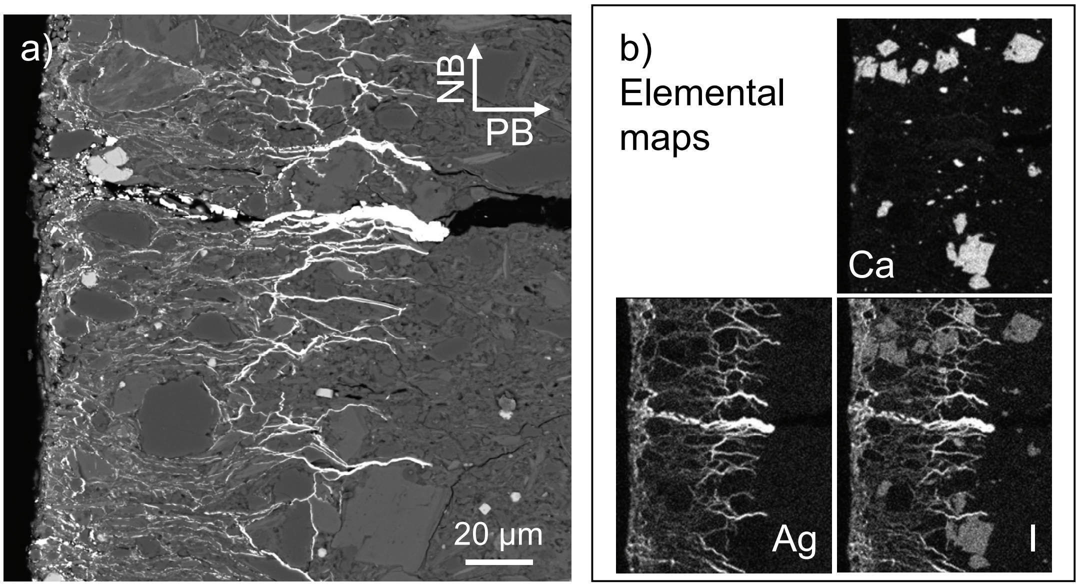

Figure 42: (a) BSE Image from a Georgian Bay Formation Shale Sample (DGR2-596) Illustrating the Distribution of AgI Precipitate in the Pores and (b) Elemental Maps from the Area Shown in (a)

The BSEI and EDS elemental images of argillaceous limestone samples (DGR3-688 and DGR4-719) shown in Figure 43 provide evidence for several different types of transport pathways.

1) Where dolomite is present, there are intergranular voids that are partially filled with clay minerals, and the presence of AgI within these voids indicates that they represent accessible diffusion pathways (Figure 43a-d).

2) In the calcite-rich areas, diffusion occurs principally along grain boundaries (Figure 43c, e).

3) The extensive accumulation of AgI in the argillaceous domains (Figure 43f, g) indicates that diffusion occurs preferentially in these regions.

4) Microfractures that are accessible to diffusive transport occur near the sample margin (Figure 43h) and likely represent artefacts of sample preparation.

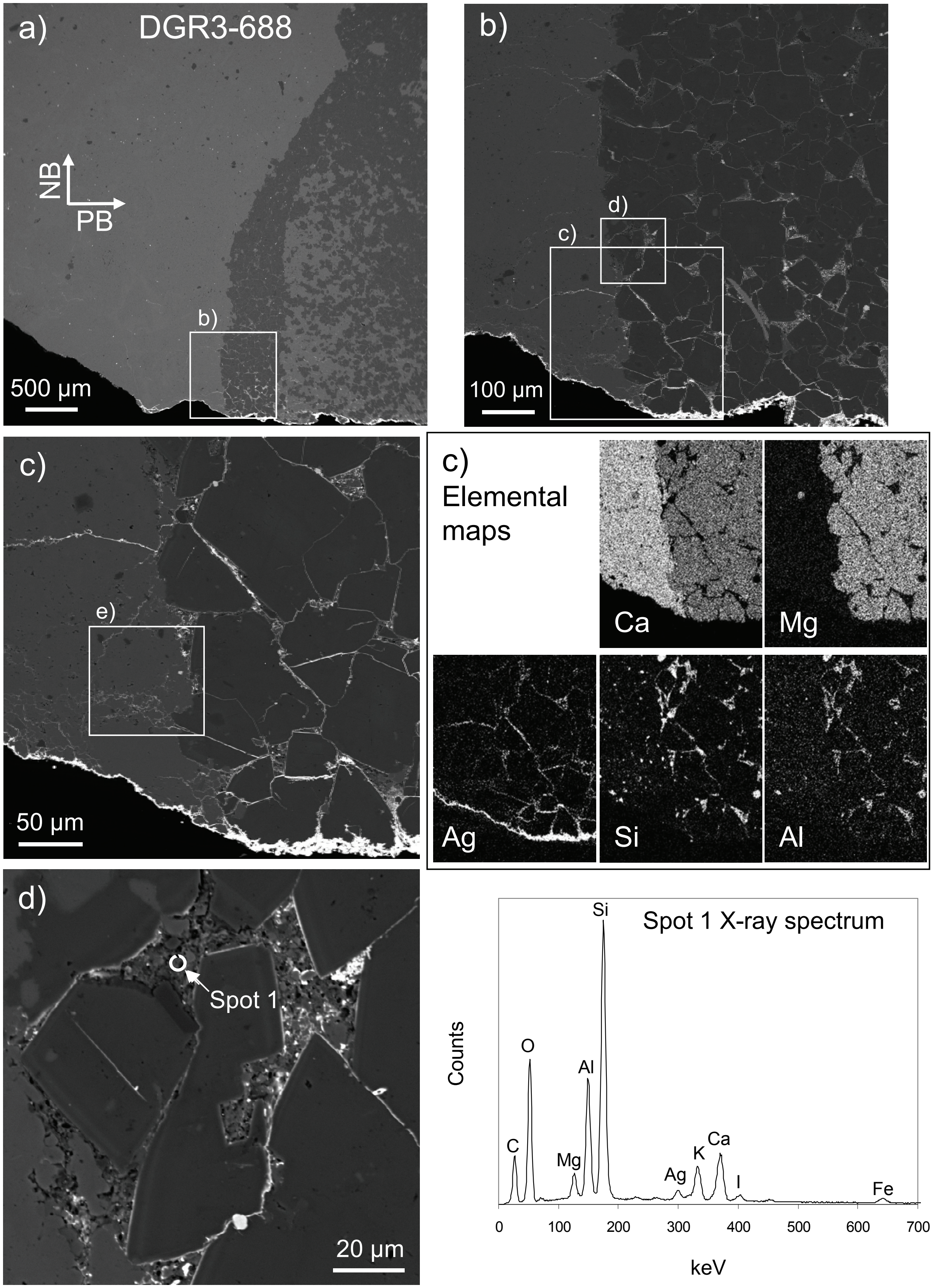
a)
DGR3-688
NB
PB
b)
500 µm
b)
d)
c)
100 µm
c)
e)
50 µm
c)
Elemental maps
Ca
Mg
Ag
Si
Al
d)
Spot 1
20 µm
Spot 1 X-ray spectrum
Counts
keV
C
O
Mg
Al
Si
Ag
K
Ca
I
Fe
0
100
200
300
400
500
600
700

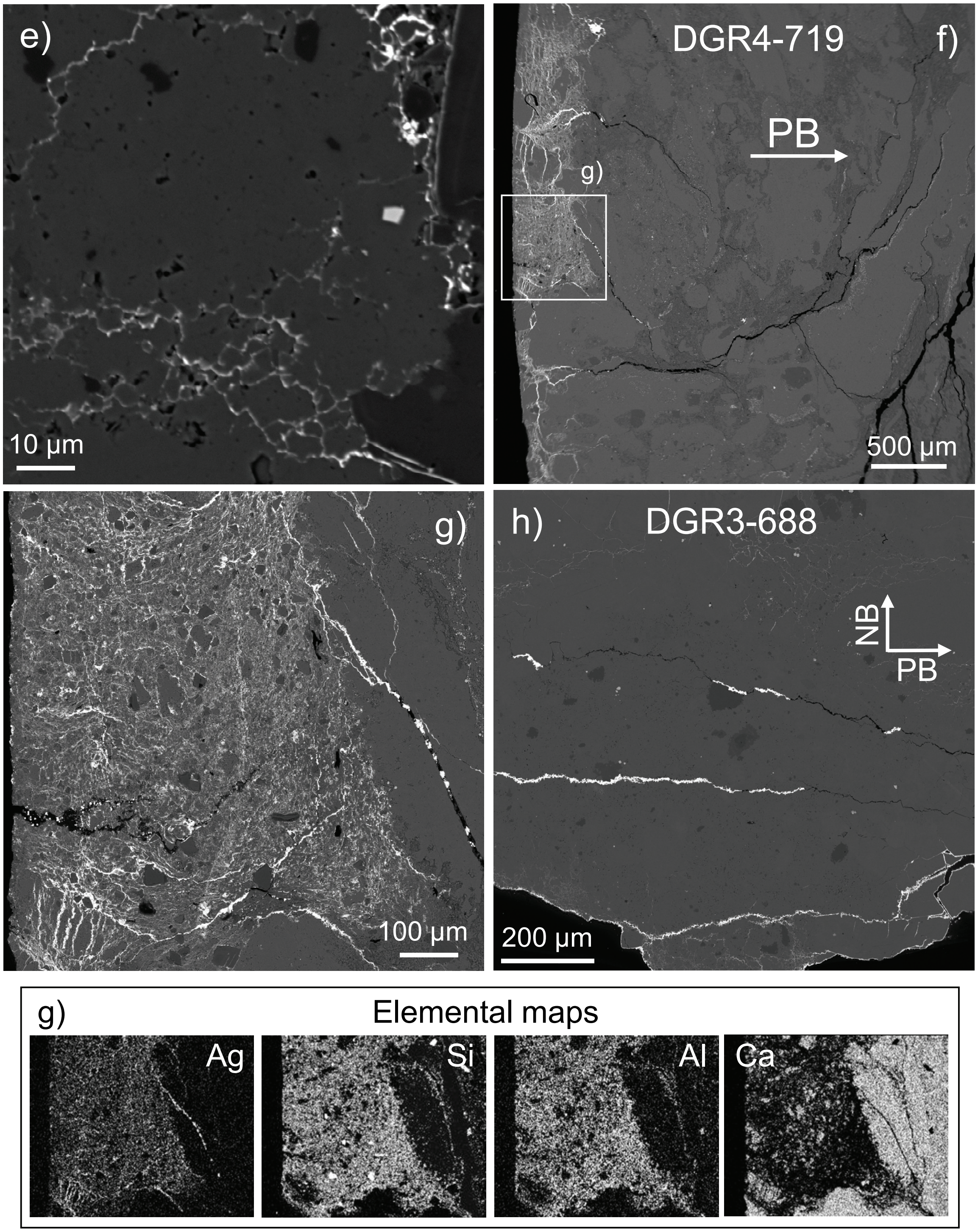

Figure 43: SEM Images from Argillaceous Limestone Samples. Areas (a) – (e): BSE Images from DGR3-688 Illustrating the Distribution of AgI Precipitate in the Pores, along with Elemental Maps from Area (c) and an EDS Spectrum from Spot 1 in Area (d), which Confirms the Clay Component. Areas (f) and (g): BSE Images from DGR4-719 along with Elemental Maps from Area (g). Area (h): BSE Image from DGR3-688 Illustrating Microfractures near the Sample Margin that Likely Relate to Sample Preparation

Microfractures with apertures up to 12 µm are evident in all rock types that were studied (Figures 42a and 43c, g). In some cases, particularly when they occur near the margins of the samples, these microfractures are thought to be artifacts related to sampling, sample preparation or AgI crystal growth. A modified preparation method was tested in an attempt to minimize sample damage; mounting slabs of rock on petrographic glass slide first and then fixing the I^- with $AgNO_3$ with the rock already mounted on the slide. Four of the shale subsamples (DGR2-517NB/PB and DGR2-597NB/PB) prepared this way fractured during sample preparation due to clay expansion. The expansion was so strong that the glass slides shattered. Argillaceous limestone and hardbed samples appeared to be intact after the procedure, but SEM imaging (DGR3-505, DGR3-681, and DGR4-822) indicated the persistent presence of microfractures. The sample preparation procedure was not successful so results are not shown.

Images from a siltstone hardbed (DGR2-544) in the Georgian Bay Formation shale indicate that the intergranular void spaces are filled with clay minerals (based on Si and Al distributions in elemental maps), and the AgI distribution demonstrates that these clay-filled voids represent diffusion accessible pathways (Figure 44).

6.2 SEM WITH SILVER-DOPED LOW-VISCOSITY EPOXY IMPREGNATION

In an effort to avoid mechanical damage due to rock/fracture expansion induced by AgI crystal growth, samples were impregnated with silver-doped low-viscosity epoxy prior to thin-section preparation. Silver was chosen because it has a high atomic number and therefore provides good contrast for BSE imaging. Silver cyclohexanebutyrate was reported to be stable and soluble in some non-polar organic solvents and, therefore, it was expected to be soluble in the epoxy (EPOTek-301-2FL).

6.2.1 Experimental Procedures

Silver cyclohexanebutyrate (~0.05 g) was dissolved in 0.518 g of EPOTek-301-2FL resin to reach the solubility limit, and then mixed with 0.181 g of the hardener. A few drops of the mixture were placed on the surface of a sandstone test sample and the epoxy allowed to flow into the rock pores. The time required for this low-viscosity epoxy to harden was 4-6 days at room temperature. Following the same procedures as described in Section 6.1.1, a polished petrographic thin-section was prepared and SEM-EDS images were collected.

6.2.2 Results and Discussion

Silver was not detected in SEM-BSE images, nor was the Ag signal detected with EDS. This result indicates that the solubility of silver cyclohexanebutyrate in the epoxy was below the detection capabilities for EDS analysis.

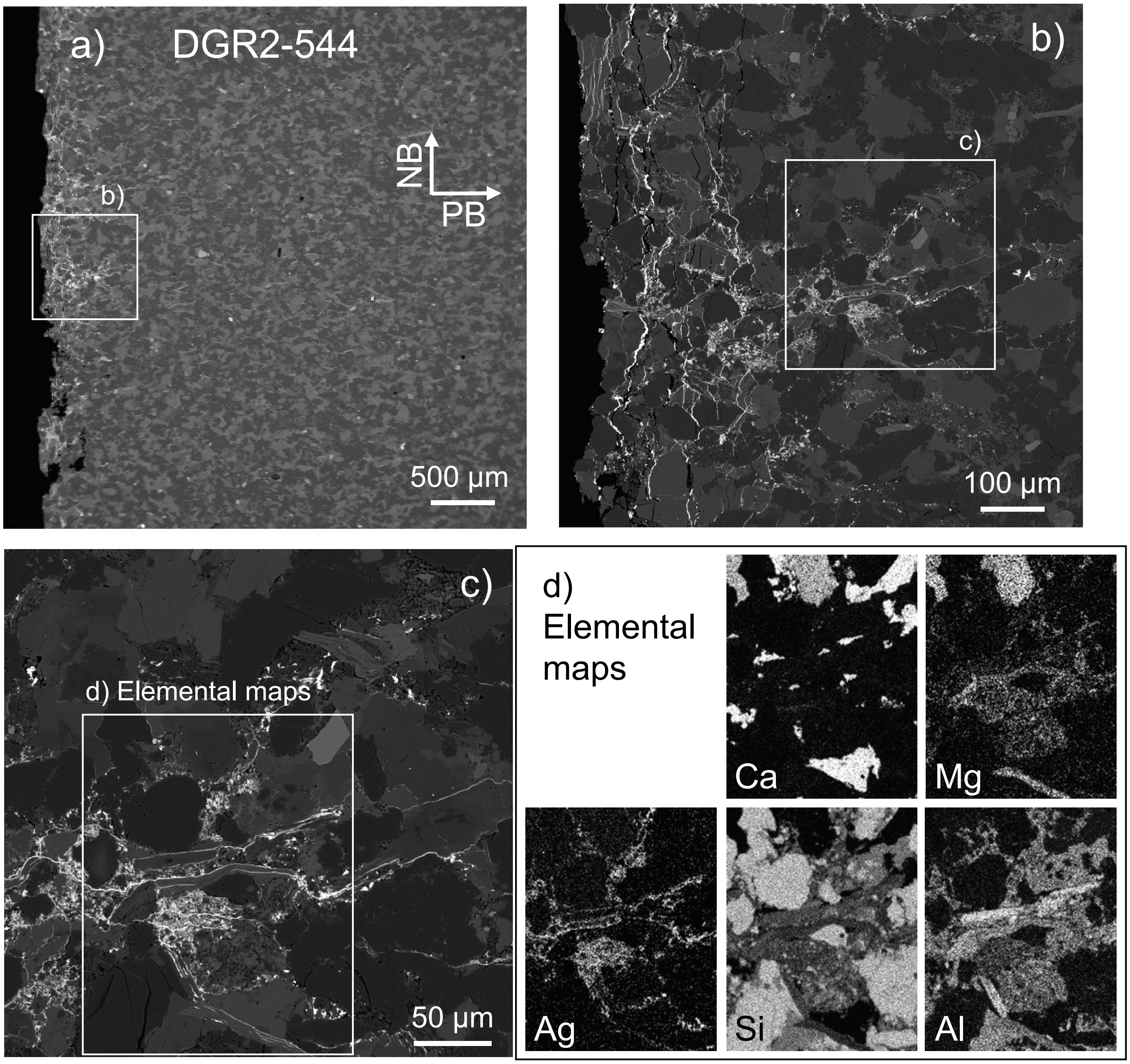

Figure 44: BSE Images (a) – (c) from a Siltstone Sample (DGR2-544) Illustrating the Distribution of AgI Precipitate in the Pores, and Elemental Maps Acquired by SEM/EDS from the Area Outlined in (c)

6.3 CATHODOLUMINESCENCE (CL) IMAGING

This attempt at porosity imaging involved impregnation of the rock pore spaces with a luminescent epoxy, followed by thin-section preparation and CL imaging (Kuzmin 2007; Sokolov et al. 2007).

6.3.1 Experimental Procedures

A fluorescent agent, 2,5-diphenyloxazol (PPO, $C_{15}H_{11}NO$), was added to the low-viscosity epoxy, EPOTek-301-2FL, by dissolving 0.015 g of PPO in 0.395 g of the epoxy hardener and then mixing with 1.129 g of the epoxy resin. A few drops of this mixture were placed on the surface of a sandstone sample and allowed to flow into the rock pores. Three polished petrographic thin-sections were prepared for SEM imaging: 1) a blank without epoxy, 2) a sample with epoxy but no fluorescent agent, and 3) a sample with PPO doped epoxy. Images were acquired in both BSE and CL imaging modes.

6.3.2 Results and Discussion

Images in Figure 45 indicate that the pore spaces in the sandstone test sample were filled with the low-viscosity epoxy, which, alone (without fluorescent agent), displays moderate luminescence in the green wavelength region (Figure 45b). The red regions in Figure 45b represent luminescent mineral grains and the dark areas represent non-luminescent mineral grains.

The mineral grains in the blank sandstone sample (Figure 46a) display some red, but mostly green luminescence, which cannot easily be distinguished from the green epoxy luminescence (Figure 45b).

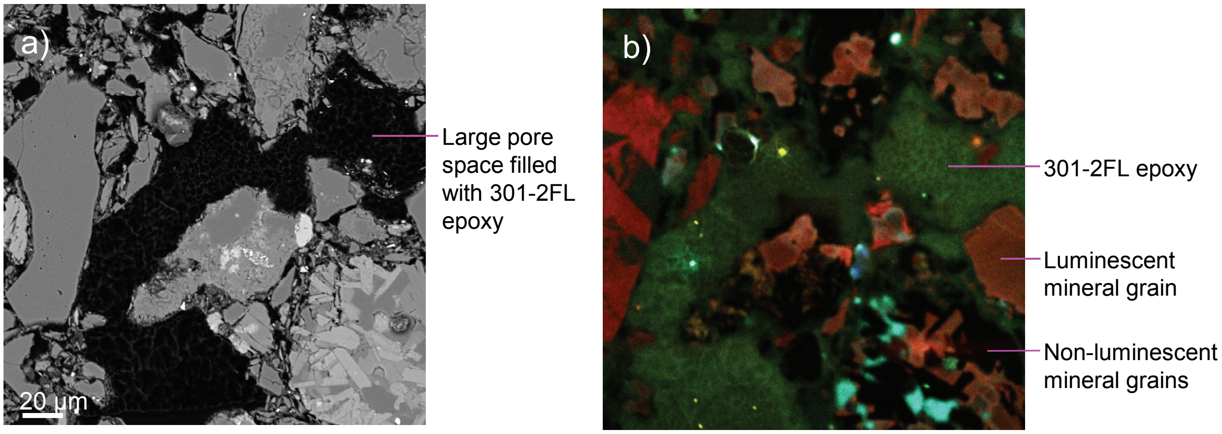

Figure 45: SEM Images from a Sandstone Sample Impregnated with EPOTek-301-2FL Low-Viscosity Epoxy (a) BSE Imaging Mode and (b) CL Imaging Mode

There was no additional CL signal observed for the sample impregnated with PPO-epoxy (Figure 46), indicating that the luminescence of doped epoxy is not strong enough to overcome the background from luminescent mineral grains.

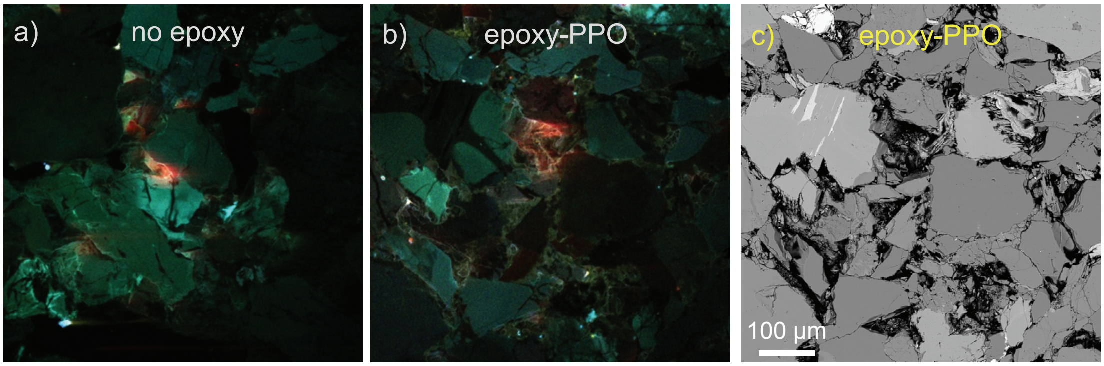

Figure 46: SEM Images from a Sandstone Sample, (a) CL Image of Untreated Sample, (b) CL Image of Sample Impregnated with Epoxy Doped with PPO, and (c) BSE Image of PPO-Doped Sample

6.4 SUMMARY

Three SEM-based techniques were investigated in an attempt to visualize diffusion-accessible pathways in porous media. Chemical agents were selected to enhance contrast between the mineral grains and the pores in the SEM images: 1) SEM-EDS imaging with AgI precipitate formed in the pores; 2) SEM-EDS imaging of pores filled with silver-doped epoxy; and 3) CL imaging of pores filled with epoxy doped with a luminescence agent. Only the first method produced images leading to meaningful scientific findings as summarized below:

- At the μm scale of SEM imaging, the diffusion pathways observed within the Georgian Bay Formation shale sample exhibit preferential orientation parallel to bedding, which is consistent with the alignment of clay minerals as a result of burial and consolidation.

- In the argillaceous limestone sample, diffusion occurs preferentially in the argillaceous component, and also along grain-boundaries in calcite-rich domains and within intergranular voids in dolomite-rich domains.

- In siltstone samples within the Georgian Bay Formation, the intergranular void spaces are filled with clay minerals, and these clay-filled voids provide diffusion-accessible pathways.

- Microfractures were observed in SEM images from all 3 rock samples tested using method (1). In many cases these microfractures are thought to be artefacts related to sample preparation. It is not possible to distinguish naturally-occurring microfractures from those which are artefacts of sampling and sample preparation.

  In attempts to avoid artifacts, a modified sample preparation procedure for imaging technique (1) (section 6.1) and two new techniques, (2) (section 6.2) and (3) (section 6.3), were tested. However, they were unsuccessful.

7. CONCLUDING REMARKS

This technical report documents the main activities and findings of research undertaken at the University of New Brunswick to i) develop new and improve current methodologies for laboratory measurements of diffusion properties of sedimentary rocks, and ii) to better understand the mechanisms controlling solute transport in diffusion-dominated sedimentary rock systems. Diffusion measurement techniques for low-permeability sedimentary rocks were advanced using new and/or modified methods in several areas: i) effective diffusion coefficient (D_e) measurements with confining pressure (CP) by through-diffusion; ii) improvements and advances in the X-ray radiography (RAD) method; iii) method development for creating partial gas/brine saturation conditions for diffusion studies in the future; and iv) imaging diffusion pathways with SEM. The results of these projects are summarized here.

DIFFUSION MEASUREMENTs WITH CONFINING PRESSURE

The through-diffusion technique was advanced to measure diffusion coefficient values in rock samples under confining pressures meant to simulate in situ pressure conditions. The method was tested successfully with four rock types representing three key lithologies. Both tritium (HTO) and iodide (I^-) tracers were used for this work. Overall, it was found that increasing the pressure from ambient laboratory conditions to in situ pressures (ΔP) decreased the measured D_e values by as much as 44%. Correction factors are suggested for the D_e values measured previously at ambient laboratory pressure to account for the effect of in situ stress on D_e.

REVISIONS TO THE RADIOGRAPHY CALIBRATION METHOD

The calibration used to quantify iodide-accessible porosity (ϕ_I) and, consequently the effective diffusion coefficient for iodide (D_{eI}), for the RAD method was revised. The new calibration method is also used when quantifying the concentration of the cesium in a rock sample, which is required to produce the C/C_0 profiles used in determining diffusion (D_{pCs}) and sorption parameters for this non-conservative tracer. The new method provides a better match between the X-Ray beam-hardening characteristics of the calibration materials (natural sandstones) and the rock samples than the glass vials which had previously been used for the calibration. The natural sandstones were used to estimate I^- concentration and ϕ_I values. The calibration for Cs^+ exploits relationships between the calibration functions of three different materials: glass vials, sandstones and ceramics.

MEASUREMENT OF DIFFUSION PROPERTIES BY X-RAY RADIOGRAPHY USING IODIDE AND CESIUM TRACERS: OPALINUS CLAY

The RAD method was used to make diffusion measurements on samples of Opalinus Clay from the Mont Terri URL in Switzerland using a conservative (I^-) and a non-conservative (Cs^+) tracer. The Opalinus Clay contains swelling clays. The RAD diffusion cell developed in previous studies was not designed to contain swelling samples, which resulted in erroneously high measured D_{eI} and ϕ_I values. The radiography cell was then re-designed to hold materials prone to swelling or disaggregation in confined conditions. The rigidity of the new cell was limited by the requirement for thin plastic materials with low X-ray absorption. Consequently, not all sample expansion was eliminated and control or monitoring of the confining pressure was not possible. However, the D_{eI} value determined when using the new RAD confining cell, 4.7×10^{-12} m^2/s, is consistent with published values for the Opalinus Clay. The new confining cell increases the range of samples for which diffusion measurements can be made by radiography.

For the non-conservative tracer, Cs^+, diffusion measurements were made under unconfined conditions only. Therefore, while absolute values for diffusion coefficients may have been overestimated, other aspects concerning the extension of the RAD method to a non-conservative tracer were investigated. The multicomponent reactive transport code MIN3P was used to perform diffusion-reaction transport simulations and to calculate total Cs^+ concentration versus distance profiles. Estimates of D_{pCs} and log $K_{Cs+/Na+}$ were obtained using the Model-Independent Parameter Estimation code, PEST.

The values for log $K_{Cs+/Na+}$ and CEC were found to be strongly correlated, so the CEC was set to 12.4 meq/100g - a value for Opalinus Clay obtained from recent published literature (Appelo et al. 2010). The fitted range of values for log $K_{Cs+/Na+}$ was 1.4 to 2.1, which is consistent with published values of log $K_{Cs+/Na+}$ dominated by planar sites. A decrease in log $K_{Cs+/Na+}$ was observed as the Cs^+ concentration in the tracer increased, which is consistent with expectations based on literature reports describing the characteristics of multiple binding sites on illite.

For some samples oriented normal to bedding, sample heterogeneities were observed and were reflected in the data. Improvements to the model fit were achieved by allowing for variable porosity and D_{pCs} in the diffusion-reaction simulations.

INVESTIGATING EFFECTS OF PARTIAL SATURATION ON DGR ROCKS

The focus of this study was to develop a new method to introduce a controlled volume of gas into the rock pore spaces, and then use X-ray radiography to verify the degree of gas saturation achieved. The ultimate goal is to understand the effect of the gas phase on the diffusive transport of aqueous tracers by measuring the D_e values in fully and partially saturated rock samples. Preliminary results from X-ray radiography investigations provided valuable information for the future work with a radiation-imaging technique that utilizes an Am-241 gamma source to monitor the partial saturation and to conduct D_e measurements. The γ-ray technique provides advantages over X-ray radiography in that beam hardening is eliminated and counting statistics are optimized by increasing radiation exposure time.

VISUALIZING DIFFUSION PATHWAYS

Three SEM-based techniques were investigated in an attempt to visualize diffusion-accessible pathways in porous media. Chemical agents were selected to enhance contrast between the mineral grains and the pores in the SEM images: 1) SEM-EDS imaging with AgI precipitate formed in the pores; 2) SEM-EDS imaging of pores filled with silver-doped epoxy; and 3) CL imaging of pores filled with epoxy doped with a luminescence agent. Only the first method produced images leading to scientific findings that improved our understanding of mechanisms controlling solute transport in diffusion-dominated sedimentary rock systems.

ACKNOWLEDGEMENTS

We gratefully acknowledge contributions of core samples and related information from Martin Mazurek (University of Bern), Olivier Leupin (NAGRA) and Thomas Gimmi (Paul Scherrer Institute). We also thank the staff of the UNB Microscopy and Microanalysis Facility for their technical support with the microCT, SEM and TEM.

REFERENCES

Al, T., Y. Xiang and L. Cavé. 2009. Measurement of diffusion properties by X-ray radiography and by through-diffusion techniques using iodide and tritium tracers: Core samples from OS-1 and DGR-2. Prepared by the University of New Brunswick for Geofirma Engineering Ltd. (previously Intera Engineering Ltd.). Technical Report TR-07-17 Revision 2A, February 3, 2009. Canada.

Al, T., Y. Xiang, D. Loomer and L. Cavé. 2012. Measurement of diffusion properties by X-ray radiography and by through-diffusion techniques using iodide and tritium tracers: Core samples from DGR-3 and DGR-4. Report prepared by the University of New Brunswick for Geofirma Engineering Ltd. (previously Intera Engineering Ltd.). Technical Report TR-08-27 Revision 2A, May, 2012. Canada.

Aldaba, D., R. Fernández-Torrent, G. Rauret, M. Vidal and A. Rigol. 2010. Laboratory experiments to characterize radiochloride diffusion in unsaturated soils. Applied Radiation and Isotopes 68, 393-398.

Appelo, C.A.J. and D. Postma. 2005. Geochemistry, Groundwater and Pollution. 2nd Edition. A.A. Balkema, Amsterdam, 649 pp.

Appelo, C.A.J., L.R. Van Loon and P. Wersin. 2010. Multicomponent diffusion of a suite of tracers (HTO, Cl, Br, I, Na, Sr, Cs) in a single sample of Opalinus Clay. Geochimica et Cosmochimica Acta 74, 1201-19.

Barraclough, P.B. and P.B. Tinker. 1981. The determination of ionic diffusion coefficients in field soils. I. Diffusion coefficients in sieved soils in relation to water content and bulk density. Journal of Soil Science 32, 225-236.

Bazer-Bachi, F., E. Tevissen, M. Descostes, B. Grenut, P. Meier, M.-O. Simonnot and M. Sardin. 2006. Characterization of iodide retention on Callovo-Oxfordian argillites and its influence on iodide migration. Physics and Chemistry of the Earth 31, 517-522.

Bradbury, M.H. and B. Baeyens. 1998. A physicochemical characterisation and geochemical modelling approach for determining porewater chemistries in argillaceous rocks. Geochimica et Cosmochimica Acta 62, 783-795.

Bradbury, M.H. and B. Baeyens. 2000. A generalized sorption model for the concentration dependent uptake of caesium by argillaceous rocks. Journal of Contaminant Hydrology 42, 141-163.

Cavé, L., T. Al, Y. Xiang and P. Vilks. 2009a. A technique for estimating one-dimensional diffusion coefficients in low permeability sedimentary rock using X-ray radiography: Comparison with through-diffusion measurements. Journal of Contaminant Hydrology 103, 1-12.

Cavé, L., T. Al and Y. Xiang. 2009b. X-ray radiography techniques for measuring diffusive properties of sedimentary rocks. Prepared by the University of New Brunswick. Nuclear Waste Management Organization Technical Report NWMO TR-2009-03, February 2009. Toronto, Canada. (Available at http://www.nwmo.ca)

Cavé, L., T. Al, Y. Xiang and D. Loomer. 2010. Investigations of diffusive transport processes in sedimentary rock. Prepared by the University of New Brunswick. Nuclear Waste Management Organization Technical Report NWMO TR-2010-04, June 2010. Toronto, Canada. (Available at http://www.nwmo.ca)

Celland, W.D. and T.W. Fens. 1991. Automated rock characterization with SEM/image-analysis techniques. SPE Formation Evaluation 6, 437-443.

Churcher, P.L., P.R. French, J.E. Shaw and L.L. Schramm. 1991. Rock properties of Berea sandstone, Baker dolomite, and Indiana limestone. SPE 21044, 431-449. SPE International Symposium on Oilfield Chemistry. Anaheim, California, February 20-22, 1991.

Conca, J.L. and J. Wright. 1992. Diffusion and flow in gravel, soil and whole rock. Applied Hydrogeology 1, 5-24.

Corkum, A.G. and C.D. Martin. 2007a. The mechanical behaviour of weak mudstone (Opalinus Clay) at low stresses. International Journal of Rock Mechanics & Mining Sciences 44, 196-209.

Corkum, A.G. and C.D. Martin. 2007b. Modelling a mine-by test at the Mont Terri rock laboratory, Switzerland. International Journal of Rock Mechanics & Mining Sciences 44, 846-859.

Delage, P., M.D. Howat and Y.J. Cui. 1998. The relationship between suction and swelling properties in a heavily compacted unsaturated clay. Engineering Geology 50, 31-48.

Doherty, J. 2010. Open-source model-independent parameter estimation and uncertainty analysis software - PEST. Version 12.2. (Available at http://www.pesthomepage.org/)

Domenico, S.N. 1976. Effect of brine-gas mixture on velocity in an unconsolidated sand reservoir. Geophysics 41, 882-894.

Durocher, K., T. Kotzer and S. Whittaker. 2005. Physical and chemical characterization of subterranean CO_2 storage sites using synchrotron-based computed microtomography techniques. *In* Summary of Investigations 2005, Volume 1, Saskatchewan Geological Survey, Sask. Industry Resources, Misc. Rep. 2005-4.1, CD-ROM, Paper A-3, 7.

Emerson, D.W. 1990. Notes on mass properties of rocks – density, porosity, permeability. Exploration Geophysics 21, 209-216.

FORGE. 2010. Review of Boom Clay and Opalinus Clay parameters. FORGE report D4.6-VER 1.0, prepared by Fate of Repository Gases. (Available at http://www.bgs.ac.uk/forge/docs/reports/D4.6.pdf)

Fredrich, J.T., B. Menéndez and T.-F. Wong. 1995. Imaging the pore structure of geomaterials. Science 268, 276-279.

Frisillo, A.L. and T.J. Stewart. 1980. Effect of partial gas/brine saturation on ultrasonic absorption on sandstone. Journal of Geophysical Research 85, 5209-5211.

García-Gutiérrez, M., J.L. Cormenzana, T. Missana, M. Mingarro and P.L. Martín. 2006. Large-scale laboratory diffusion experiments in clay rocks. Physics and Chemistry of the Earth 31, 523-530.

Gimmi, T., O.X. Leupin, J. Eikenberg, M.A. Glaus, L.R. van Loon, H.N. Waber, P. Wersin, H.A.O. Wang, D. Grolimund, C.N. Borca, S. Dewonck and C. Wittebroodt. 2014. Anisotropic diffusion at the field scale in a 4-year multi-tracer diffusion and retention experiment – I: Insights from the experimental data. Geochimica et Cosmochimica Acta 125, 373-393.

Gorski, B., T. Anderson and T. Conlon. 2009. Laboratory geomechanical strength testing of DGR-1 & DGR-2 core. Prepared by CANMET Mining and Mineral Sciences Laboratories, Natural Resources Canada for Geofirma Engineering Ltd. (previously Intera Engineering Ltd.). Technical Report TR-07-03 Revision 3, February, 2009.

Gorski, B., D. Rodgers and T. Conlon. 2011. Laboratory geomechanical strength testing of DGR-2 to DGR-6 core. Prepared by CANMET Mining and Mineral Sciences Laboratories, Natural Resources Canada for Geofirma Engineering Ltd. Technical Report TR-09-07 Revision 0, April 7, 2011.

Hellmuth, K.H., M. Siitari-Kauppi and A. Lindberg. 1993. Study of porosity and migration pathways in crystalline rock by impregnation with ^{14}C-polymthylmethacrylate. Journal of Contaminant Hydrology 13, 403-418.

Hirono, T., W. Lin and S. Nakashima. 2006. Pore space visualization of rocks using an atomic force microscope. International Journal of Rock Mechanics & Mining Sciences 43, 317-320.

Holzer, L., R. Wepf, B. Münch and P. Marschall. 2010. Multiscale imaging of the pore structure of Opalinus Clay. Clays in Natural & Engineered Barriers for Radioactive Waste Confinement. 4th International Meeting, March 2010, Nantes, France.

Jakob, A., W. Pfingsten and L. van Loon. 2009. Effects of sorption competition on cesium diffusion through compacted argillaceous rock. Geochimica et Cosmochimica Acta 73, 2441-2456.

Koroleva, M., A. de Haller, U. Mäder, H.N. Waber and M. Mazurek. 2009. Borehole DGR-2: Pore-water investigations. A report prepared by the Institute of Geological Sciences University of Bern, Switzerland, Revision April, 2009.

Koroleva, M., C. Lerouge, U., Mäder, F. Claret and E. Gaucher. 2011. Biogeochemical processes in a clay formation in situ experiment: Part B – Results from overcoring and evidence of strong buffering by the rock formation. Applied Geochemistry 26, 954-966.

Krause, M., J.-C. Perrin, C.-W. Kuo and S.M. Benson. 2009. Characterization of CO_2 storage properties using core analysis techniques and thin section data. Energy Procedia 1, 2969-2974.

Kuzmin, V.A. 2007. Cathodoluminescence technique for studying the pore space of rock using scanning electron microscopy. Journal of Surface Investigation. X-ray, Synchrotron and neutron techniques 1, 687-690.

Lauber, M., B. Baeyens and M.H. Bradbury. 2000. Physico-chemical characterisation and sorption measurements of Cs, Sr, Ni, Eu, Th, Sn and Se on Opalinus Clay from Mont Terri. PSI Bericht Report Nr. 00-10, Switzerland, 77 p.

Lee, M.R. 2010. Transmission electron microscopy (TEM) of Earth and planetary materials: A review. Mineralogical Magazine 74, 1-27.

Li, Y. and S. Gregory. 1974. Diffusion of ions in sea water and in deep-sea sediments. Geochimica and Cosmochimica Acta 38, 703-714.

Lim, P.C., S.L. Barbour and D.G. Fredlund. 1998. The influence of degree of saturation on the coefficient of aqueous diffusion. Canadian Geotechnical Journal 35, 811-827.

Lindquist, W.B., A. Venkatarangan, J. Dunsmuir, T.-F. Wong. 2000. Pore and throat size distributions measured from synchrotron X-ray tomographic images of Fontainebleau sandstones. Journal of Geophysical Research 105, 21509-21527.

Lutus, P. 2011. PolySolve Version 3.4 (02-27-2011). Polynomial Regression Data Fit java applet. (Available at http://www.arachnoid.com/polysolve/index.html)

Mao, S. and Z. Duan. 2006. A thermodynamic model for calculating nitrogen solubility, gas phase composition and density of the N_2-H_2O-NaCl system. Liquid Phase Equilibria 248, 103-114

Mayer, K.U., E.O. Frind and D.W. Blowes. 2002. Multicomponent reactive transport modeling in variably saturated porous media using a generalized formulation for kinetically controlled reactions. Water Resources Research 38, 1174-1194.

Mazurek, M., A. Gautschi, P. Marschall, G. Vigneron, P. Lebon and J. Delay. 2008. Transferability of geoscientific information from various sources (study sites, underground rock laboratories, natural analogues) to support safety cases for radioactive waste repositories in argillaceous formations. Physics and Chemistry of the Earth 33, S95-S105.

Melkior, T., D. Mourzagh, S. Yahiaoui, D. Thoby, J.C. Alberto, C. Brouard and N. Michau. 2004. Diffusion of an alkaline fluid through clayey barriers and its effect on the diffusion properties of some chemical species. Applied Clay Science 26, 99-107.

Melkior, T., S. Yahiaoui, S. Motellier, D. Thoby and E. Tevissen. 2005. Cesium sorption and diffusion in Bure mudrock samples. Applied Clay Science 29, 172-186.

Mosser-Ruck, R., K. Devineau, D. Charpentier and M. Cathelineau. 2005. Effects of ethylene glycol saturation protocols on XRD patterns: A critical review and discussion. Clay and Clay Minerals 53, 631-638.

NWMO. 2011. Regional Geomechanics – Southern Ontario, NWMO DGR-TR-2011-13, prepared by Nuclear Waste Management Organization and AECOM Canada Ltd. (Available at www.nwmo.ca)

Pace, M.N., M.A. Mayes, P.M., Jardine, L.D. McKay, X.L. Yin, T.L. Mehlhorn, Q. Liu and H. Gurleyuk. 2007. Transport of Sr^{2+} and $SrEDTA^{2-}$ in partially-saturated and heterogeneous sediments. Journal of Contaminant Hydrology 91, 267-287.

Palut, J.-M., Ph. Montarnal, A. Gautschi, E. Tevissen and E. Mouche. 2003. Characterisation of HTO diffusion properties by an in situ tracer experiment in Opalinus clay at Mont Terri. Journal of Contaminant Hydrology 61, 203-218.

Parkhurst, D.L. and C.A.J. Appelo. 1999. User's guide to PHREEQC (Version 2) – A computer program for speciation, batch-reaction, one-dimensional transport and inverse geochemical calculations. Water-Resources Investigations Report 99-4259. U.S. Department of the Interior, U.S. Geological Survey, Denver, Colorado.

Pearson, F.J., D. Arcos, A. Bath, J.-Y. Boisson, A.M. Fernández, H.-E. Gäbler, E. Gaucher, A. Gautschi, L. Griffault, P. Hernán and H.N. Waber. 2003. Mont Terri project – geochemistry of water in the Opalinus Clay Formation at the Mont Terri Rock Laboratory. Reports of the Swiss Federal Office for Water and Geology (FOWG), Geology Series No. 5, 319 p.

Plummer, M.A., L.C. Hull and D.T. Fox. 2004. Transport of carbon-14 in a large unsaturated soil column. Vadose Zone Journal 3, 109-121.

Raven, K., D. McCreath, R. Jackson, I. Clark, D. Heagle, S. Sterling and J. Avis. 2010. Descriptive geosphere site model, Deep Geologic Repository Bruce Nuclear Site. Report prepared by Geofirma Engineering Ltd. (previously Intera Engineering Ltd.). Technical Report TR-08-01 Revision 1C, April 15, 2010. Canada.

Ruzyla, K. 1986. Characterization of pore space by quantitative image analysis. SPE Formation Evaluation 1, 389-398.

Savoye, S., J. Page, C. Puente, C. Imbert and D. Coelho. 2010. New experimental approach for studying diffusion through an intact and unsaturated medium: A case study with Callovo-Oxfordian argillite. Environmental Science & Technology 44, 3698-3704.

Sokolov, V.N., O.V. Razgulina, D.I. Yurkovets and M.S. Chernov. 2007. Quantitative analysis of pore space of Moraine clay soils by SEM images. Journal of Surface Investigation. X-ray, Synchrotron and Neutron Techniques 1, 417-422.

Subudhi, R.K. 2009. A radiation transmission technique for the spatially-resolved measurement of porosity and diffusion properties of porous media. M. Sc. Thesis, University of New Brunswick, Canada.

Subudhi, R.K., E.A. Hussein and T. Al. 2010. Measurement of spatial distribution of total and accessible porosity in sedimentary rocks using isotopic radiation transmission: Device design and testing. Applied Radiation and Isotopes 68, 496-504.

Tevissen, E., J.M. Soler, P. Montarnal, A. Gautschi and L.R. Van Loon. 2004. Comparison between in situ and laboratory diffusion studies of HTO and halides in Opalinus Clay from the Mont Terri. Radiochimica Acta 92, 781-786.

Tomutsa, L. and V. Radmilovic. 2003. Focussed ion beam assisted three-dimensional rock imaging at submicron scale. Lawrence Berkeley National Laboratory: Lawrence Berkeley National Laboratory. LBNL Paper LBNL-52648.

van Loon, L.R., J.M. Soler and M.H. Bradbury. 2003a. Diffusion of HTO, $^{36}Cl^-$ and $^{125}I^-$ in Opalinus Clay samples from Mont Terri: Effect of confining pressure. Journal of Contaminant Hydrology 61, 73-83.

van Loon, L.R., J.M., Soler, A. Jakob and M.H., Bradbury. 2003b. Effect of confining pressure on the diffusion of HTO, $^{36}Cl^-$ and $^{125}I^-$ in a layered argillaceous rock (Opalinus Clay): Diffusion perpendicular to the fabric. Applied Geochemistry 18, 1653-1662.

van Loon, L.R., P. Wersin, J.M. Soler, J. Eikenberg, Th., Gimmi, P. Hernan, S. Dewonck and S. Savoye. 2004. In-situ diffusion of HTO, $^{22}Na^+$, Cs^+ and I^- in Opalinus Clay and the Mont Terri underground rock laboratory. Radiochimica Acta 92, 757-763.

van Loon, L.R., M. A. Glaus and W. Muller. 2007. Anion exclusion effects in compacted bentonites: Towards a better understanding of anion diffusion. Applied Geochemistry 22, 2536-2552.

van Loon, L., B. Baeyens and M.H. Bradbury. 2009. The sorption behaviour of caesium on Opalinus clay: A comparison between intact and crushed material. Applied Geochemistry 24, 999-1004.

Wersin, P., L.R. van Loon, J.M. Soler, A. Yllera, J. Eikenberg, Th. Gimmi, P. Hernan and J.-Y. Boisson. 2004. Long-term diffusion experiment at Mont Terri: First results from field and laboratory data. Applied Clay Science 26, 123-135.

Wersin, P., J.M. Soler, L. Van Loon, J. Eikenberg, B. Baeyens, D. Grolimund, T. Gimmi and S. Dewonck. 2008. Diffusion of HTO, Br^-, I^-, Cs^+, $^{85}Sr^{2+}$ and $^{60}Co^{2+}$ in a clay formation: Results and modelling from an in situ experiment in Opalinus Clay. Applied Geochemistry 23, 678-691.

Yin, C.-S., M.L. Batzle and B.J. Smith. 1992. Effects of partial liquid/gas saturation on extensional wave attenuation in Berea sandstone. Geophysical Research Letters 19, 1399-1402.

Yokoyama, T. and S. Nakashima. 2005. Diffusivity anisotropy in a rhyolite and its relation to pore structure. Engineering Geology 80, 328-335.

APPENDIX A: CALCITE EQUILIBRIUM MODELLING

What will happen if a tracer solution that is undersaturated with respect to calcite is used in an Opalinus Clay sample for radiographic diffusion measurements?

When a tracer that is undersaturated with respect to calcite is introduced into the reservoir and placed in contact with rock that contains calcite, there will be a zone in the sample near that contact where calcite will dissolve until the tracer solution equilibrates with the calcite in the sample (Figure A 1). The dissolution of calcite should result in increased porosity in the sample and the question becomes, is the quantity of calcite dissolved significant when compared to the overall porosity of the sample? The approach taken to answer this question was to use PHREEQC (Version 2.17.3;Parkhurst and Appelo 1999) to estimate the amount of calcite that would be dissolved after equilibrating the NaI tracer solution with sample CO_2 and calcite. From that, the resultant increase in pore space in the sample was estimated. The estimated increase in pore space from calcite dissolution was then compared to the overall porosity of the Opalinus Clay (OPA).

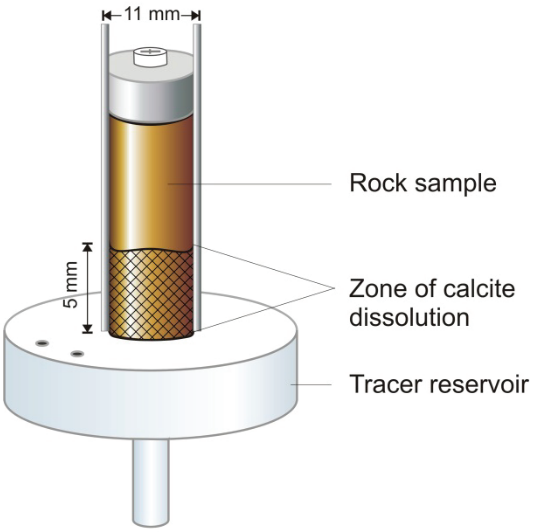

Figure A 1: Conceptual model of the effect of introducing a tracer solution that is undersaturated with respect to calcite into a sample that contains calcite

The equilibrium modeling was performed using a range of sample pCO_2 values, -3.0, -2.0 and -1.0 (atmospheric pCO_2 values are -3.4), to provide a range of possible values for the quantity of calcite dissolved (Input file is shown in Table A 1). The results from PHREEQC are given as the amount of calcite dissolved per litre which was converted to the volume in the sample by assuming a 5.5 mm sample radius, a 5 mm long zone of equilibration in the sample (the region of interest) and a sample porosity of 0.16 (Mazurek et al. 2008). The estimated volume of calcite that would be dissolved in the region of interest ranged from 3.8 to 18 x 10^{-9} L based on pCO_2 values ranging from -3.0 to -1.0. The pore volume for the Opalinus Clay within that region of interest was estimated to be 7.6 x 10^{-5} L. The volume of calcite that would be dissolved would be approximately 4 orders of magnitude smaller than the volume of the samples' pore space. Therefore, the effect of calcite dissolution that may occur as a result of using a NaI tracer solution that is undersaturated with respect to calcite is considered negligible for the radiographic diffusion measurements on Opalinus Clay samples.

Table A 1: The PHREEQC Input File for the Calcite Equilibrium Modelling

```
TITLE OPA Tracer
# Solute activities calculated with Wateq4f database

SELECTED_OUTPUT
        -file           OPA_tracer_final wateq4f Cl 20101020.txt
        -reset    false
        -solution
        -pH
        -charge_balance
    -totals             Alkalinity Na Cl I
        -ionic_strength
        -SI                                 calcite
        -equilibrium_phases   calcite

SOLUTION 1  NaI TRACER
        units     mol/L
        temp      23
        pH        5.5       #pH of distilled water
        pe        4
        redox     pe
        Na        0.39
        Cl                  0.39
        density   1.013
EQUILIBRIUM_PHASES 1
        CO2(g)    -1.0
        calcite   0
END

SOLUTION 2  NaI TRACER
        units     mol/L
        temp      23
        pH        5.5       #pH of distilled water
        pe        4
        redox     pe
        Na        0.39
        Cl                  0.39
        density   1.013
EQUILIBRIUM_PHASES 2
        CO2(g)    -2.0
        calcite   0
END

SOLUTION 3  NaI TRACER
        units     mol/L
        temp      23
        pH        5.5       #pH of distilled water
        pe        4
        redox     pe
        Na        0.39
        Cl                  0.39
        density   1.013
EQUILIBRIUM_PHASES 3
        CO2(g)    -3.0
        calcite   0
END
```

APPENDIX B: RADIOGRAPHY DIFFUSION PROFILES USING AN IODIDE TRACER

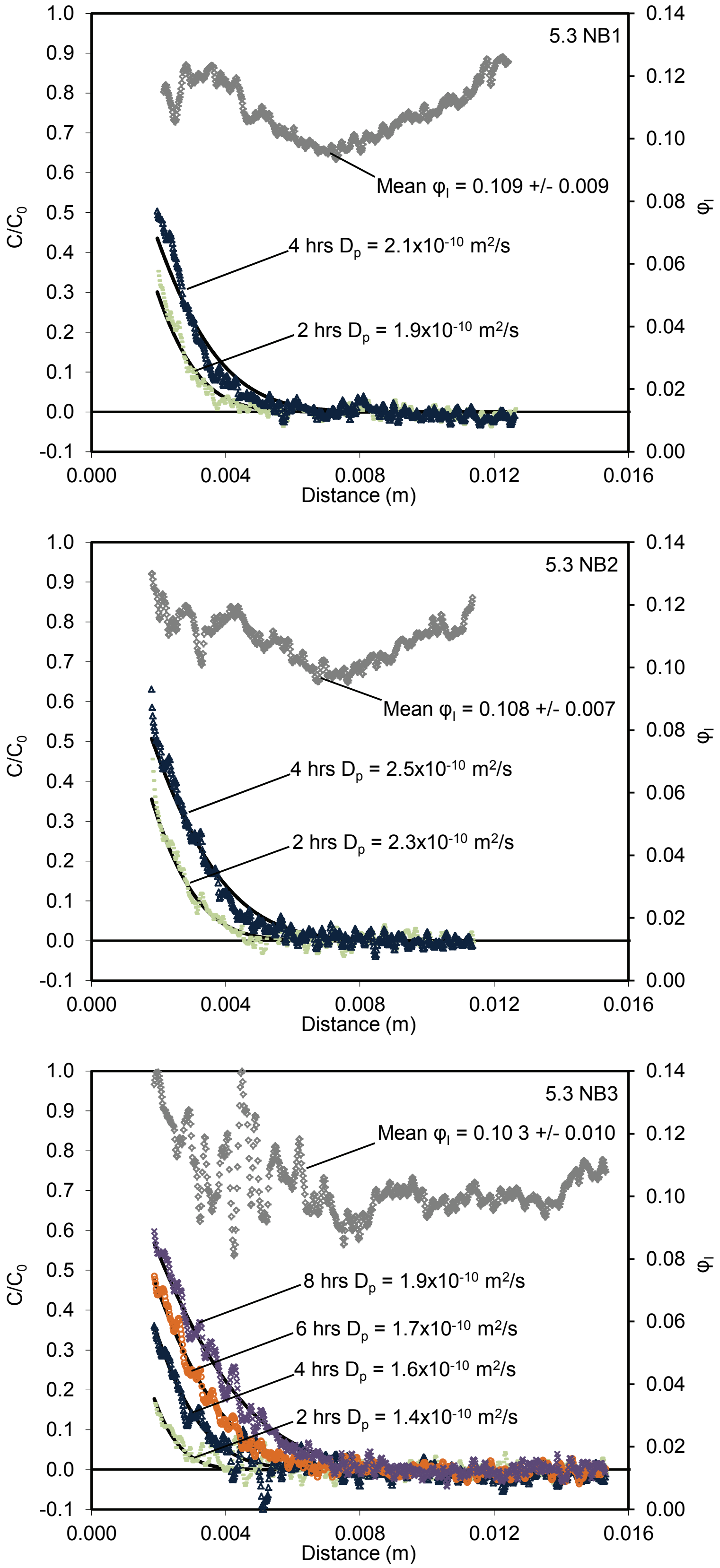

Figure B 1: D_{pl} and ϕ_l profiles for Opalinus Clay BDR1 5.3 NB samples

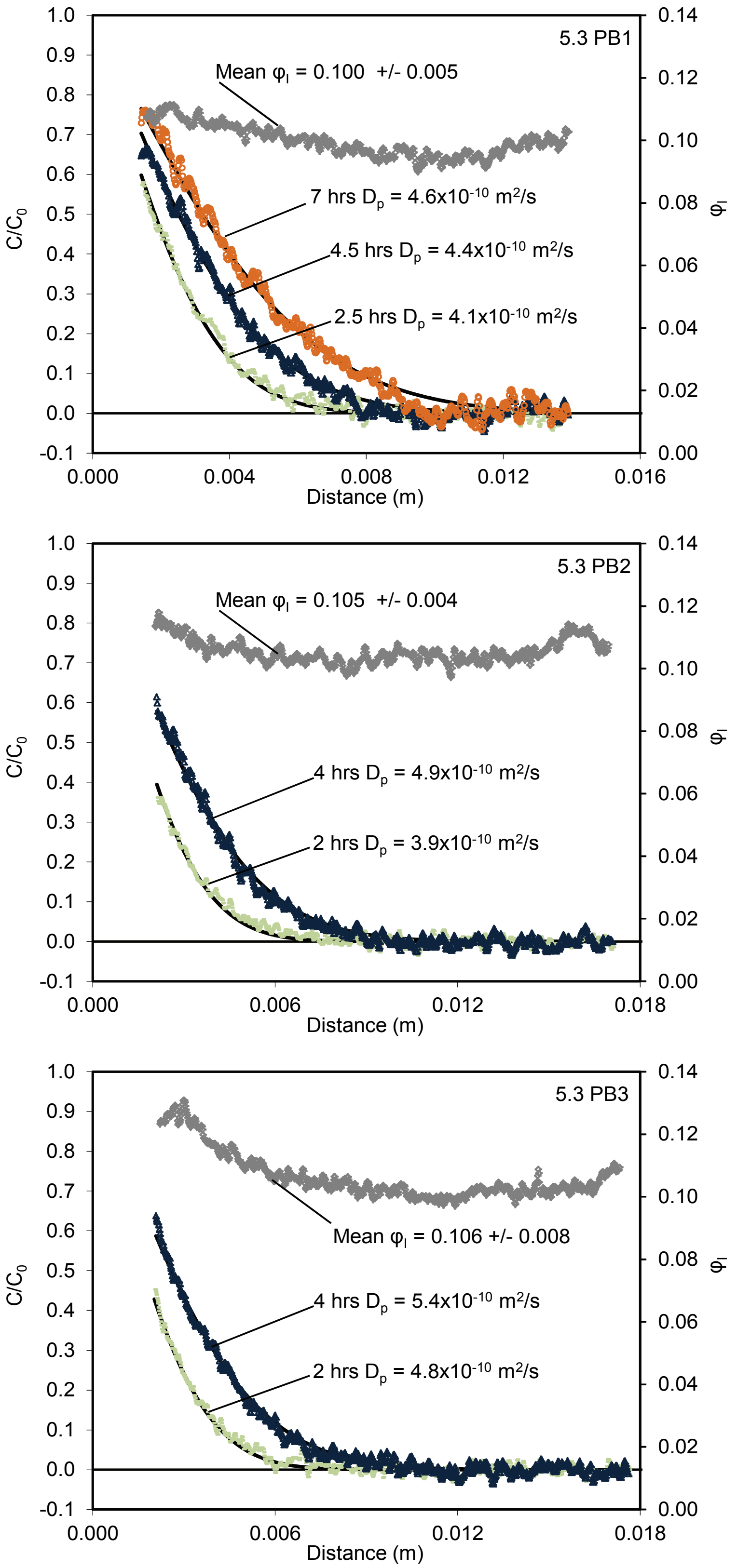

Figure B 2: D_{pl} and ϕ_l profiles for Opalinus Clay BDR1 5.3 PB samples

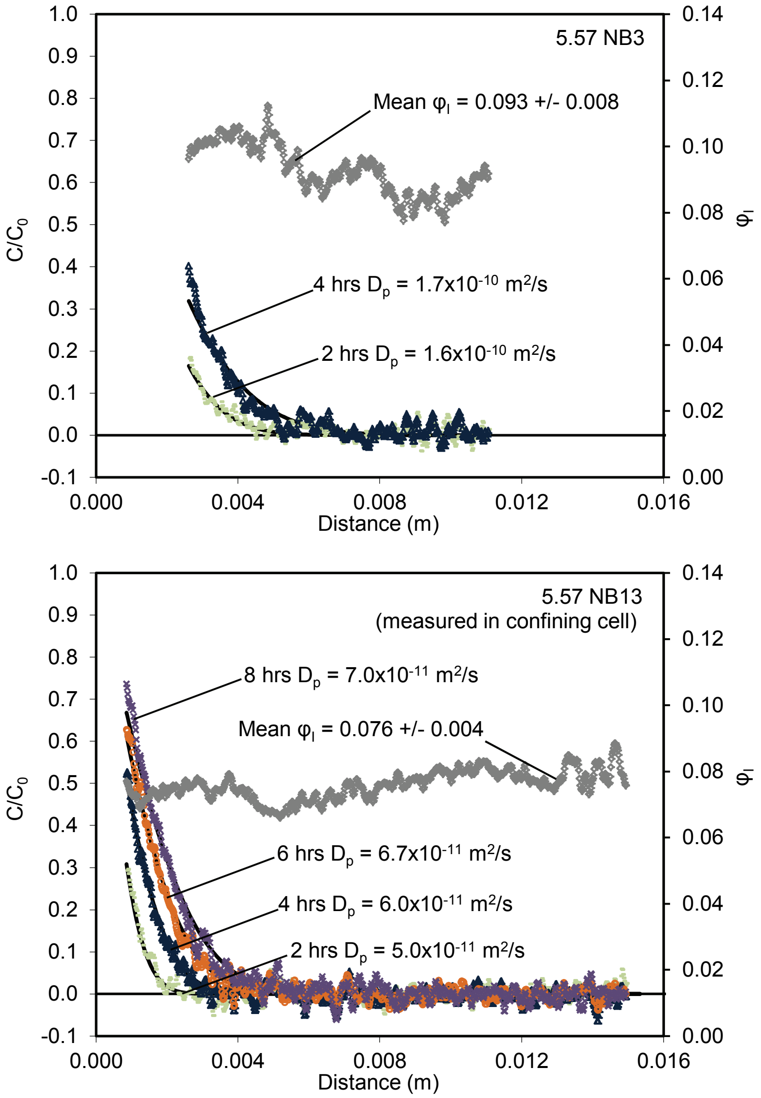

Figure B 3: D_{pl} and ϕ_l profiles for Opalinus Clay BDR1 5.57 NB samples measured with and without confining pressure

APPENDIX C: EXAMPLES OF REACTIVE TRANSPORT FILES

CONTENTS

Example of a MIN3P Template File (5.57 PB8, C_0 = 0.01 M Cs^+)

```
ptf %
!  Test example: Cs+ cation exchange in OPA SPW
!
! Data Block 1: global control parameters
! -------------------------------------------------------------------------
!
'global control parameters'
'Degassing from landfill plume'
.true.                        ;varsat_flow
.false.                       ;steady_flow
.true.                        ;fully_saturated
.true.                        ;reactive_transport

'done'

! Data Block 2: geochemical system
! -------------------------------------------------------------------------
'geochemical system'

'use new database format'


!'use pitzer model'

!'use macinnes convention'

'database directory'
'database\default'

'components'
8                           ;number of components (nc-1)
'h+1'
'cs+1'                        ;component names
'na+1'
'k+1'
'mg+2'
'ca+2'
'cl-1'
'so4-2'

'intra-aqueous kinetic reactions'
0                            ;number of intra-aqueous kinetic reactions

'secondary aqueous species'
3                 ;number of secondary aqueous species
'oh-'
'hso4-'
'mgoh+'

'gases'
0                            ;number of gases


'sorbed species'
5
'na-x(na)'
'k-x(na)'
'cs-x(na)'
'ca-x(na)'
'mg-x(na)'
```

```
'minerals'
0                              ;number of minerals (nm)

'excluded minerals'
0                              ;number of excluded minerals (nmx)


'done'

! Data Block 3: spatial discretization
! -----------------------------------------------------------------------
'spatial discretization'
1                              ;number of discretization intervals in x
40                              ;number of control volumes in x
0.0 1.6812d-2                ;xmin,xmax
!-----------------------------------------------------------------------
1                              ;number of discretization intervals in z
1                              ;number of control volumes in z
0.0 1.0d0                   ;zmin,zmax
!------------------------------------------------------------------------
1                              ;number of discretization intervals in y
1                              ;number of control volumes in y
0.0 1.0d0
!-----------------------------------------------------------------------
'done'

! Data Block 4: time step control - global system
! -----------------------------------------------------------------------
'time step control - global system'
'days'                         ;time unit
0.0                             ;time at start of solution
4.0d0                          ;final solution time
0.25d0                         ;maximum time step
0.00001d0                      ;minimum time step
'done'

! Data Block 5: control parameters - local geochemistry
! -----------------------------------------------------------------------

'control parameters - local geochemistry'

'newton iteration settings'
1.d-4                          ;factor for numerical differentiation
1.d-6                          ;convergence tolerance

'maximum ionic strength'
20.0d0                         ;max. ionic strength

'minimum activity for h2o'
0.2d0                          ;min. activity for h2o

'done'

! Data Block 6: control parameters - variably saturated flow
! -----------------------------------------------------------------------
!
'control parameters - variably saturated flow'

'mass balance'
```

```
'input units for boundary and initial conditions'
'hydraulic head'             ;input unit

'solver settings'
0                          ;level_vs, incomplete factorization level
100                          ;msolvit_vs, max. number of solver iterations
0                          ;idetail_vs, solver information level
1.0d-7                        ;restol_vs, solver residual tolerance
1.0d-7                        ;deltol_vs, solver update tolerance

'done'


!
! Data Block 7: control parameters - reactive transport
! --------------------------------------------------------------------------
!
'control parameters - reactive transport'

'mass balance'

'spatial weighting'
'upstream'                   ;spatial weighting

'activity update settings'
'double_update'                ;type of activity update

'tortuosity correction'
!'no correction'
'assigned tau'                ;tortuosity is specified below with porosity

'newton iteration settings'
1.0d-4                        ;increment h for numerical differentiation
5                          ;anticipated number of Newton iterations
50                          ;max. number of Newton iterations
1.0d0                        ;anticipated update in log cycles
2.0d0                        ;maximum update in log cycles
1.0d-5                        ;convergence tolerance (global system)

'solver settings'
1                          ;incomplete factorization level
100                          ;max. number of solver iterations
0                          ;solver information level
1.d-7                        ;solver residual tolerance
1.d-7                        ;solver update tolerance

'done'
!
! Data Block 8: output control
! --------------------------------------------------------------------------
!
'output control'

'output of spatial data'
4                          ;number of output times (spatial data)
1.0d0 2.0d0 3.0d0 4.0d0

'output of transient data'
0                          ;number of output locations (transient data)
1                          ;timesteps between output (transient data)
10                          ;control volume numbers (transient data)
```

```
'done'

! Data Block 9: Physical Parameters (Porous Medium)
! ---------------------------------------------------------------------------

'physical parameters - porous medium'
1                              ;number of property zones
! ---------------------------------------------------------------------------
'number and name of zone'
1
'domain'
0.164d0                        ;porosity
1.0d0                   ;tortuosity (calculated from DpCs and D0)

'extent of zone'
0.0 1.6812d-2    0.0 1.0d0 0.0 1.0d0

'end of zone'


'done'

!
! Data Block 10: physical parameters - variably saturated flow
! ---------------------------------------------------------------------------
!
'physical parameters - variably saturated flow'
! ---------------------------------------------------------------------------
! ---------------------------------------------------------------------------
'domain'                ;name of zone


 'hydraulic conductivity in x-direction'
1.0

 'hydraulic conductivity in y-direction'
1.0

 'hydraulic conductivity in z-direction'
1.0

'specific storage coefficient'
 1.0d-6


'end of zone'

'done'


!
! Data Block 11: physical parameters - reactive transport
! ---------------------------------------------------------------------------
!
'physical parameters - reactive transport'

'diffusion coefficients'
%DpCs_557pb8%               ;aqueous phase (Cs Free solution D0 = 2.05e-9;
!                          Li and Gregory, 1974; in Melkior et al 2005,Applied Clay Science 29, 172– 186.
0.d0                    ;gaseous phase

! ---------------------------------------------------------------------------
```

```
'domain'

'longitudinal dispersivity'
0.0d0

'transverse vertical dispersivity'
0.0d0

'transverse horizontal dispersivity'
0.0d0


'end of zone'

'done'
!
! Data Block 12: initial condition - variably saturated flow
! ---------------------------------------------------------------------------
!
'initial condition - variably saturated flow'
1                          ;number of zones
! ---------------------------------------------------------------------------
'number and name of zone'
1
'domain'

'initial condition'
0.00d0                     ;hydraulic head

'extent of zone'
0.0 1.6812d-2   0.0 1.0d0 0.0 1.0d0

'end of zone'


'done'


!
! Data Block 13: boundary conditions - variably saturated flow
! ---------------------------------------------------------------------------
!
'boundary conditions - variably saturated flow'
2                          ;number of zones

! ---------------------------------------------------------------------------
'number and name of zone'
1
'boundary 1'

'boundary type'
'first'     0.0d0          ;hydraulic head

'extent of zone'
0.0 0.0d0   0.0 1.0d0 0.0 1.0d0

'end of zone'

! ---------------------------------------------------------------------------
'number and name of zone'
2
'boundary 2'
```

```
'boundary type'
'first'   0.0d0             ;hydraulic head

'extent of zone'
1.6812d-2 1.6812d-2    0.0 1.0d0 0.0d0 1.0d0

'end of zone'


'done'
!
! Data Block 15: initial conditions - reactive transport
! -------------------------------------------------------------------------
!
'initial condition - reactive transport'
1                          ;number of zones
! -------------------------------------------------------------------------
'number and name of zone'
1
'domain'

'concentration input'                                  ;OPA SPW
7.2d0       'ph'              ;h+1
1.0d-20     'free'            ;cs+1
2.4d-1      'free'            ;na+1
1.61d-3     'free'            ;k+1
1.70d-2     'free'            ;mg+2
2.58d-2     'free'            ;ca+2
2.99d-1     'free'            ;cl-1
1.41d-2     'free'            ;so4-2


'sorption parameter input'
12.4              ;cation exchange capacity [meq/100 g solid]
2.25d0                    ;dry bulk density [g/cm^3] T. Gimmi pers. com. 2011

'equilibrate with fixed solution composition'

'extent of zone'
0.0 1.6812d-2    0.0d0 1.0d0 0.0 1.0d0

'end of zone'



'done'

 Data Block 16: boundary conditions - reactive transport
! -------------------------------------------------------------------------
!
'boundary conditions - reactive transport'
1                          ;number of zones

! -------------------------------------------------------------------------
'number and name of zone'
1
'inflow boundary'

'boundary type'
'first'
```

```
'concentration input'                    ;OPA Cs Tracer 1
7.2d0      'ph'              ;h+1
1.0d-2     'free'            ;cs+1
2.4d-1     'free'            ;na+1
1.61d-3    'free'            ;k+1
1.70d-2    'free'            ;mg+2
2.58d-2    'free'            ;ca+2
3.09d-1    'free'            ;cl-1
1.41d-2    'free'            ;so4-2

'sorption parameter input'
12.4                ;cation exchange capacity
2.25d0                   ;dry bulk density  T. Gimmi pers. com. 2011

'extent of zone'
0.0d0 0.0d0    0.0 1.0d0 0.0 1.0d0

'end of zone'

'done'
```

Example of a PEST Control File (5.57 PB8, C_0 = 0.01 M Cs^+)

```
pcf
* control data
restart  estimation
   2   144    2    0    1
   2    4 single point   1   0   0
  5.0   2.0   0.3  0.01    10
  3.0   3.0 0.001
  0.1
   20  0.005    4    3  0.01    3
   1    1    1
* parameter groups
k_557pb8       relative 0.01  0.0  switch  2.0 parabolic
DpCs_557pb8    relative 0.01  0.0  switch  2.0 parabolic
* parameter data
k_557pb8       log  factor     2.000      5.000000E-1   1.000000E+1    k_557pb8         1.0000       0.0000     1
DpCs_557pb8    log  factor     9.7e-10      1.000000e-12  2.000000E-9    DpCs_557pb8      1.0000       0.0000     1
* observation groups
obsgroup
* observation data
cs_1             0.162470   1.0  obsgroup
cs_2             0.112512   1.0  obsgroup
cs_3             0.073664   1.0  obsgroup
cs_4             0.044489   1.0  obsgroup
cs_5             0.023513   1.0  obsgroup
cs_6             0.009278   1.0  obsgroup
cs_7             0.000399   1.0  obsgroup
cs_8             0.000000   1.0  obsgroup
cs_9             0.000000   1.0  obsgroup
cs_10             0.000000   1.0  obsgroup
cs_11             0.000000   1.0  obsgroup
cs_12             0.000000   1.0  obsgroup
cs_13             0.000000   1.0  obsgroup
cs_14             0.000000   1.0  obsgroup
cs_15             0.000000   1.0  obsgroup
cs_16             0.000000   1.0  obsgroup
cs_17             0.000000   1.0  obsgroup
cs_18             0.000000   1.0  obsgroup
cs_19             0.000000   1.0  obsgroup
cs_20             0.000000   1.0  obsgroup
cs_21             0.000000   1.0  obsgroup
cs_22             0.000000   1.0  obsgroup
cs_23             0.000000   1.0  obsgroup
cs_24             0.000000   1.0  obsgroup
cs_25             0.000000   1.0  obsgroup
cs_26             0.000000   1.0  obsgroup
cs_27             0.000000   1.0  obsgroup
cs_28             0.000000   1.0  obsgroup
cs_29             0.000000   1.0  obsgroup
cs_30             0.000000   1.0  obsgroup
cs_31             0.000000   1.0  obsgroup
cs_32             0.000000   1.0  obsgroup
cs_33             0.000000   1.0  obsgroup
cs_34             0.000000   1.0  obsgroup
cs_35             0.000000   1.0  obsgroup
cs_36             0.000000   1.0  obsgroup
cs_37             0.284050   1.0  obsgroup
cs_38             0.242505   1.0  obsgroup
cs_39             0.197868   1.0  obsgroup
cs_40             0.154296  1.0  obsgroup
cs_41             0.114518  1.0  obsgroup
```

```
cs_42          0.080134  1.0  obsgroup
cs_43          0.051867  1.0  obsgroup
cs_44          0.029786  1.0  obsgroup
cs_45          0.013497  1.0  obsgroup
cs_46          0.002303  1.0  obsgroup
cs_47          0.000000  1.0  obsgroup
cs_48          0.000000  1.0  obsgroup
cs_49          0.000000  1.0  obsgroup
cs_50          0.000000  1.0  obsgroup
cs_51          0.000000  1.0  obsgroup
cs_52          0.000000  1.0  obsgroup
cs_53          0.000000  1.0  obsgroup
cs_54          0.000000  1.0  obsgroup
cs_55          0.000000  1.0  obsgroup
cs_56          0.000000  1.0  obsgroup
cs_57          0.000000  1.0  obsgroup
cs_58          0.000000  1.0  obsgroup
cs_59          0.000000  1.0  obsgroup
cs_60          0.000000  1.0  obsgroup
cs_61          0.000000  1.0  obsgroup
cs_62          0.000000  1.0  obsgroup
cs_63          0.000000  1.0  obsgroup
cs_64          0.000000  1.0  obsgroup
cs_65          0.000000  1.0  obsgroup
cs_66          0.000000  1.0  obsgroup
cs_67          0.000000  1.0  obsgroup
cs_68          0.000000  1.0  obsgroup
cs_69          0.000000  1.0  obsgroup
cs_70          0.000000  1.0  obsgroup
cs_71          0.000000  1.0  obsgroup
cs_72          0.000000  1.0  obsgroup
cs_73          0.373132  1.0  obsgroup
cs_74          0.331729  1.0  obsgroup
cs_75          0.288046  1.0  obsgroup
cs_76          0.244375  1.0  obsgroup
cs_77          0.202462  1.0  obsgroup
cs_78          0.163577  1.0  obsgroup
cs_79          0.128578  1.0  obsgroup
cs_80          0.097972  1.0  obsgroup
cs_81          0.071970  1.0  obsgroup
cs_82          0.050544  1.0  obsgroup
cs_83          0.033477  1.0  obsgroup
cs_84          0.020405  1.0  obsgroup
cs_85          0.010864  1.0  obsgroup
cs_86          0.004329  1.0  obsgroup
cs_87          0.000245  1.0  obsgroup
cs_88          0.000000  1.0  obsgroup
cs_89          0.000000  1.0  obsgroup
cs_90          0.000000  1.0  obsgroup
cs_91          0.000000  1.0  obsgroup
cs_92          0.000000  1.0  obsgroup
cs_93          0.000000  1.0  obsgroup
cs_94          0.000000  1.0  obsgroup
cs_95          0.000000  1.0  obsgroup
cs_96          0.000000  1.0  obsgroup
cs_97          0.000000  1.0  obsgroup
cs_98          0.000000  1.0  obsgroup
cs_99          0.000000  1.0  obsgroup
cs_100          0.000000  1.0  obsgroup
cs_101          0.000000  1.0  obsgroup
cs_102          0.000000  1.0  obsgroup
cs_103          0.000000  1.0  obsgroup
```

```
cs_104          0.000000  1.0  obsgroup
cs_105          0.000000  1.0  obsgroup
cs_106          0.000000  1.0  obsgroup
cs_107          0.000000  1.0  obsgroup
cs_108          0.000000  1.0  obsgroup
cs_109          0.421924  1.0  obsgroup
cs_110          0.388013  1.0  obsgroup
cs_111          0.350046  1.0  obsgroup
cs_112          0.310111  1.0  obsgroup
cs_113          0.269915  1.0  obsgroup
cs_114          0.230815  1.0  obsgroup
cs_115          0.193851  1.0  obsgroup
cs_116          0.159780  1.0  obsgroup
cs_117          0.129106  1.0  obsgroup
cs_118          0.102112  1.0  obsgroup
cs_119          0.078895  1.0  obsgroup
cs_120          0.059396  1.0  obsgroup
cs_121          0.043429  1.0  obsgroup
cs_122          0.030713  1.0  obsgroup
cs_123          0.020895  1.0  obsgroup
cs_124          0.013583  1.0  obsgroup
cs_125          0.008362  1.0  obsgroup
cs_126          0.004821  1.0  obsgroup
cs_127          0.002569  1.0  obsgroup
cs_128          0.001251  1.0  obsgroup
cs_129          0.000562  1.0  obsgroup
cs_130          0.000254  1.0  obsgroup
cs_131          0.000144  1.0  obsgroup
cs_132          0.000111  1.0  obsgroup
cs_133          0.000098  1.0  obsgroup
cs_134          0.000000  1.0  obsgroup
cs_135          0.000000  1.0  obsgroup
cs_136          0.000000  1.0  obsgroup
cs_137          0.000000  1.0  obsgroup
cs_138          0.000000  1.0  obsgroup
cs_139          0.000000  1.0  obsgroup
cs_140          0.000000  1.0  obsgroup
cs_141          0.000000  1.0  obsgroup
cs_142          0.000000  1.0  obsgroup
cs_143          0.000000  1.0  obsgroup
cs_144          0.000000  1.0  obsgroup
* model command line
min3p_32
* model input/output
557pb8.tpl  557pb8.dat
database\default\sorption.tpl database\default\sorption.dbs
557pb8_1.ins  557pb8_1.gst_gsb
557pb8_2.ins  557pb8_2.gst_gsb
557pb8_3.ins  557pb8_3.gst_gsb
557pb8_4.ins  557pb8_4.gst_gsb
* prior information
```

Example of a PEST Record File (5.57 PB8, C_0 = 0.01 M Cs^+)

```
PEST RUN RECORD: CASE 557pb8

PEST run mode:-

  Parameter estimation mode


Case dimensions:-

  Number of parameters                 :    2
  Number of adjustable parameters      :    2
  Number of parameter groups           :    2
  Number of observations               :  144
  Number of prior estimates            :    0


Model command line(s):-

  min3p_32


Jacobian command line:-

  na


Model interface files:-

  Templates:
    557pb8.tpl
    database\default\sorption.tpl
  for model input files:
    557pb8.dat
    database\default\sorption.dbs

  (Parameter values written using single precision protocol.)
  (Decimal point always included.)

  Instruction files:
    557pb8_1.ins
    557pb8_2.ins
    557pb8_3.ins
    557pb8_4.ins
  for reading model output files:
    557pb8_1.gst_gsb
    557pb8_2.gst_gsb
    557pb8_3.gst_gsb
    557pb8_4.gst_gsb


PEST-to-model message file:-

  na


Derivatives calculation:-

Param       Increment   Increment   Increment   Forward or   Multiplier  Method
group       type        low bound   central     (central)    (central)
k_557pb8    relative    1.0000E-02  none        switch       2.000       parabolic
```

```
dpcs_557pb8  relative   1.0000E-02   none       switch      2.000     parabolic


Parameter definitions:-

Name        Trans-         Change      Initial       Lower         Upper
        formation        limit        value          bound          bound
k_557pb8     log            factor      2.00000      0.500000       10.0000
dpcs_557pb8  log            factor     9.700000E-10   1.000000E-12   2.000000E-09

Name        Group         Scale        Offset       Model command number
k_557pb8     k_557pb8      1.00000        0.00000            1
dpcs_557pb8  dpcs_557pb8   1.00000        0.00000            1


Prior information:-

   No prior information supplied


Observations:-

Observation name       Observation                   Weight      Group
 cs_1                       0.162470                    1.000       obsgroup
 cs_2                       0.112512                    1.000       obsgroup
 cs_3                       7.366400E-02                1.000       obsgroup
 cs_4                       4.448900E-02      1.000      obsgroup
 cs_5                       2.351300E-02      1.000      obsgroup
 cs_6                       9.278000E-03      1.000      obsgroup
 cs_7                       3.990000E-04      1.000      obsgroup
 cs_8                       0.00000                     1.000       obsgroup
 cs_9                       0.00000                     1.000       obsgroup
 cs_10                      0.00000                     1.000       obsgroup
 cs_11                      0.00000                     1.000       obsgroup
 cs_12                      0.00000                     1.000       obsgroup
 cs_13                      0.00000                     1.000       obsgroup
 cs_14                      0.00000                     1.000       obsgroup
 cs_15                      0.00000                     1.000       obsgroup
 cs_16                      0.00000                     1.000       obsgroup
 cs_17                      0.00000                     1.000       obsgroup
 cs_18                      0.00000                     1.000       obsgroup
 cs_19                      0.00000                     1.000       obsgroup
 cs_20                      0.00000                     1.000       obsgroup
 cs_21                      0.00000                     1.000       obsgroup
 cs_22                      0.00000                     1.000       obsgroup
 cs_23                      0.00000                     1.000       obsgroup
 cs_24                      0.00000                     1.000       obsgroup
 cs_25                      0.00000                     1.000       obsgroup
 cs_26                      0.00000                     1.000       obsgroup
 cs_27                      0.00000                     1.000       obsgroup
 cs_28                      0.00000                     1.000       obsgroup
 cs_29                      0.00000                     1.000       obsgroup
 cs_30                      0.00000                     1.000       obsgroup
 cs_31                      0.00000                     1.000       obsgroup
 cs_32                      0.00000                     1.000       obsgroup
 cs_33                      0.00000                     1.000       obsgroup
 cs_34                      0.00000                     1.000       obsgroup
 cs_35                      0.00000                     1.000       obsgroup
 cs_36                      0.00000                     1.000       obsgroup
 cs_37                0.284050                  1.000      obsgroup
 cs_38                0.242505                  1.000      obsgroup
 cs_39                0.197868                  1.000      obsgroup
```

```
cs_40          0.154296               1.000    obsgroup
cs_41          0.114518               1.000    obsgroup
cs_42          8.013400E-02    1.000   obsgroup
cs_43          5.186700E-02    1.000   obsgroup
cs_44          2.978600E-02    1.000   obsgroup
cs_45          1.349700E-02    1.000   obsgroup
cs_46          2.303000E-03    1.000   obsgroup
cs_47          0.00000                1.000    obsgroup
cs_48                  0.00000                1.000   obsgroup
cs_49                  0.00000                1.000   obsgroup
cs_50                  0.00000                1.000   obsgroup
cs_51                  0.00000                1.000   obsgroup
cs_52                  0.00000                1.000   obsgroup
cs_53                  0.00000                1.000   obsgroup
cs_54                  0.00000                1.000   obsgroup
cs_55                  0.00000                1.000   obsgroup
cs_56                  0.00000                1.000   obsgroup
cs_57                  0.00000                1.000   obsgroup
cs_58                  0.00000                1.000   obsgroup
cs_59                  0.00000                1.000   obsgroup
cs_60                  0.00000                1.000   obsgroup
cs_61                  0.00000                1.000   obsgroup
cs_62                  0.00000                1.000   obsgroup
cs_63                  0.00000                1.000   obsgroup
cs_64                  0.00000                1.000   obsgroup
cs_65                  0.00000                1.000   obsgroup
cs_66                  0.00000                1.000   obsgroup
cs_67                  0.00000                1.000   obsgroup
cs_68                  0.00000                1.000   obsgroup
cs_69                  0.00000                1.000   obsgroup
cs_70                  0.00000                1.000   obsgroup
cs_71                  0.00000                1.000   obsgroup
cs_72                  0.00000                1.000   obsgroup
cs_73          0.373132               1.000    obsgroup
cs_74          0.331729               1.000    obsgroup
cs_75          0.288046               1.000    obsgroup
cs_76          0.244375               1.000    obsgroup
cs_77          0.202462               1.000    obsgroup
cs_78                  0.163577               1.000   obsgroup
cs_79                  0.128578               1.000   obsgroup
cs_80          9.797200E-02    1.000   obsgroup
cs_81          7.197000E-02    1.000   obsgroup
cs_82          5.054400E-02    1.000   obsgroup
cs_83          3.347700E-02    1.000   obsgroup
cs_84          2.040500E-02    1.000   obsgroup
cs_85          1.086400E-02    1.000   obsgroup
cs_86          4.329000E-03    1.000   obsgroup
cs_87          2.450000E-04    1.000   obsgroup
cs_88                  0.00000                1.000   obsgroup
cs_89                  0.00000                1.000   obsgroup
cs_90                  0.00000                1.000   obsgroup
cs_91                  0.00000                1.000   obsgroup
cs_92                  0.00000                1.000   obsgroup
cs_93                  0.00000                1.000   obsgroup
cs_94                  0.00000                1.000   obsgroup
cs_95                  0.00000                1.000   obsgroup
cs_96                  0.00000                1.000   obsgroup
cs_97                  0.00000                1.000   obsgroup
cs_98                  0.00000                1.000   obsgroup
cs_99                  0.00000                1.000   obsgroup
cs_100                 0.00000                1.000   obsgroup
cs_101                 0.00000                1.000   obsgroup
```

```
 cs_102                  0.00000                 1.000     obsgroup
 cs_103                  0.00000                 1.000     obsgroup
 cs_104                  0.00000                 1.000     obsgroup
 cs_105                  0.00000                 1.000     obsgroup
 cs_106                  0.00000                 1.000     obsgroup
 cs_107                  0.00000                 1.000     obsgroup
 cs_108                  0.00000                 1.000     obsgroup
 cs_109                  0.421924                1.000     obsgroup
 cs_110                  0.388013                1.000     obsgroup
 cs_111                  0.350046                1.000     obsgroup
 cs_112                  0.310111                1.000     obsgroup
 cs_113                  0.269915                1.000     obsgroup
 cs_114                  0.230815                1.000     obsgroup
 cs_115                  0.193851                1.000     obsgroup
 cs_116                  0.159780                1.000     obsgroup
 cs_117                  0.129106                1.000     obsgroup
 cs_118                  0.102112                1.000     obsgroup
 cs_119                  7.889500E-02            1.000     obsgroup
 cs_120                  5.939600E-02    1.000     obsgroup
 cs_121                  4.342900E-02    1.000     obsgroup
 cs_122                  3.071300E-02    1.000     obsgroup
 cs_123                  2.089500E-02    1.000     obsgroup
 cs_124                  1.358300E-02    1.000     obsgroup
 cs_125                  8.362000E-03    1.000     obsgroup
 cs_126          4.821000E-03    1.000     obsgroup
 cs_127                  2.569000E-03    1.000     obsgroup
 cs_128                  1.251000E-03    1.000     obsgroup
 cs_129                  5.620000E-04    1.000     obsgroup
 cs_130                  2.540000E-04    1.000     obsgroup
 cs_131                  1.440000E-04    1.000     obsgroup
 cs_132                  1.110000E-04    1.000     obsgroup
 cs_133                  9.800000E-05    1.000     obsgroup
 cs_134                  0.00000                 1.000     obsgroup
 cs_135                  0.00000                 1.000     obsgroup
 cs_136                  0.00000                 1.000     obsgroup
 cs_137                  0.00000                 1.000     obsgroup
 cs_138                  0.00000                 1.000     obsgroup
 cs_139                  0.00000                 1.000     obsgroup
 cs_140                  0.00000                 1.000     obsgroup
 cs_141                  0.00000                 1.000     obsgroup
 cs_142                  0.00000                 1.000     obsgroup
 cs_143                  0.00000                 1.000     obsgroup
 cs_144                  0.00000                 1.000     obsgroup


Control settings:-

  Initial lambda                                               :  5.0000
  Lambda adjustment factor                                     :  2.0000
  Sufficient new/old phi ratio per optimisation iteration              : 0.30000
  Limiting relative phi reduction between lambdas                      : 1.00000E-02
  Maximum trial lambdas per iteration                          :  10
  Forgive model run failure during lamda testing                       : no

  Perform Broyden's update of Jacobian matrix                      : no

  Maximum  factor  parameter change (factor-limited changes)    :  3.0000
  Maximum relative parameter change (relative-limited changes) : na
  Fraction of initial parameter values used in computing
  change limit for near-zero parameters                        : 1.00000E-03
  Allow bending of parameter upgrade vector                            : no
  Allow parameters to stick to their bounds                            : no
```

```
  Relative phi reduction below which to begin use of
  central derivatives                               : 0.10000
  Iteration at which to first consider derivatives switch      :   1

  Relative phi reduction indicating convergence              : 0.50000E-02
  Number of phi values required within this range             :   4
  Maximum number of consecutive failures to lower phi         :   3
  Minimal relative parameter change indicating convergence     : 0.10000E-01
  Number of consecutive iterations with minimal param change   :   3
  Maximum number of optimisation iterations                   :  20

  Attempt automatic user intervention                        : no

  Attempt reuse of parameter sensitivities                   : no


File saving options: -

  Save best JCO file                                : yes
  Save multiple JCO files                             : no
  Save multiple REI files                            : no
  Save multiple PAR files                             : no


                         OPTIMISATION RECORD


INITIAL CONDITIONS:
  Sum of squared weighted residuals (ie phi) =  0.51047

    Current parameter values
    k_557pb8         2.00000
    dpcs_557pb8     9.700000E-10


OPTIMISATION ITERATION NO.        : 1
  Model calls so far             : 1
  Starting phi for this iteration:  0.51047

     Lambda =   5.0000     ----->
       Phi =  9.24305E-02  (  0.181 of starting phi)

  No more lambdas: phi is less than 0.3000 of starting phi
  Lowest phi this iteration:  9.24305E-02

    Current parameter values                 Previous parameter values
    k_557pb8         1.54675                 k_557pb8         2.00000
    dpcs_557pb8     9.391939E-10            dpcs_557pb8      9.700000E-10
  Maximum   factor change:  1.293     ["k_557pb8"]
  Maximum relative change: 0.2266     ["k_557pb8"]


OPTIMISATION ITERATION NO.        : 2
  Model calls so far             : 4
  Starting phi for this iteration:  9.24305E-02

     Lambda =   2.5000     ----->
       Phi =  4.39783E-02  (  0.476 of starting phi)

     Lambda =   1.2500     ----->
       Phi =  3.74734E-02  (  0.405 of starting phi)
```

```
    Lambda =  0.62500     ----->
      Phi =  3.26835E-02  (  0.354 of starting phi)

    Lambda =  0.31250     ----->
      Phi =  2.98348E-02  (  0.323 of starting phi)

    Lambda =  0.15625     ----->
      Phi =  2.83656E-02  (  0.307 of starting phi)

    Lambda =  7.81250E-02 ----->
      Phi =  2.79106E-02  (  0.302 of starting phi)

    Lambda =  3.90625E-02 ----->
      Phi =  2.74915E-02  (  0.297 of starting phi)

  No more lambdas: phi is less than 0.3000 of starting phi
  Lowest phi this iteration:  2.74915E-02

    Current parameter values                 Previous parameter values
    k_557pb8         1.40204                 k_557pb8         1.54675
    dpcs_557pb8      1.205239E-09            dpcs_557pb8      9.391939E-10
  Maximum   factor change:  1.283     ["dpcs_557pb8"]
  Maximum relative change: 0.2833     ["dpcs_557pb8"]


OPTIMISATION ITERATION NO.        : 3
  Model calls so far              : 13
  Starting phi for this iteration:  2.74915E-02

    Lambda =  1.95313E-02 ----->
      Phi =  2.42189E-02  (  0.881 of starting phi)

    Lambda =  9.76563E-03 ----->
      Phi =  2.41683E-02  (  0.879 of starting phi)

  No more lambdas: relative phi reduction between lambdas less than 0.0100
  Lowest phi this iteration:  2.41683E-02

    Current parameter values                 Previous parameter values
    k_557pb8         1.42686                 k_557pb8         1.40204
    dpcs_557pb8      1.265723E-09            dpcs_557pb8      1.205239E-09
  Maximum   factor change:  1.050     ["dpcs_557pb8"]
  Maximum relative change: 5.0184E-02 ["dpcs_557pb8"]


OPTIMISATION ITERATION NO.        : 4
  Model calls so far              : 17
  Starting phi for this iteration:  2.41683E-02

    Lambda =  4.88281E-03 ----->
      Phi =  2.42698E-02  (  1.004 times starting phi)

    Lambda =  2.44141E-03 ----->
      Phi =  2.42698E-02  (  1.004 times starting phi)

  No more lambdas: relative phi reduction between lambdas less than 0.0100
  Lowest phi this iteration:  2.42698E-02
  Relative phi reduction between optimisation iterations less than 0.1000
  Switch to central derivatives calculation
  (restart from best parameters so far - these achieved at iteration    3)
```

```
    Current parameter values
    k_557pb8        1.42686
    dpcs_557pb8     1.265723E-09


OPTIMISATION ITERATION NO.        : 5
  Model calls so far              : 21
  Starting phi for this iteration:  2.41683E-02

     Lambda =  4.88281E-03 ----->
       Phi =  2.41833E-02  (  1.001 times starting phi)

     Lambda =  2.44141E-03 ----->
       Phi =  2.41833E-02  (  1.001 times starting phi)

     Lambda =  9.76563E-03 ----->
       Phi =  2.41833E-02  (  1.001 times starting phi)

  No more lambdas: phi rising
  Lowest phi this iteration:  2.41833E-02

    Current parameter values                 Previous parameter values
    k_557pb8        1.42898                  k_557pb8        1.42686
    dpcs_557pb8     1.255976E-09             dpcs_557pb8     1.265723E-09
  Maximum   factor change:  1.008     ["dpcs_557pb8"]
  Maximum relative change: 7.7004E-03 ["dpcs_557pb8"]


OPTIMISATION ITERATION NO.        : 6
  Model calls so far              : 28
  Starting phi for this iteration:  2.41833E-02

     Lambda =  4.88281E-03 ----->
       Phi =  2.41831E-02  (  1.000 of starting phi)

     Lambda =  2.44141E-03 ----->
       Phi =  2.41832E-02  (  1.000 of starting phi)

     Lambda =  9.76563E-03 ----->
       Phi =  2.41832E-02  (  1.000 of starting phi)

  No more lambdas: phi rising
  Lowest phi this iteration:  2.41831E-02

    Current parameter values                 Previous parameter values
    k_557pb8        1.42832                  k_557pb8        1.42898
    dpcs_557pb8     1.254552E-09             dpcs_557pb8     1.255976E-09
  Maximum   factor change:  1.001     ["dpcs_557pb8"]
  Maximum relative change: 1.1335E-03 ["dpcs_557pb8"]

  Optimisation complete: the  4 lowest phi's are within a relative distance
                    of eachother of 5.000E-03
  Total model calls:     35

  The model has been run one final time using best parameters.
  Thus all model input files contain best parameter values, and model
  output files contain model results based on these parameters.


                        OPTIMISATION RESULTS
```

```
Parameters ----->

Parameter       Estimated        95% percent confidence limits
               value            lower limit      upper limit
 k_557pb8       1.42686           1.40616          1.44787
 dpcs_557pb8    1.265723E-09      1.226370E-09     1.306337E-09

Note: confidence limits provide only an indication of parameter uncertainty.
     They rely on a linearity assumption which  may not extend as far in
     parameter space as the confidence limits themselves - see PEST manual.

See file 557pb8.sen for parameter sensitivities.


Observations ----->

Observation     Measured             Calculated          Residual            Weight     Group
                  value              value
cs_1              0.162470           0.236351            -7.388130E-02       1.000      obsgroup
cs_2              0.112512           0.163418            -5.090640E-02       1.000      obsgroup
cs_3              7.366400E-02       0.106351            -3.268670E-02       1.000      obsgroup
cs_4              4.448900E-02       6.526257E-02         -2.077357E-02      1.000      obsgroup
cs_5              2.351300E-02       3.789122E-02         -1.437822E-02      1.000      obsgroup
cs_6              9.278000E-03       2.089644E-02         -1.161844E-02      1.000      obsgroup
cs_7              3.990000E-04       1.098806E-02         -1.058906E-02      1.000      obsgroup
cs_8              0.00000            5.527783E-03         -5.527783E-03      1.000      obsgroup
cs_9              0.00000            2.668194E-03         -2.668194E-03      1.000      obsgroup
cs_10             0.00000            1.238781E-03         -1.238781E-03      1.000      obsgroup
cs_11             0.00000            5.543969E-04         -5.543969E-04      1.000      obsgroup
cs_12             0.00000            2.396283E-04         -2.396283E-04      1.000      obsgroup
cs_13             0.00000            1.002117E-04         -1.002117E-04      1.000      obsgroup
cs_14             0.00000            4.061447E-05         -4.061447E-05      1.000      obsgroup
cs_15             0.00000            1.597723E-05         -1.597723E-05      1.000      obsgroup
cs_16             0.00000            6.109681E-06         -6.109681E-06      1.000      obsgroup
cs_17             0.00000            2.274236E-06         -2.274236E-06      1.000      obsgroup
cs_18             0.00000            8.251320E-07         -8.251320E-07      1.000      obsgroup
cs_19             0.00000            2.921606E-07         -2.921606E-07      1.000      obsgroup
cs_20             0.00000            1.010741E-07         -1.010741E-07      1.000      obsgroup
cs_21             0.00000            3.420269E-08         -3.420269E-08      1.000      obsgroup
cs_22             0.00000            1.133280E-08         -1.133280E-08      1.000      obsgroup
cs_23             0.00000            3.680453E-09         -3.680453E-09      1.000      obsgroup
cs_24             0.00000            1.172621E-09         -1.172621E-09      1.000      obsgroup
cs_25             0.00000            3.668519E-10         -3.668519E-10      1.000      obsgroup
cs_26             0.00000            1.127880E-10         -1.127880E-10      1.000      obsgroup
cs_27             0.00000            3.410490E-11         -3.410490E-11      1.000      obsgroup
cs_28             0.00000            1.015027E-11         -1.015027E-11      1.000      obsgroup
cs_29             0.00000            2.975450E-12         -2.975450E-12      1.000      obsgroup
cs_30             0.00000            8.596734E-13         -8.596734E-13      1.000      obsgroup
cs_31             0.00000            2.449613E-13         -2.449613E-13      1.000      obsgroup
cs_32             0.00000            6.888385E-14         -6.888385E-14      1.000      obsgroup
cs_33             0.00000            1.913263E-14         -1.913263E-14      1.000      obsgroup
cs_34             0.00000            5.273356E-15         -5.273356E-15      1.000      obsgroup
cs_35             0.00000            1.524330E-15         -1.524330E-15      1.000      obsgroup
cs_36             0.00000            7.635554E-16         -7.635554E-16      1.000      obsgroup
cs_37             0.284050           0.337686            -5.363630E-02       1.000      obsgroup
cs_38             0.242505           0.274964            -3.245870E-02       1.000      obsgroup
cs_39             0.197868           0.217377            -1.950850E-02       1.000      obsgroup
cs_40             0.154296           0.166666            -1.236990E-02       1.000      obsgroup
cs_41             0.114518           0.123884            -9.365500E-03       1.000      obsgroup
cs_42             8.013400E-02       8.929563E-02        -9.161630E-03       1.000      obsgroup
cs_43             5.186700E-02       6.246430E-02        -1.059730E-02       1.000      obsgroup
cs_44             2.978600E-02       4.245157E-02        -1.266557E-02       1.000      obsgroup
```

```
cs_45          1.349700E-02   2.806455E-02   -1.456755E-02   1.000   obsgroup
cs_46          2.303000E-03   1.807082E-02   -1.576782E-02   1.000   obsgroup
cs_47          0.00000        1.134703E-02   -1.134703E-02   1.000   obsgroup
cs_48          0.00000        6.955972E-03   -6.955972E-03   1.000   obsgroup
cs_49          0.00000        4.167212E-03   -4.167212E-03   1.000   obsgroup
cs_50          0.00000        2.441991E-03   -2.441991E-03   1.000   obsgroup
cs_51          0.00000        1.400927E-03   -1.400927E-03   1.000   obsgroup
cs_52          0.00000        7.873994E-04   -7.873994E-04   1.000   obsgroup
cs_53          0.00000        4.339063E-04   -4.339063E-04   1.000   obsgroup
cs_54          0.00000        2.345935E-04   -2.345935E-04   1.000   obsgroup
cs_55          0.00000        1.245203E-04   -1.245203E-04   1.000   obsgroup
cs_56          0.00000        6.492989E-05   -6.492989E-05   1.000   obsgroup
cs_57          0.00000        3.328100E-05   -3.328100E-05   1.000   obsgroup
cs_58          0.00000        1.677858E-05   -1.677858E-05   1.000   obsgroup
cs_59          0.00000        8.324799E-06   -8.324799E-06   1.000   obsgroup
cs_60          0.00000        4.067220E-06   -4.067220E-06   1.000   obsgroup
cs_61          0.00000        1.957787E-06   -1.957787E-06   1.000   obsgroup
cs_62          0.00000        9.289849E-07   -9.289849E-07   1.000   obsgroup
cs_63          0.00000        4.347623E-07   -4.347623E-07   1.000   obsgroup
cs_64          0.00000        2.007764E-07   -2.007764E-07   1.000   obsgroup
cs_65          0.00000        9.153824E-08   -9.153824E-08   1.000   obsgroup
cs_66          0.00000        4.122233E-08   -4.122233E-08   1.000   obsgroup
cs_67          0.00000        1.834596E-08   -1.834596E-08   1.000   obsgroup
cs_68          0.00000        8.077025E-09   -8.077025E-09   1.000   obsgroup
cs_69          0.00000        3.529988E-09   -3.529988E-09   1.000   obsgroup
cs_70          0.00000        1.558250E-09   -1.558250E-09   1.000   obsgroup
cs_71          0.00000        7.574310E-10   -7.574310E-10   1.000   obsgroup
cs_72          0.00000        5.433164E-10   -5.433164E-10   1.000   obsgroup
cs_73          0.373132       0.385682       -1.254980E-02   1.000   obsgroup
cs_74          0.331729       0.332312       -5.830000E-04   1.000   obsgroup
cs_75          0.288046       0.281043        7.003500E-03   1.000   obsgroup
cs_76          0.244375       0.233063       1.131170E-02    1.000   obsgroup
cs_77          0.202462       0.189386       1.307620E-02    1.000   obsgroup
cs_78          0.163577       0.150739       1.283790E-02    1.000   obsgroup
cs_79          0.128578       0.117511       1.106750E-02    1.000   obsgroup
cs_80          9.797200E-02   8.973949E-02    8.232510E-03   1.000   obsgroup
cs_81          7.197000E-02   6.716191E-02   4.808090E-03    1.000   obsgroup
cs_82          5.054400E-02   4.928734E-02   1.256660E-03    1.000   obsgroup
cs_83          3.347700E-02   3.548936E-02   -2.012360E-03   1.000   obsgroup
cs_84          2.040500E-02   2.509022E-02   -4.685220E-03   1.000   obsgroup
cs_85          1.086400E-02   1.742791E-02   -6.563910E-03   1.000   obsgroup
cs_86          4.329000E-03   1.190146E-02   -7.572460E-03   1.000   obsgroup
cs_87          2.450000E-04   7.995238E-03   -7.750238E-03   1.000   obsgroup
cs_88          0.00000        5.286662E-03   -5.286662E-03   1.000   obsgroup
cs_89          0.00000        3.442510E-03   -3.442510E-03   1.000   obsgroup
cs_90          0.00000        2.208620E-03   -2.208620E-03   1.000   obsgroup
cs_91          0.00000        1.396735E-03   -1.396735E-03   1.000   obsgroup
cs_92          0.00000        8.710409E-04   -8.710409E-04   1.000   obsgroup
cs_93          0.00000        5.358841E-04   -5.358841E-04   1.000   obsgroup
cs_94          0.00000        3.253724E-04   -3.253724E-04   1.000   obsgroup
cs_95          0.00000        1.950441E-04   -1.950441E-04   1.000   obsgroup
cs_96          0.00000        1.154751E-04   -1.154751E-04   1.000   obsgroup
cs_97          0.00000        6.754688E-05   -6.754688E-05   1.000   obsgroup
cs_98          0.00000        3.905159E-05   -3.905159E-05   1.000   obsgroup
cs_99          0.00000        2.232248E-05   -2.232248E-05   1.000   obsgroup
cs_100         0.00000        1.262035E-05   -1.262035E-05   1.000   obsgroup
cs_101         0.00000        7.059783E-06   -7.059783E-06   1.000   obsgroup
cs_102         0.00000        3.909449E-06   -3.909449E-06   1.000   obsgroup
cs_103         0.00000        2.145043E-06   -2.145043E-06   1.000   obsgroup
cs_104         0.00000        1.168974E-06   -1.168974E-06   1.000   obsgroup
cs_105         0.00000        6.377658E-07   -6.377658E-07   1.000   obsgroup
cs_106         0.00000        3.577978E-07   -3.577978E-07   1.000   obsgroup
```

```
cs_107      0.00000        2.238381E-07   -2.238381E-07   1.000   obsgroup
cs_108      0.00000        1.843228E-07   -1.843228E-07   1.000   obsgroup
cs_109      0.421924       0.414693       7.231100E-03    1.000   obsgroup
cs_110      0.388013       0.367890       2.012270E-02    1.000   obsgroup
cs_111      0.350046       0.322037       2.800950E-02    1.000   obsgroup
cs_112      0.310111       0.277939       3.217160E-02    1.000   obsgroup
cs_113      0.269915       0.236363       3.355240E-02    1.000   obsgroup
cs_114      0.230815       0.197965       3.285010E-02    1.000   obsgroup
cs_115      0.193851       0.163250        3.060120E-02   1.000   obsgroup
cs_116      0.159780       0.132533        2.724750E-02   1.000   obsgroup
cs_117      0.129106       0.105929        2.317660E-02   1.000   obsgroup
cs_118      0.102112       8.337076E-02    1.874124E-02   1.000   obsgroup
cs_119      7.889500E-02   6.463056E-02    1.426444E-02   1.000   obsgroup
cs_120      5.939600E-02   4.936802E-02    1.002798E-02   1.000   obsgroup
cs_121      4.342900E-02   3.717176E-02    6.257240E-03   1.000   obsgroup
cs_122      3.071300E-02   2.760104E-02    3.111960E-03   1.000   obsgroup
cs_123      2.089500E-02   2.021939E-02    6.756100E-04   1.000   obsgroup
cs_124      1.358300E-02   1.461915E-02   -1.036150E-03   1.000   obsgroup
cs_125      8.362000E-03   1.043660E-02   -2.074600E-03   1.000   obsgroup
cs_126      4.821000E-03   7.359380E-03   -2.538380E-03   1.000   obsgroup
cs_127      2.569000E-03   5.127667E-03   -2.558667E-03   1.000   obsgroup
cs_128      1.251000E-03   3.531313E-03   -2.280313E-03   1.000   obsgroup
cs_129      5.620000E-04   2.404492E-03   -1.842492E-03   1.000   obsgroup
cs_130      2.540000E-04   1.619222E-03   -1.365222E-03   1.000   obsgroup
cs_131      1.440000E-04   1.078710E-03   -9.347100E-04   1.000   obsgroup
cs_132      1.110000E-04   7.111039E-04   -6.001039E-04   1.000   obsgroup
cs_133      9.800000E-05   4.639840E-04   -3.659840E-04   1.000   obsgroup
cs_134       0.00000       2.997267E-04   -2.997267E-04   1.000   obsgroup
cs_135       0.00000       1.917408E-04   -1.917408E-04   1.000   obsgroup
cs_136       0.00000       1.215065E-04   -1.215065E-04   1.000   obsgroup
cs_137       0.00000       7.630570E-05   -7.630570E-05   1.000   obsgroup
cs_138       0.00000       4.752256E-05   -4.752256E-05   1.000   obsgroup
cs_139       0.00000       2.939923E-05   -2.939923E-05   1.000   obsgroup
cs_140       0.00000       1.814227E-05   -1.814227E-05   1.000   obsgroup
cs_141       0.00000       1.129465E-05   -1.129465E-05   1.000   obsgroup
cs_142       0.00000       7.304445E-06    -7.304445E-06  1.000   obsgroup
cs_143       0.00000       5.238169E-06    -5.238169E-06  1.000   obsgroup
cs_144       0.00000       4.600933E-06    -4.600933E-06  1.000   obsgroup

See file 557pb8.res for more details of residuals in graph-ready format.

See file 557pb8.seo for composite observation sensitivities.


Objective function ----->

  Sum of squared weighted residuals (ie phi)              =  2.4168E-02


Correlation Coefficient ----->

  Correlation coefficient                          =  0.9904


Analysis of residuals ----->

  All residuals:-
     Number of residuals with non-zero weight                    =   144
     Mean value of non-zero weighted residuals                    = -1.0998E-03
     Maximum weighted residual [observation "cs_113"]              =  3.3552E-02
     Minimum weighted residual [observation "cs_1"]              = -7.3881E-02
     Standard variance of weighted residuals                   =  1.7020E-04
```

```
    Standard error of weighted residuals                    =  1.3046E-02

    Note: the above variance was obtained by dividing the objective
    function by the number of system degrees of freedom (ie. number of
    observations with non-zero weight plus number of prior information
    articles with non-zero weight minus the number of adjustable parameters.)
    If the degrees of freedom is negative the divisor becomes
    the number of observations with non-zero weight plus the number of
    prior information items with non-zero weight.


K-L information statistics ----->


  AIC   =  -1245.724
  AICC  =  -1245.552
  BIC   =  -1236.814
  KIC   =  -1233.855

Parameter covariance matrix ----->

               k_557pb8   dpcs_557pb8
k_557pb8       1.0487E-05  -7.8115E-06
dpcs_557pb8   -7.8115E-06   4.8978E-05


Parameter correlation coefficient matrix ----->

               k_557pb8   dpcs_557pb8
k_557pb8        1.000      -0.3447
dpcs_557pb8   -0.3447        1.000


Normalized eigenvectors of parameter covariance matrix ----->

              Vector_1     Vector_2
k_557pb8       0.9815      -0.1916
dpcs_557pb8    0.1916       0.9815


Eigenvalues ----->

8.9622E-06   5.0502E-05
```

APPENDIX D: RADIOGRAPHY DIFFUSION PROFILES FROM CESIUM TRACERS

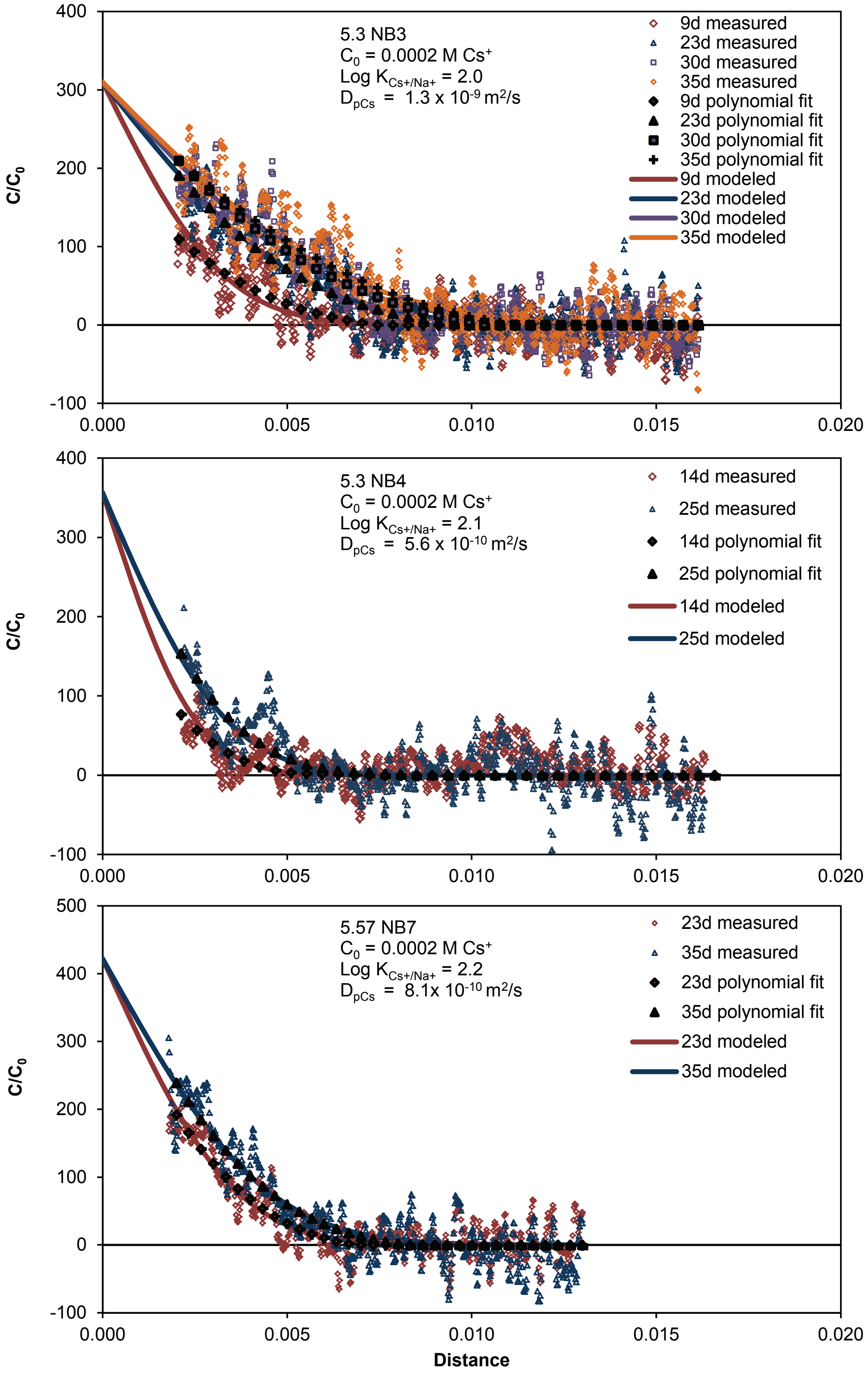

Figure D 1: D_{pCs} raw data profiles, the polynomial fit used for PEST analysis and the fitted profiles for Opalinus Clay BDR1 NB samples; C_0 = 0.0002 M Cs^+

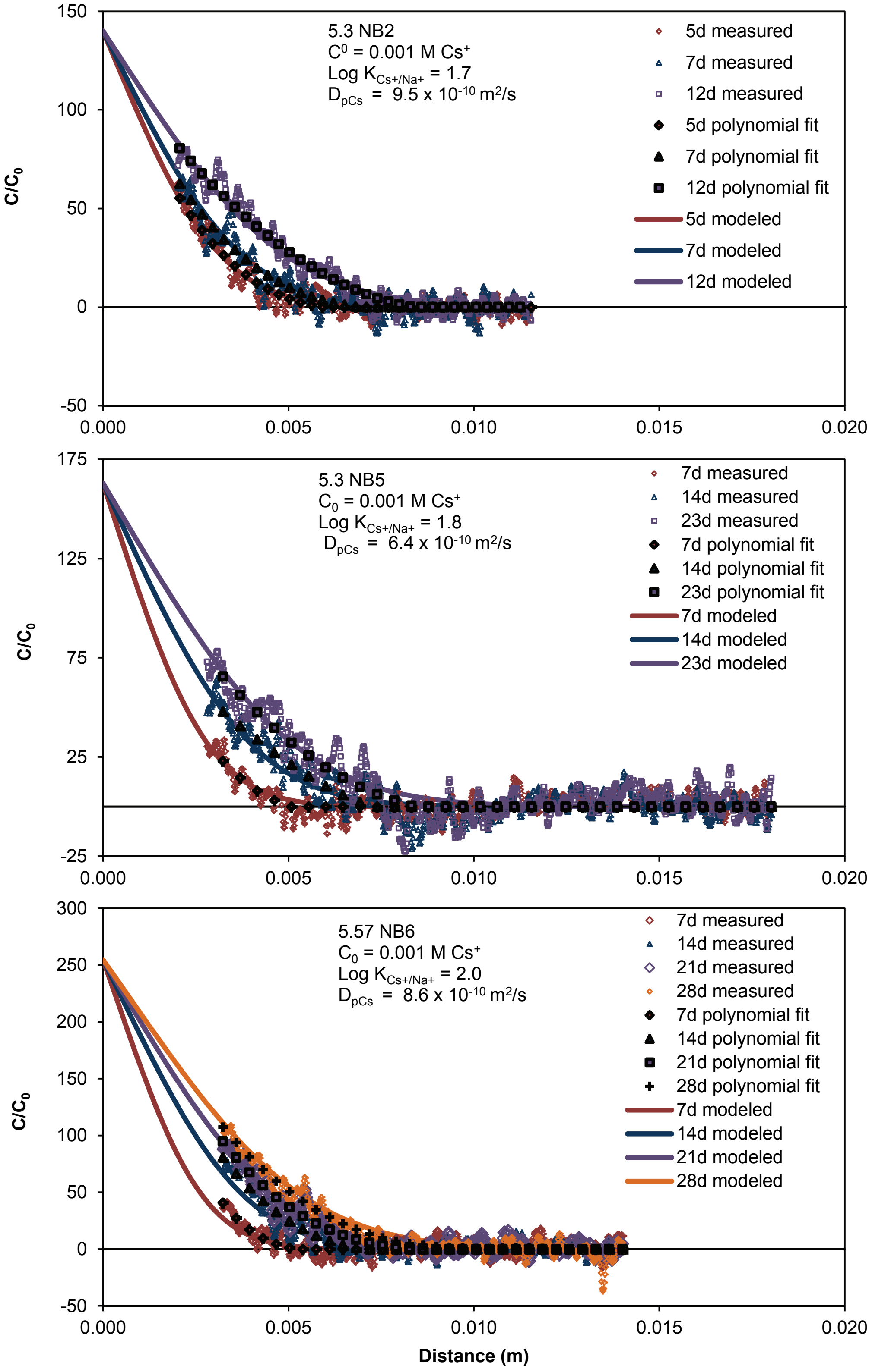

Figure D 2: D_{pCs} raw data profiles, the polynomial fit used for PEST analysis and the fitted profiles for Opalinus Clay BDR1 NB samples; C_0 = 0.001 M Cs^+

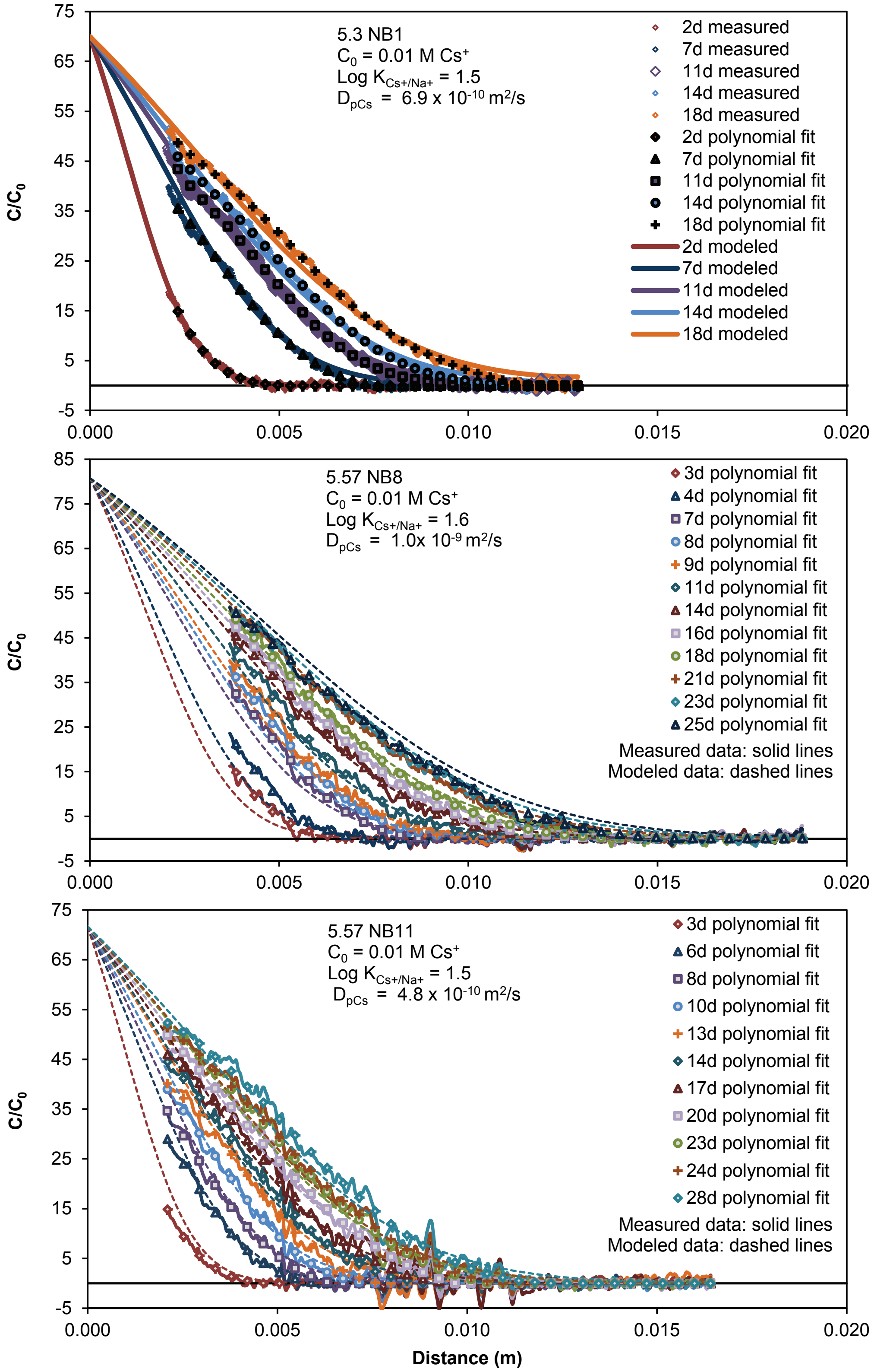

Figure D 3: D_{pCs} raw data profiles, the polynomial fit used for PEST analysis and the fitted profiles for Opalinus Clay BDR1 NB samples; C_0 = 0.01 M Cs^+

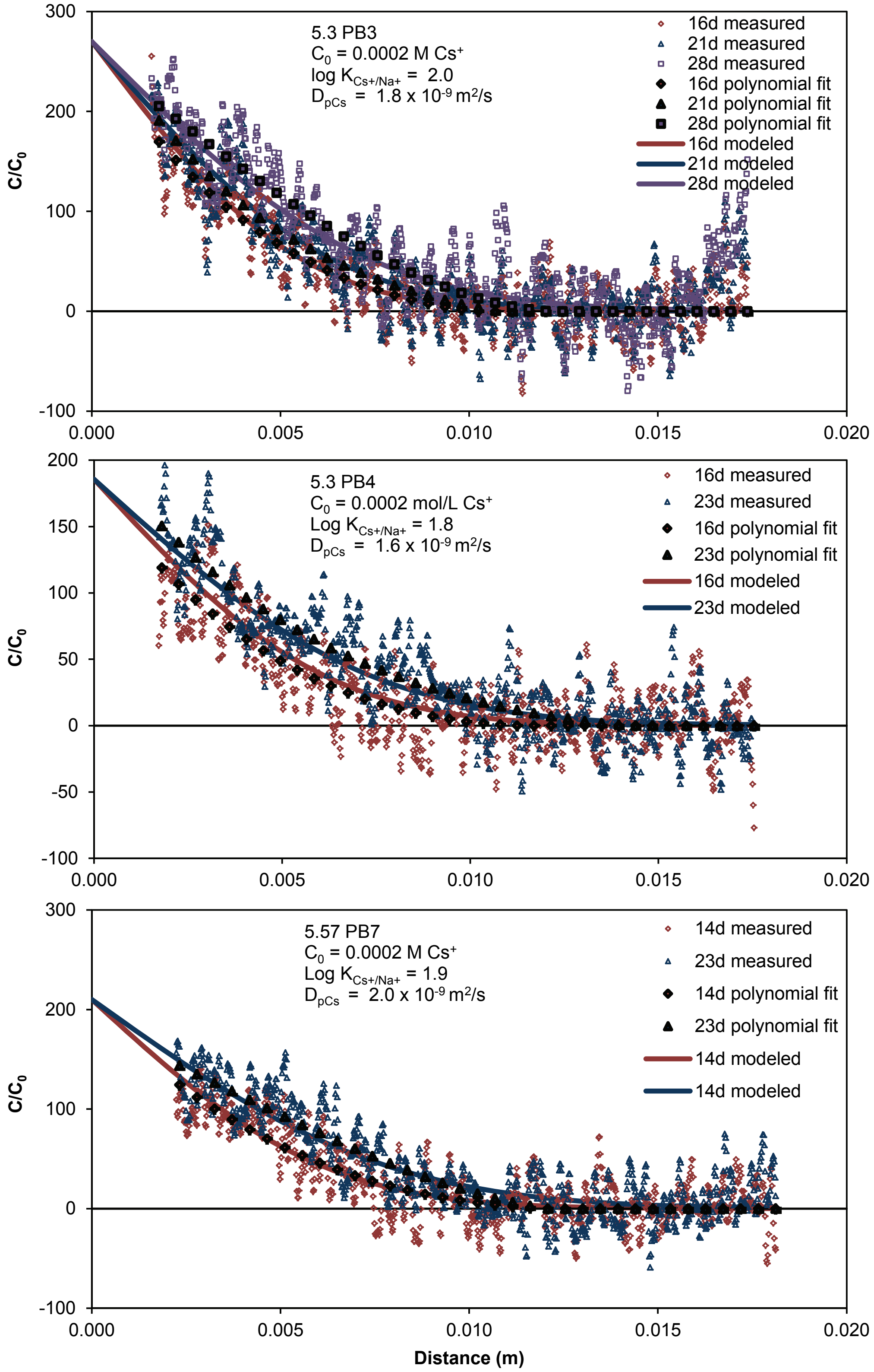

Figure D 4: D_{pCs} raw data profiles, the polynomial fit used for PEST analysis and the fitted profiles for Opalinus Clay BDR1 PB samples; C_0 = 0.0002 M Cs^+

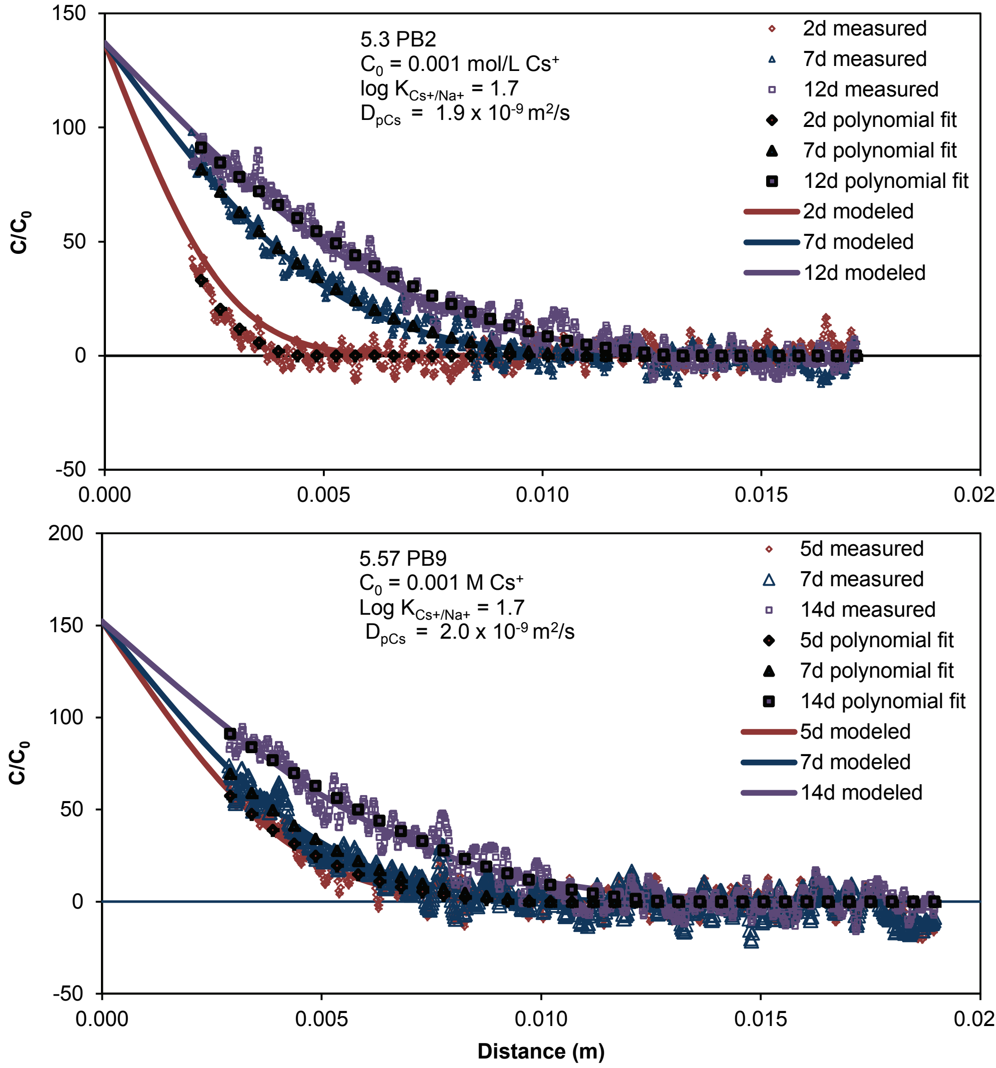

Figure D 5: D_{pCs} raw data profiles, the polynomial fit used for PEST analysis and the fitted profiles for Opalinus Clay BDR1 PB samples; C_0 = 0.001 M Cs^+

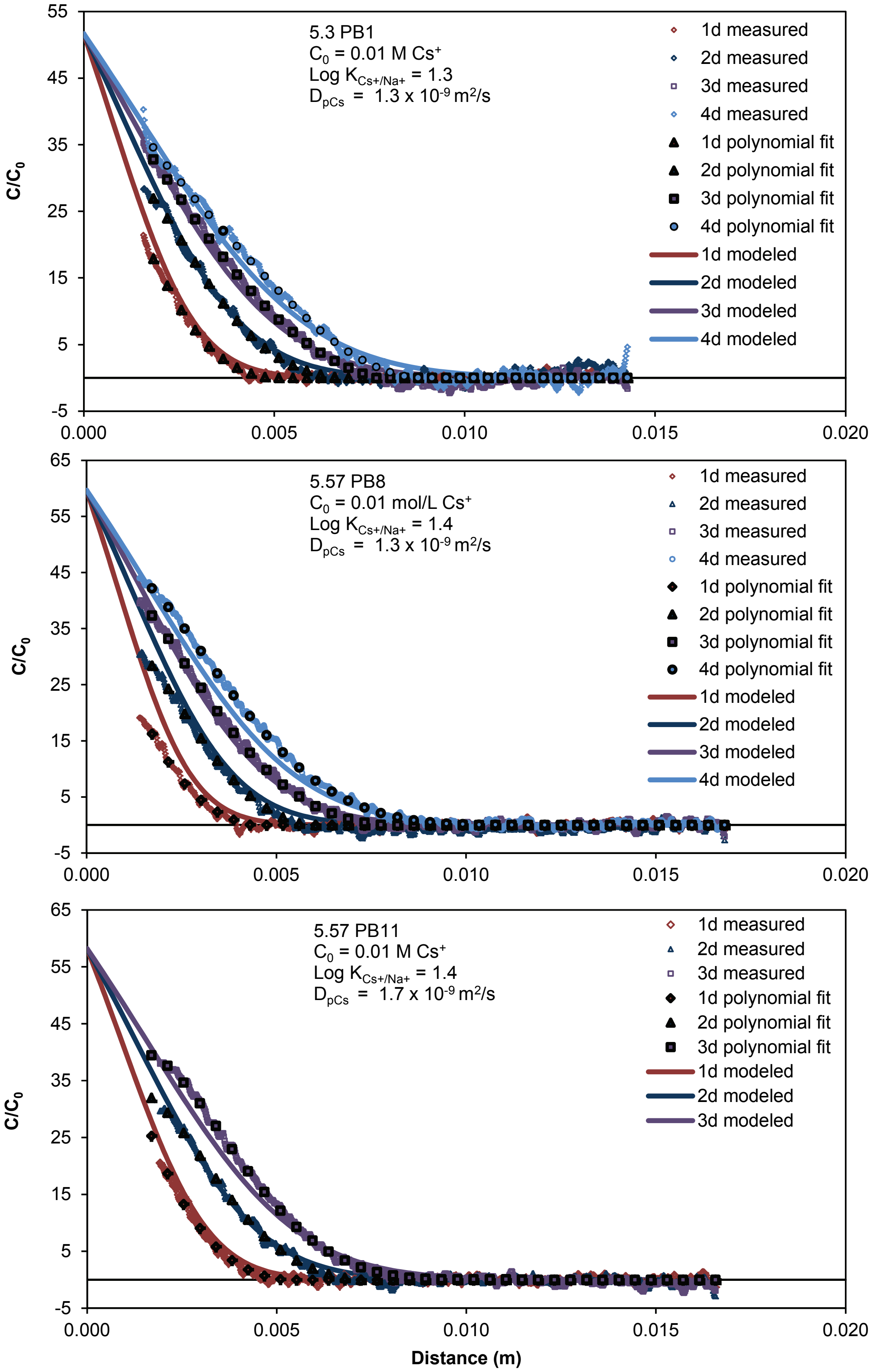

Figure D 6: D_{pCs} raw data profiles, the polynomial fit used for PEST analysis and the fitted profiles for Opalinus Clay BDR1 PB samples; C_0 = 0.01 M Cs^+

APPENDIX E: OVERVIEW OF NANOSCALE IMAGING AND ANALYSIS

There are currently three technologies that are being applied to the study of nanopores: 1) neutron scattering, 2) X-ray microtomography using synchrotron sources, and 3) transmission electron microscopy (TEM). A brief outline of each technology, their potential and their current limitations follows.

Neutron scattering employs neutron radiation to probe a material. It has the potential to provide a wealth of information about a rock sample, including statistically valid information on grain surface and grain/pore distribution properties for length scales ranging from approximately 10 Å to 3 µm. The pores in this size range may often form the connections between the larger pores typically observed petrographically and these pore-throat structures may control many of the resistivity, flow and capillary-pressure characteristics of the rock (Muller and McCauley 1992), making them important to the understanding of transport properties in certain types of rocks. Neutron scattering has been used to analyze the effect of pressure on the pore structure of synthetic fluorohectorite clay samples (Knudsen et al. 2004). While Anovitz et al. (2009) provide a thorough assessment of the potential for quantitative pore structure analysis using ultra-small and small angle neutron scattering (USANS and SANS) in geological media. The current limitations to SANS as described by Anovitz et al. (2009) are summarized here. In SANS, the data are typically interpreted in terms of a two-phase approximation, meaning that with porous media, it is necessary to assume that the area being investigated consists of solid matrix and pore space. This requires that there is relatively little scattering at grain boundaries between different solids. Many geological materials consist of minerals with appreciable mineral-mineral scattering contrast, and as a result, some of the calculated porosity from SANS may reflect intergranular scattering and not pore space. Additionally, the pore-structure data obtained from SANS are limited to the nano and micro pores and do not extend to the macro pores, which leaves out a potentially significant portion of the porosity from the volume calculations. Anovitz et al. (2009) suggest coupling SANS data with backscattered electron imaging in SEM, spin-echo small angle neutron scattering and small angle light scattering to provide more accurate total pore volume calculations. Therefore, the methods for extracting and interpreting the information from the data are still in development and more research, which is undoubtedly occurring, is required before broader application in heterogeneous geologic materials is warranted.

Synchrotron source X-ray microtomography can produce 3D analysis of the pore space and pore connectivity and is increasingly being used for quantitative analysis of pore space. Synchrotron-based microtomography provides a non-destructive, 3D, direct assessment of porosity without the underlying assumptions that are required for pore-geometry investigations with mercury injection porisimetry. To date, the highest spatial resolution achieved is 0.5 µm with sample volumes ranging from 150 to 225 µm^3, using a third-generation synchrotron facility in Japan (Promentilla et al. 2009). Promentilla et al. (2009) concluded that if the critical pore diameter that plays an important role in transport properties is at the nanometer scale, then the current spatial resolution of synchrotron-based microtomography is not sufficient to resolve this issue. However, the theoretical resolution limit of synchrotron-based microtomography has not yet been achieved (Gallucci et al. 2007). Consequently, as technological improvements are made, the resolution may continue to be improved. Therefore, it may be worthwhile to continue to monitor developments in this field.

Transmission electron microscopy is a well-known technique used to visualize nanopores because it has the necessary spatial resolution. It can also provide information on mineral crystallographic orientation and chemical composition. However, samples must be very small and thin such that they are transparent to the electron beam (≤150 nm). It may not be possible to prepare rock samples without disturbing the pore structure. In addition, the small sample size leads to a question of whether the results are representative of the bulk material. Despite these shortcomings, TEM analysis can provide direct information on the size and structure of nanopores, particularly when TEM is used to compliment other methods such as SEM imaging and mercury porisimetry. Figure E 1: Example of an Annular Dark-Field STEM Image of a Shale Sample (not Related to DGR Studies) Prepared Using the FIB Preparation Technique. Arrows are Pointing to Pores; the Measured Dimensions of the Pores are Provided provides an example of an image from the TEM analysis of pores in a shale sample.

Preparation of samples in a manner that will preserve grain/textural relationships, without changing the pore dimensions, is a key step to implementing a TEM study. Focused ion beam (FIB) milling is commonly used for geologic sample preparation (Patterson et al. 2002; Petrunic et al. 2006; Garvie et al. 2008; Hay et al., 2010) because of the capability for precise targeting of selected areas and the wide range of materials that can be prepared. However, the ion collisions that initiate sputter removal can also lead to ion implantation and cause damage to the remaining material, e.g., amorphitization. However, there are techniques available to reduce or remove this damage. Typically, the FIB is operated at an accelerating voltage of 30 kV (Lee et al. 2010). However, FIB columns can now be operated at low accelerating voltages, 1-2 kV, which reduces the size of the amorphitized zone on FIB samples and a low-energy Ar beam can be used to remove damaged layers after FIB milling (Mayer et al. 2007). Alternatively, pre-coating a region of interest with a >85 nm think layer of Au before FIB milling has been found effective in preventing ion-implantation damage (Lee et al. 2007). Overall, the FIB is probably the best technique to prepare samples and keep the original pore geometry preserved.

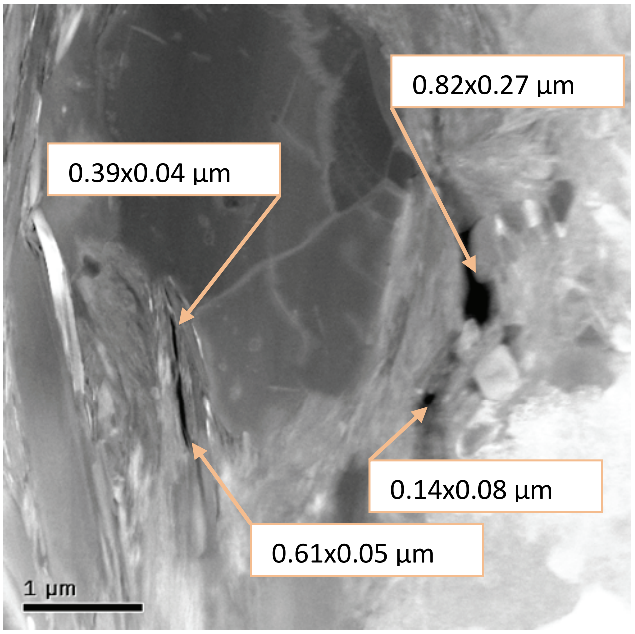

Figure E 1: Example of an Annular Dark-Field STEM Image of a Shale Sample (not Related to DGR Studies) Prepared Using the FIB Preparation Technique. Arrows are Pointing to Pores; the Measured Dimensions of the Pores are Provided

As with the synchrotron technology, 3D imaging in the TEM using electron tomography has been achieved. Most of the 3D imaging to date has focused on synthetic nanoparticles (Ziese et al. 2004; Weyland et al. 2006; Ersen et al. 2007) with one example of magnetite crystals found in bacteria (Weyland et al. 2006). The 3D imaging has been used to successfully image internal pore structure of these materials (Ziese et al. 2004; Ersen et al. 2007). In this review, no examples of 3D TEM studies of porosity imaging from intact rock samples were found in the peer-reviewed literature. Given the additional time, cost and complexity for 3D-TEM analysis, coupled with questions of sample representativeness, this technique is not recommended for porosity characterization at this time.

When considering deep geological repositories, the goal is to be able to understand the structure and connectivity of pores from the nanoscale to the formation scale. Work of this nature is currently underway. The pore structure of low permeability Opalinus Clay is being characterized by using combined X-ray microtomography, SEM and TEM techniques (Holxer et al. 2012; Houben et al. 2012). The goal of this type of work is to use a suite of complementary characterisation methods to provide a complete geostatistical description of the porosity in a potential DGR host rock formation. At this time, peer-reviewed published papers from this work are not available. However, abstracts from recent meetings and conferences are available (Holxer et al. 2012; Houben et al., 2012) and indicate work in this field will progress.

REFERENCES

Anovitz, L.M., G.W. Lynn, D.R. Cole, G. Rother, L.F. Allard, W.A. Hamilton, L. Porcar and M.H. Kim. 2009. A new approach to quantification of metamorphism using ultra-small and small angle neutron scattering. Geochimica et Cosmochimica Acta 73, 7303-7324.

Ersen, O., C. Hirlimann, M. Drillon, J. Werckmann, F. Tihay, C. Pham-Huu, C. Crucifix and P. Schultz. 2007. 3D-TEM characterization of nanometric objects. Solid State Sciences 9, 1088-1098.

Gallucci, E., K. Scrivener, A. Groso, M. Stampanoni and G. Margaritondo. 2007. 3D experimental investigation of the microstructure of cement pastes using synchrotron X-ray microtomography (µCT). Cement and Concrete Research 37, 360-368.

Garvie, L.A.J., D.M. Burt and P.R. Busek. 2008. Nanometer-scale complexity, growth, and diagenesis in desert varnish. Geology 36, 215-218.

Hay, D.C., T.J. Dempster, M.R. Lee and D.J. Brown. 2010. Anatomy of a low temperature zircon outgrowth. Contributions to Mineralogy and Petrology 159, 81-92.

Holzer, L., R. Wepf, B. Münch and P. Marschall. 2010. Multiscale imaging of the pore structure of Opalinus Clay. Clays in Natural & Engineered Barriers for Radioactive Waste Confinement. 4th International Meeting, March 2010, Nantes, France.

Houben, M.E., B. Laurich, G. Desbois and J.L. Urai. 2012. Microstructure and porosity of Opalinus Clay at the Mont Terri rock laboratory (Switzerland). EGU General Assembly 2012. Geophysical Research Abstracts 14, 1 p.

Knudsen, K.D., J.O. Fossum, G. Helgesen and M.W. Haakestad. 2004. Small-angle neutron scattering from a nano-layered synthetic silicate. Physica B 352, 247-258.

Lee, M.R., D.J. Brown, C.L. Smith, M.E. Hodson, M. MacKenzie and R. Hellmann. 2007. Characterization of mineral surfaces using FIB and TEM: A case study of naturally weathered alkali feldspars. American Mineralogist 92, 1383-1394.

Lee, M.R. 2010. Transmission electron microscopy (TEM) of Earth and planetary materials: A review. Mineralogical Magazine 74, 1-27.

Mayer, J., L.A. Giannuzzi, T. Kamino and J. Michael. 2007. TEM Sample Preparation and FIB-Induced Damage. MRS Bulletin 32, 400-407.

Muller, J. and McCauley, J.L. 1992. Implication of fractal geometry for fluid flow properties of sedimentary rocks. Transport in Porous Media: 8, 133-147.

Patterson, R.J., D. Mayer, L. Weaver and M.W. Phaneuf. 2002. ‘‘H-bar lift-out’’ and ‘‘Plan-view lift-out’’: robust, re-thinnable FIB-TEM preparation for ex-situ cross-sectional and plan-view FIB specimen preparation. Microscopy and Microanalysis 8 (Suppl. 2), 566-567.

Petrunic, B.M., T.A. Al and L. Weaver. 2006. A transmission electron microscopy analysis of secondary minerals formed in tungsten-mine tailings with an emphasis on arsenopyrite oxidation. Applied Geochemistry 21, 1259-1273.

Promentilla, M.A.B., T. Sugiyama, T. Hitomi and N. Takeda. 2009. Quantification of tortuosity in hardened cement pastes using synchrotron-based X-ray computed microtomography. Cement and Concrete Research 39, 548-557.

Weyland, M., T.J.V. Yates, R.E. Dunin-Borkowski, L. Laffonta and P.A. Midgley. 2006. Nanoscale analysis of three-dimensional structures by electron tomography. Scripta Materialia 55, 29-33.

Ziese, U., K.P. de Jong and A.J. Koster. 2004. Electron tomography: a tool for 3D structural probing of heterogeneous catalysts at the nanometer scale. Applied Catalysis A: General 260, 71-74.